THE UNIVERSITY OF CHICAGO

SEASONAL EFFECTS ON BIOLOGICAL RHYTHMS

A DISSERTATION SUBMITTED TO

THE FACULTY OF THE DIVISION OF THE PHYSICAL SCIENCES

AND

THE FACULTY OF THE DIVISION OF THE BIOLOGICAL SCIENCES

AND THE PRITZKER SCHOOL OF MEDICINE

IN CANDIDACY FOR THE DEGREE OF

DOCTOR OF PHILOSOPHY

GRADUATE PROGRAM IN BIOPHYSICAL SCIENCES

BY

YEVGENIY LEYPUNSKIY

CHICAGO, ILLINOIS

AUGUST 2018

Table of Contents

List of Figures

List of Tables

Acknowledgements

During the course of my PhD, I discovered that science is a team sport. I could not have done my work without the help of many individuals and the support of my advisers, program administrators, family and friends, some of whom I would like to acknowledge here.

First, I would like to thank my advisers, Michael Rust and Aaron Dinner, for supervising my research, providing ideas for projects that suited my skillset, and pivoting when projects failed. They pushed me when I needed the pushing and allowed me struggle when I needed to work things out, helping me grow into a more independent thinker, experimentalist and communicator. I am greatly indebted to them scientifically, but I also owe them much for their concerns for each student's personal well-being. In particular, I appreciate the opportunity to work for the UChicago Innovation Fund in the middle of my PhD, which was a really significant professional experience for me. And I am truly thankful for the flexibility to work from abroad during the last six months of my PhD in order to spend time with my partner. There is much I learned from both of my advisers outside of specific research questions we were addressing. I am grateful for those discussions. Finally, I am glad that the gamble my advisers undertook in jointly mentoring a student from the Biophysical Sciences Program has grown into a wider-ranging collaboration between their research groups.

Additionally, I would like to acknowledge the support of many administrators, both in the Biophysical Sciences Program and at the Institute for Genomics and Systems Biology, who have made my graduate education possible. In particular, thanks to Michele Wittels, Julie Feder, Liza Herendeen and Temi Okubadejo for keeping things running smoothly! Special thanks to Tobin Sosnick for conceiving of and then administering the Biophysical Sciences Program, and also for

giving me the opportunity to take his course and then work as a teaching assistant for it. Finally, I'd like to thank Colleen Mullarkey in the Dissertation Office at UChicago for her patient help with formatting of the thesis.

I would also like to thank the many junior graduate and undergraduate students with whom I had a chance to work during their rotations, summer projects or while they were starting out in the Rust or Dinner Groups. I grew as a scientist and a mentor from these experiences. In particular, I owe thanks to UnJin Lee for his help in the early stages of the work described in Chapter 2. I am indebted to Haneul Yoo for her help in developing the 384-well assay to monitor KaiB-KaiC binding interactions using a polarization probe, which was essential in completing the work in Chapter 2. I would like to give a shout out to Danylo Lavrentovich who took on an ambitious project for his undergraduate thesis in the Dinner group; I am glad I was there to help and work alongside such a talented student.

I would like to acknowledge several Rust Lab members, who have helped me tremendously over the years. Connie Phong and Jenny Lin taught me many biochemical techniques over the years, and Jenny was an important collaborator in Chapter 2. Justin Chew was an incredibly positive and dependable team mate from day one, and I will always chuckle thinking about our long hours in the machine shop. Gopal Pattanayak has been a great friend and mentor in the Rust Lab and in life for many years. My thanks to him extend much beyond this page!

I would like to thank the Dinner Lab as a whole for many useful discussions and much advice over the years. Special thanks to my graduate program classmates Monika Scholz, Alan Hutchison, Herman Gudjonson, Ryan Mork and Kevin Song. Herman in particular has

contributed much towards my PhD; our discussions (and his help with math!) have influenced the direction of my work at many junctures. Kevin has also been a dear friend and great classmate in machine learning—thank you!

I want to express my gratitude to my family for their incessant support, even when they disagreed with my decisions. Their encouragement (when things looked grim) and honest joy (when things were looking up) formed the bedrock that helped me gain sure footing during my PhD.

And finally, I want to thank my partner Jagoda Rokicka for her love, patience and understanding, and her incredible ability to make me see things in a different light. She has helped me acquire a sense of direction, confidence and serenity that I needed to gain perspective and complete my PhD. I am one lucky guy.

Chapter 1 INTRODUCTION

Circadian rhythms: definitions and brief history of circadian biology

Circadian clocks are genetically encoded biological oscillators with approximately 24-hr period. Organisms in all kingdoms of life have evolved such endogenous timekeeping systems as internal representations of environmental cycles arising from Earth's daily rotation around its axis. These clocks provide innate pressures for many familiar daily activity patterns, such as the urge to be awake during the day and sleep at night.

The first published observation that circadian rhythms are self-sustaining, i.e., that they will persist in the absence of external signals, dates back to 1729 [1,2]. The discovery is due to an astronomer, the Frenchman Jean-Jacques d'Ortous De Mairan, who was interested in the rotation of the Earth around its axis. De Mairan reported that daily leaf-opening rhythms of plants (likely *Mimosa pudica*) persist, with a period of approximately 24 hours, even when the plants are maintained in constant darkness and temperature (Figure 1.1) [2].

For a long time, the scientific community was skeptical that rhythms observed in these experiments were truly self-sustaining, but these observations were confirmed and extended about a century later. Some of the first reports of endogenous circadian rhythms in insects and higher mammals date to late 1800s and early 1900s [1]. By the 1950s, the study of biological rhythms had gained momentum: the topic of the 1960 Cold Springs Harbor Symposium was "Biological Clocks." In 1959, Franz Halberg coined the term circadian to describe processes that occur with approximately daily frequency from the Latin words "circa" (approximately) and "dies" (day) [1].

Around the same time, the scientific community reached a consensus regarding three properties defining circadian rhythms (Figure 1.2). For a behavior to be recognized as circadian, (i) it must occur with approximately 24-hr period in the absence of rhythmic cues from the environment, (ii) this circadian period must vary little over the range of physiological temperatures, and (iii) the phase of the rhythm must be sensitive to environmental signals to which the rhythm entrains (e.g., light and temperature) [3].

The advent of genetics enabled scientists to begin studying the mechanisms of circadian rhythms. Mutations affecting period length were discovered in fruit flies, green algae and fungi in the 1970s, and the first clock gene (*Drosophila period* gene, *per*) was cloned in 1984 by Hall, Rosbash and Young [1,4]. In 2017, these researchers were awarded the Nobel Prize in Physiology or Medicine for this important step and further elucidation of molecular mechanisms governing circadian clocks [4].

Figure 1.1. Illustration of De Mairan's experiments showing that daily leaf-opening rhythms in mimosa plants persist even when plants are placed in constant conditions. Figure modified from [4].

Much effort in the genetic era has focused on deciphering the molecular mechanisms of circadian rhythms, often asking what genes are necessary to generate free-running rhythms in constant conditions and how they interact with each other. Though molecular players differ

between species, the common paradigm that emerged is that in each organism there is a core set of proteins (the "core" or "master" clock), which conspire together to promote an ordered cycle of transcriptional and post-transcriptional events, leading to ≈24-hr rhythms in each other's gene expression and/or protein phosphorylation [5]. This cycle sets the internal time, which is then transmitted to give rise to genome-wide oscillations in transcription as well as physiological rhythms [6]. Findings that clocks control the transcription of a large fraction of genes in fruit flies and cyanobacteria underscore the important role clocks play in global gene regulation [7,8].

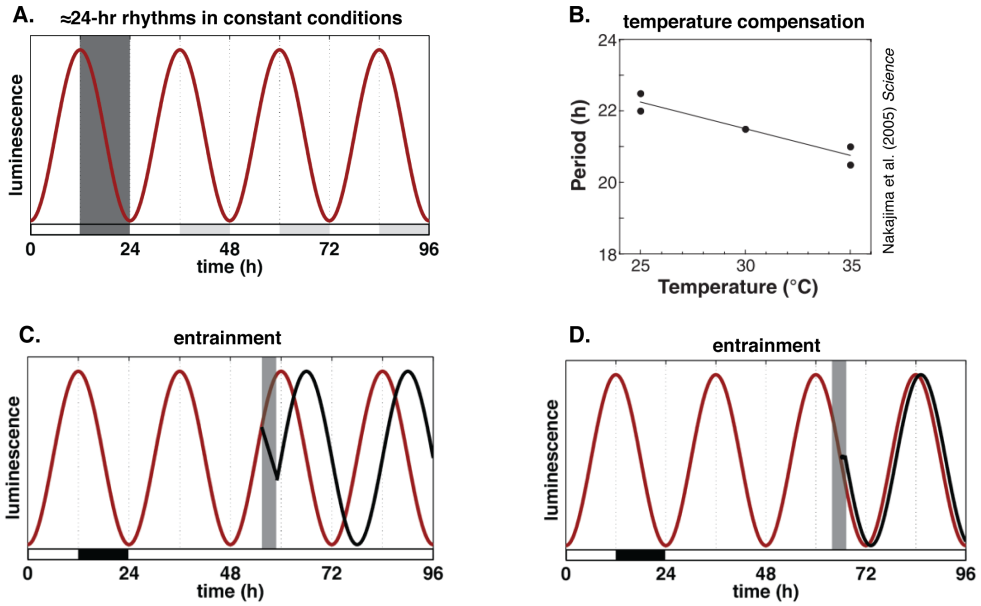

Figure 1.2. Three defining features of circadian rhythms.
(A) Circadian rhythms are free-running: they persist with ≈24-hr period in the absence of external stimuli. Schematic of a typical measurement for the cyanobacterial clock system (see Chapter 2 and Appendix A), where luminescent reporters of gene expression are commonly used to monitor circadian rhythms. Cells typically receive a 12-hr pulse of light, followed by a 12-hr pulse of darkness (grey bar) before being released into continuous light (at 24 hr in this panel).
(B) Circadian rhythms are temperature-compensated: the period remains circa 24 hours as the temperature is varied over a physiological range. Panel adapted from [9].
(C-D) Circadian rhythms are can be entrained by external signals: the phase of the rhythm can be modulated in response to an environmental signal (for cyanobacteria, this can be a dark pulse), even as the period remains unchanged. These schematics illustrate that the magnitude of the phase shift depends on the phase when the environmental signal is applied.

Though it is important to understand the mechanisms by which the circadian clocks generate free-running oscillations in constant conditions, it is noteworthy that in natural conditions the clock is almost never free-running. Because clock phase is sensitive to environmental inputs, in natural environments circadian clocks are driven by external changes in light, temperature, availability of food and other factors. These external entraining cues also change between different environments and with the seasons. In my thesis, I focused on this seasonal aspect.

Questions motivating my thesis

Many articles in the field of circadian rhythms begin with a seemingly obligatory remark about the purpose of circadian clocks. Typically, the intent is to communicate to the reader that circadian clocks help organisms to appropriately align physiology and behavior with the day-night cycle [10–13]. These statements are usually made in a matter-of-fact way, as if to underscore their self-evidence. However, to a large extent, these statements are conjectures, pointing to deep unanswered questions about the role of circadian clocks.

What does it mean for the clock to "appropriately" align to the day-night cycle? I think most researchers would say that the answer depends on the specific environmental conditions. Much of what's known about circadian control of physiological rhythms comes from laboratory studies in idealized conditions, such as a 12-hr light / 12-hr dark cycle (LD12:12), constant light or constant darkness. In this sense, it is known what biological clocks "do" in these settings, and several studies have demonstrated that clock mutants are disadvantaged in light-dark cycles in the lab [14,15]. Yet these conditions are very different from the demands of natural

environments, where light levels and temperature vary not only throughout the day, but also seasonally and between geographies.

Activity rhythms in natural environments can be quite different from what's observed in the lab [16,17]. It is poorly understood how circadian clocks function in these natural settings, what is the optimal coordination of physiological rhythms with the day-night cycle in these conditions, and whether circadian clocks are effective at optimally aligning physiology in this way [13]. Addressing questions at the intersection of circadian biology and ecology is difficult because doing so requires monitoring rhythmic behavior in a wide range of conditions or developing technology to mimic such conditions in the lab.

I am in interested in such questions related to circadian function in ecologically relevant environments [18]. In my thesis work, I have focused on seasonal effects on circadian rhythms (admittedly, it's a stretch to call this "ecology") from two perspectives. In Chapter 2, I describe my study of how the circadian clock of cyanobacteria responds to seasonal changes day length. The cyanobacterial clock system allowed me to measure the response of the cellular rhythm to the light-dark cycle and to trace the biochemical origin of this response. Along the way, I developed methods to culture cyanobacteria in diverse light-dark environments in a multiplexed fashion. Later, in a very different approach described in Chapter 3, I studied seasonal changes in daily activity patterns of humans by monitoring their social media activity over the course of two years. In Appendix A, I describe my efforts to connect clock function to fitness in cyanobacteria as a follow-up to work in Chapter 2.

REFERENCES

1. McClung, C.R. (2006). Plant Circadian Rhythms. The Plant Cell 18, 792–803.

2. Bünning, E. (1960). Opening Address: Biological Clocks. Cold Spring Harb Symp Quant Biol 25, 1–9.

3. Golden, S.S., and Canales, S.R. (2003). Cyanobacterial circadian clocks — timing is everything. Nature Reviews Microbiology 1, 191–199.

4. The 2017 Nobel Prize in Physiology or Medicine - Press Release Available at: https://www.nobelprize.org/nobel_prizes/medicine/laureates/2017/press.html [Accessed May 25, 2018].

5. Hamilton, E.E., and Kay, S.A. (2008). SnapShot: Circadian Clock Proteins. Cell 135, 368-368.e1.

6. Panda, S., Hogenesch, J.B., and Kay, S.A. (2002). Circadian rhythms from flies to human. Nature 417, 329–335.

7. Ito, H., Mutsuda, M., Murayama, Y., Tomita, J., Hosokawa, N., Terauchi, K., Sugita, C., Sugita, M., Kondo, T., and Iwasaki, H. (2009). Cyanobacterial daily life with Kai-based circadian and diurnal genome-wide transcriptional control in Synechococcus elongatus. Proceedings of the National Academy of Sciences of the United States of America 106, 14168–73.

8. Dinner, A., Hutchison, A., and Allada, R. Unpublished Data.

9. Nakajima, M., Imai, K., Ito, H., Nishiwaki, T., Murayama, Y., Iwasaki, H., Oyama, T., and Kondo, T. (2005). Reconstitution of Circadian Oscillation of Cyanobacterial KaiC Phosphorylation in Vitro. Science 308, 414–415.

10. Miller, B.H., McDearmon, E.L., Panda, S., Hayes, K.R., Zhang, J., Andrews, J.L., Antoch, M.P., Walker, J.R., Esser, K.A., Hogenesch, J.B., et al. (2007). Circadian and CLOCK-controlled regulation of the mouse transcriptome and cell proliferation. Proceedings of the National Academy of Sciences 104, 3342–3347.

11. Liu, Z., Huang, M., Wu, X., Shi, G., Xing, L., Dong, Z., Qu, Z., Yan, J., Yang, L., Panda, S., et al. (2014). PER1 Phosphorylation Specifies Feeding Rhythm in Mice. Cell Reports 7, 1509–1520.

12. Partch, C.L., Green, C.B., and Takahashi, J.S. (2014). Molecular architecture of the mammalian circadian clock. Trends in Cell Biology 24, 90–99.

13. Roenneberg, T., and Merrow, M. (2016). The Circadian Clock and Human Health. Current Biology 26, R432–R443.

14. Ouyang, Y., Andersson, C.R., Kondo, T., Golden, S.S., and Johnson, C.H. (1998). Resonating circadian clocks enhance fitness in cyanobacteria. Proceedings of the National Academy of Sciences 95, 8660–8664.

15. Dodd, A.N. (2005). Plant Circadian Clocks Increase Photosynthesis, Growth, Survival, and Competitive Advantage. Science 309, 630–633.

16. Vanin, S., Bhutani, S., Montelli, S., Menegazzi, P., Green, E.W., Pegoraro, M., Sandrelli, F., Costa, R., and Kyriacou, C.P. (2012). Unexpected features of Drosophila circadian behavioural rhythms under natural conditions. Nature 484, 371–375.

17. Daan, S., Spoelstra, K., Albrecht, U., Schmutz, I., Daan, M., Daan, B., Rienks, F., Poletaeva, I., Dell'Omo, G., Vyssotski, A., et al. (2011). Lab Mice in the Field: Unorthodox Daily Activity and Effects of a Dysfunctional Circadian Clock Allele. Journal of Biological Rhythms 26, 118–129.

18. Millar, A.J. (2016). The Intracellular Dynamics of Circadian Clocks Reach for the Light of Ecology and Evolution. Annual Review of Plant Biology 67, 595–618.

Chapter 2 THE CYANOBACTERIAL CIRCADIAN CLOCK FOLLOWS MIDDAY *IN VIVO* AND *IN VITRO*

This chapter was published as an article in *eLife 2017;6:e23539* and appears below with minor formatting modifications.

Authors: Eugene Leypunskiy, Jenny Lin, Haneul Yoo, UnJin Lee, Aaron R. Dinner, Michael J. Rust. All authors are from the University of Chicago.

ABSTRACT

Circadian rhythms are biological oscillations that schedule daily changes in physiology. Outside the laboratory, circadian clocks do not generally free-run, but are driven by daily cues whose timing varies with the seasons. The principles that determine how circadian clocks align to these external cycles are not well understood. Here we report experimental platforms for driving the cyanobacterial circadian clock both *in vivo* and *in vitro*. We find that the phase of the circadian rhythm follows a simple scaling law in light-dark cycles, tracking midday across conditions with variable day length. The core biochemical oscillator comprised of the Kai proteins behaves similarly when driven by metabolic pulses *in vitro*, indicating that such dynamics are intrinsic to these proteins. We develop a general mathematical framework based on instantaneous transformation of the clock cycle by external cues, and it successfully predicts clock behavior under many cycling environments.

INTRODUCTION

Circadian clocks generate biological rhythms that temporally organize physiology to match the 24-hour diurnal cycle. Though these clocks continue to oscillate in constant laboratory conditions, in natural environments they are driven by the external cycle of day and night. Because of latitude-dependent changes in the duration of day and night throughout the year, clock architectures must incorporate mechanisms that respond appropriately to environmental signals, such as dawn and dusk, whose schedule changes throughout the year. Data from several species indicate that circadian clocks adapt to different day lengths by modulating their phases relative to the light-dark cycle [1,2]. In this way, circadian oscillators are able to coordinate physiological events relative to specific times of day and, in multicellular organisms, specialized mechanisms exist that allow oscillators in different cells to follow distinct times of day [3,4]. Because the biochemical circuits governing circadian rhythms and light-dark sensing in such organisms are complex, it has been difficult to identify which features of circadian systems are responsible for seasonal adaptation. More generally, it remains unclear what features oscillators must have to respond appropriately to varying light-dark cycles and how those features are implemented molecularly in specific systems.

Cyanobacteria present a unique opportunity to elucidate molecular mechanisms in circadian biology because the core oscillator responsible for driving genome-wide transcriptional rhythms can be reconstituted using purified KaiABC proteins, and these proteins have been extensively studied biochemically in constant conditions [5,6]. However, cyanobacteria must contend with large seasonal variations in day length because their natural aquatic environments span a wide range of latitudes [7]. Yet, comparatively little is known about how the

cyanobacterial clock functions when driven by light-dark cycles that mimic days in different seasons.

To study how the circadian clock is affected by light-dark cycles with different day lengths, we developed multiplexed LED illumination devices to grow cyanobacteria in a wide range of light-dark conditions (Figure 2.1A). We used square-wave illumination patterns in our experiments, and used the times of lights-on and lights-off as experimental analogs of dawn and dusk, respectively. We defined the day length (τ) as the total time the lights are on each day (Figure 2.1A). We found that the circadian rhythm in the cyanobacterium *Synechococcus elongatus* PCC 7942 (*S. elongatus*) follows a simple rule: the phase of clock-driven gene expression scales linearly with day length and remains fixed relative to the middle of the day over a wide range of day lengths.

We biochemically simulated seasonal effects in the reconstituted KaiABC oscillator by driving the Kai proteins with pulses of nucleotides on a 24-hour cycle, simulating *in vivo* metabolic conditions during day and night. Remarkably, this *in vitro* system shows a similar linear scaling of clock phase with simulated day length, indicating that core mechanisms for seasonal adaptation are intrinsic to the Kai proteins. We developed a minimal mathematical model for oscillator entrainment based on rapid transitions between distinct day and night clock cycles. The model can account for the ability to track midday if the phase shifts caused by dawn and dusk depend linearly on clock time with appropriate slopes. By calibrating this model with independent measurements *in vitro* and *in vivo*, we were able to predict the results of phase response experiments, and the behavior of the clock in non-24 hour light-dark cycles.

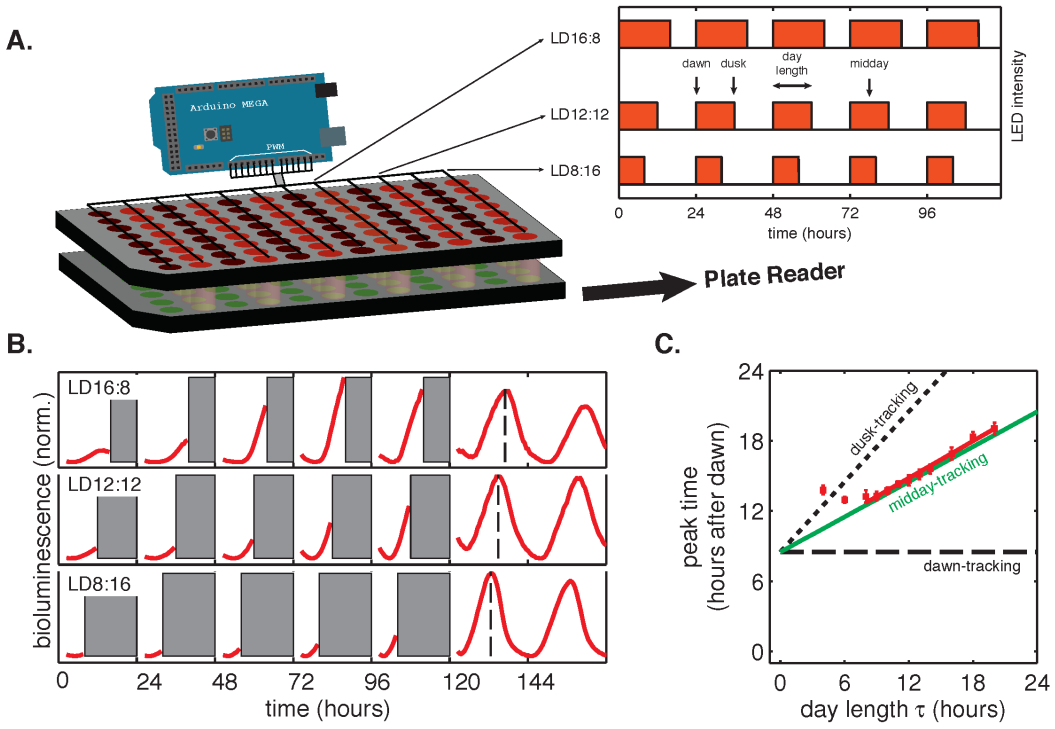

Figure 2.1. Phase of the cyanobacterial circadian rhythm scales linearly with day length. (A) LED array device used to grow *S. elongatus* in programmable light-dark cycles. Cells grown in a 96-well plate on solid media (lower plate, *green circles*) are illuminated from above by LEDs (*red circles*). An Arduino microcontroller is used to dynamically change LED intensity in different columns of the plate (*inset*). Luminescence from the bottom plate is read out every 30 minutes on a plate reader. Drawing not to scale.
(B) Drive-and-release strategy to measure phase of the circadian clock under light-dark (LD) cycling. Cells were exposed to five entraining LD cycles and then released into constant light. Bioluminescence signals (P_{kaiBC}::*luxAB*) from each well were separated into individual "day" and "night" windows. Data from night portions of the experiment were omitted from analysis (*gray bars*) and data from the day portions of the experiment were aligned to zero baseline and normalized to unit variance. Dashed lines indicate time of peak reporter signal calculated by parabolic fitting. See Computational Methods for details.
(C) Peak time of bioluminescence (P_{kaiBC}::*luxAB*) in light-dark cycles of different day length *(red squares)* was quantified by local parabolic fitting around the first maximum of the oscillation after release into constant light. Error bars represent standard deviations of peak time estimates from technical replicates (n=4-8). Slope of the linear fit (*red line*, m=0.53±0.01) was determined by linear regression. *Dashed and dotted black lines* indicate scaling of phase with day length for dawn- and dusk-tracking oscillators; *green line* indicates midday-tracking behavior.

The essential feature of the model, the linear dependences of phase shifts on clock time, has a simple geometric interpretation in terms of the deformation of the clock orbit caused by a

transition between light and dark. Thus, the entrained behavior of the circadian clock can be captured quantitatively by a mathematical framework with a small number of parameters. This framework in turn can be used to guide the design of experiments that probe the molecular origins of key mathematical features. The precisely defined nature of the cyanobacterial clock facilitates such experiments, but the model is general, so we expect it to be useful for other organisms as well.

RESULTS

Cyanobacteria respond to seasonal changes in day length by aligning the phase of circadian gene expression relative to midday.

S. elongatus is a photosynthetic bacterium whose physiology is closely tied to light and dark. In constant light, the circadian clock exerts pervasive control over gene expression: most transcripts cycle in abundance with ≈24-hour period, with the majority of transcripts peaking either near subjective morning (dawn genes), or nearly 12 hours later, at subjective nightfall (dusk genes) [8,9]. In the dark, however, growth stops, and most gene expression is highly repressed [10–12]. Thus, portions of the circadian gene expression program that fall into nighttime hours are strongly attenuated.

Viewed in this way, the hours between dawn and dusk provide a limited window for gene expression, so that winter months at high latitude provide fewer daylight hours for this cyanobacterium to accomplish biosynthetic tasks relative to summer months. We surmised that an important function for the circadian clock in this organism might be to schedule gene expression appropriately during daylight hours, when biosynthetic resources are available. We

thus expected that asymmetric light-dark cycles mimicking days in different seasons would realign the clock cycle.

To systematically study how circadian gene expression in *S. elongatus* adjusts to asymmetric light-dark schedules, we built a microcontroller-driven LED array device and used it to grow cells in 24-hour day-night cycles with photoperiod (day length) varying from 4 to 20 hours (Figure 2.1A). This LED array was coupled to a plate reader that allowed us to monitor clock output—gene expression from clock-driven promoters—using strains engineered with luminescent reporters for representative dusk (*kaiBC*) and dawn (*purF*) genes.

In these experiments, the circadian clock stably entrained to light-dark cycles with a wide range of day lengths (τ = 8-16 hours) within roughly three days (Figure S2.1, Figure S2.2). We found that the phase of the oscillation, that is, when the peak clock output signal occurred relative to dawn, varied systematically as a function of day length. In general, longer days resulted in the peak reporter signal occurring later in the day (Figure 2.1B). By plotting the time of peak reporter signal versus day length, we found that the driven behavior of the clock follows a simple scaling law: the clock phase is proportional to day length (Figure 2.1C). The proportionality constant, m, falls in an intermediate range (Figure 2.2) between the limits corresponding to either dawn (m=0) or dusk (m=1) fully resetting the clock. The linear relationship between clock phase and day length with slope $m \approx 0.5$ implies that cyanobacteria set their clock to reach the same internal time at the middle of the daylight hours, independent of day length. This entrainment behavior is not unique to the *kaiBC* promoter; a reporter for *purF*, a representative of the dawn class of genes, shows similar scaling behavior with day length (Figure S2.3).

The fact that the core oscillator of the cyanobacterial circadian clock can be reconstituted *in vitro* from purified Kai proteins [13,14] naturally led to the question of whether the ability to track midday that we observed *in vivo* is intrinsic to the core oscillator, or if it requires additional factors present in the cell. We thus sought to extend the reconstituted system such that we could drive the biochemical oscillator with rhythmic input signals.

figure	driving period T (hours)	day length τ (hours)	slope m ± SD of estimate
Figure 2.1C	24	4, 6, 8, 9, 10, 11, 12, 13, 14, 16, 18, 20	0.55 ± 0.02 (sinusoidal fitting), 0.53 ± 0.01 (parabolic fitting)
Figure S2.2	24	8, 12, 16	0.47 ± 0.03 (sinusoidal fitting), 0.57 ± 0.02 (parabolic fitting)
Figure 2.5C	22, 23, 24, 25, 26	8, 10, 12, 14	0.51 ± 0.11

Table 2.1. Summary of biologically independent *in vivo* experiments measuring entrainment to 24-hour light-dark cycles of varying day length.
Summary of biologically independent *in vivo* experiments measuring entrainment to 24-hour light-dark cycles of varying day length and corresponding estimates of *m*, the proportionality coefficient between the peak time of P_{kaiBC}*::luxAB* reporter and day length during light-dark entrainment.

***In vitro* reconstitution of seasonal clock response.**

A purified mixture of the KaiA, KaiB, and KaiC proteins spontaneously generates a stable circadian rhythm in KaiC phosphorylation and in the formation of KaiB-KaiC complexes [13,14]. Though the Kai proteins are not light-sensitive, recent work has shown that they are sensitive to metabolite pools that shift in response to changes in photosynthetic activity in the cell: KaiA is sensitive to the redox state of quinones, and KaiC phosphorylation is sensitive to the ATP/ADP ratio [15–17]. We thus developed a protocol to mimic repeated light-dark cycles *in vitro* by cycling the ATP/ADP ratio between physiologically relevant levels experienced

during day and night, using ADP addition to simulate nightfall ($[ATP]/([ATP]+[ADP]) \approx 25\%$) followed by buffer exchange into an ATP-only buffer to simulate dawn ($[ATP]/([ATP]+[ADP]) \approx 100\%$) (Figure 2.2A).

We found that the KaiC phosphorylation rhythm readily responded to this metabolite pulsing protocol. Stepping into the lower ATP/ADP conditions promoted dephosphorylation, in accord with previously published observations [18]. Conversely, stepping into higher ATP/ADP conditions favored phosphorylation (Figure 2.2B). Pulsing the ATP/ADP ratio in this way caused the KaiC phosphorylation rhythm to synchronize to the external cycle. By the third cycle, the oscillator appeared to have stably entrained, and, similar to the clock behavior we observed in live cells, longer times in daytime buffer led to later peak phosphorylation times. We estimated peak times for these oscillator reactions during the third entraining cycle and found that the phase of the *in vitro* rhythm scales linearly in proportion with simulated day length (Figure 2.2C), with KaiC phosphorylation rhythm peaking roughly 3 hours after the midpoint of simulated daytime, suggesting that the reconstituted Kai oscillator is capable of tracking the approximate midday point of an externally imposed metabolic rhythm.

To more accurately measure the scaling of entrained phase with day length in KaiABC oscillator reactions, we turned to a fluorescence polarization probe that enables automated measurement of oscillator state with high temporal resolution (Figure S2.4) [19,20]. We used this assay to determine clock phases in free-running conditions after entraining the Kai proteins with three metabolic cycles, analogous to the design of the *in vivo* experiments. We again measured linear scaling of the entrained phase, albeit with a lower slope than the estimate from sparser gel-based measurements of KaiC phosphorylation (m=0.38±0.07 for polarization probe vs.

m=0.51±0.04 for phosphorylation data, Figure 2.2C). Despite the variability in our estimates of *m*, these measurements argue that the *in vitro* oscillator successfully captures the essential feature of seasonal entrainment we observed *in vivo*: linear scaling of entrained phase with an intermediate slope.

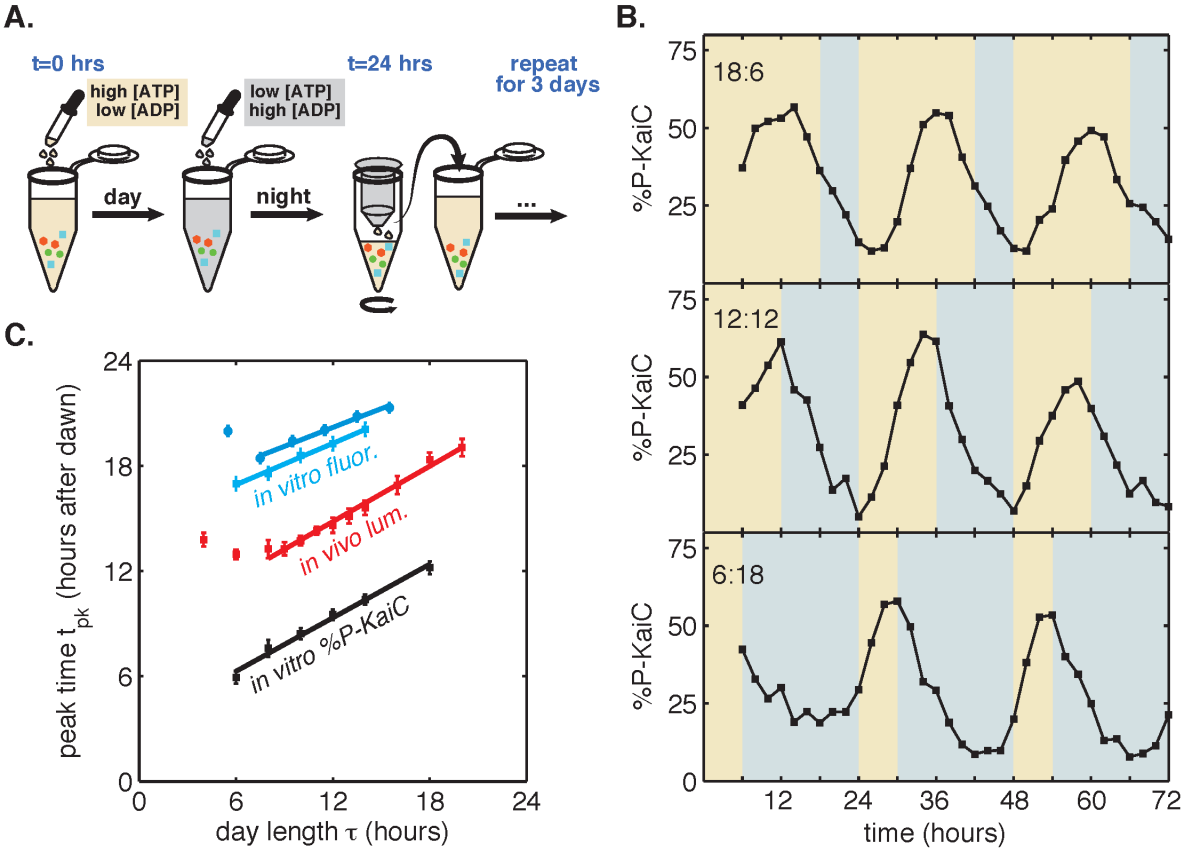

Figure 2.2.Reconstitution of the seasonal clock response *in vitro*.
(A) Buffer exchange protocol to simulate metabolic driving of the clock. To mimic daytime *in vitro*, purified Kai proteins (*green, blue and red symbols*) were incubated in "day" reaction buffer containing 2 mM (%P-KaiC) or 2.5 mM (fluorescence polarization) ATP. ADP was added (7.5 mM ADP final) to mimic nightfall. At simulated dawn, reactions were returned to "day" buffer via buffer exchange.
(B) Example traces of KaiC phosphorylation rhythm from *in vitro* reactions mimicking LD 18:6 (*top*), LD 12:12 (*middle*), and LD 6:18 (*bottom*).
(C) Phase of KaiABC oscillation scales linearly with simulated day length (time spent in "day" buffer), as assessed by the peak time of KaiC phosphorylation (*black squares*) or peak time of fluorescence polarization (*cyan squares* and *circles*, for two replicates) of fluorescently labeled KaiB. Peak times of fluorescence polarization were estimated from sinusoidal fits to oscillations

(Figure 2.2 continued) recorded in free-running conditions after entraining the oscillator with three metabolic cycles. Peak time of %P-KaiC was estimated by fitting KaiC phosphorylation time series from the third day of reactions to sinusoids. Error bars represent uncertainty of fit phase from sinusoidal regression. Lines of best fit determined by linear regression (*cyan squares:* m=0.39±0.06, *cyan circles:* m=0.36 ± 0.04, *black:* m=0.51±0.04). *In vivo* data (from Figure 2.1C) is plotted in *red*. Scaling of entrained phase was measured once via KaiC phosphorylation analysis (*black*) and twice using the fluorescence polarization probe (*cyan squares* and *circles*) with an independent preparation of proteins.

In the cell, the Kai proteins interact with histidine kinases and a network of other factors absent from the reconstituted system, ultimately leading to rhythms in transcription across the genome, including the *kai* genes themselves [21–23]. These additional factors may account for the differences we observe between proportionality constants *in vitro* and *in vivo*, and the time delay between KaiC phosphorylation and luminescent output of the *kaiBC* expression reporter is likely responsible for the offset in Figure 2.2C. While these considerations suggest that care must be taken in connecting the *in vitro* and *in vivo* results, they also underscore the significance of our observation that the Kai oscillator proteins by themselves are sufficient to yield the linear response of the system to altered day length. We therefore sought to use this *in vitro* model of seasonality to uncover the biochemical basis of the linear seasonal clock response.

Seasonal adaptation of the circadian oscillator can be decomposed into step responses to individual metabolic cues.

In the purified system, the entraining cues are steps between high and low ATP/ADP that simulate dawn and dusk. We therefore sought to decompose the seasonal adaptation of the clock into step responses following each metabolic transition. This approach is related to the limit cycle theory of oscillators: if we assume that a unique stable orbit exists for both the day and

night conditions, then a metabolic transition forces the system to adjust from its current cycle to one associated with the new condition. If relaxation to the new orbit occurs rapidly relative to the length of the day—that is, if the light and dark orbits are strongly attracting—then the state of the oscillator at each transition can be specified simply by a phase angle on that orbit. In this limit, the response of the system is fully determined by instantaneous phase shifts caused by the transitions. Mathematically, we describe this limit as an oscillator comprised of a single phase variable, θ, that runs along a fixed limit cycle trajectory at constant speed (see Mathematical Appendix). The responses to dark-to-light or light-to-dark transitions are then represented by phase shifts that are specified by the functions $L(\theta)$ and $D(\theta)$, respectively.

To determine whether this fast-relaxation approximation can describe phase shifts in the core Kai oscillator, and to study their biochemical basis, we measured the $L(\theta)$ and $D(\theta)$ shift functions in our reconstituted system. To measure the $D(\theta)$ function, we incubated the Kai proteins in daytime buffer, then transferred them into nighttime buffer at various times throughout the circadian cycle and studied how the oscillation was affected. As previously, we assayed oscillator response in separate experiments using either SDS-PAGE to measure KaiC phosphorylation or the fluorescence polarization probe to achieve high temporal resolution; example time series from the fluorescence polarization measurements are shown in Figure 2.3A-B.

We proceeded to calculate phase shifts from these measurements, taking into consideration that a switch to nighttime buffer conditions could affect the oscillator in two ways: the phase of the oscillation can shift, and the oscillator period may change, both of which can change the relative timing of peaks. In order to separate these effects, it is necessary to collect

enough data to accurately determine the period, and then extrapolate backwards to infer the instantaneous phase shift at the time of buffer exchange. We detail our procedure for analyzing these data to extract phase shifts in Figure S2.5. We used an analogous design to measure the reverse steps from nighttime to daytime buffer (Figure 2.3B). Plotted together in Figure 2.3C-D, the extrapolated phase shifts measure the sensitivity of the clock to individual light and dark steps throughout the 24-hour day.

The measured $L(\theta)$ and $D(\theta)$ step-response functions show that the phase of the purified KaiABC oscillator is responsive to both step-up and step-down metabolic changes. For example, a day-to-night shift lengthens the period of the clock by about 2 hours, and, when it is applied at subjective morning, leads to an instantaneous phase delay of about 3 hours (Figure S2.5). On the other hand, a night-to-day transition in the middle of subjective night shortens the period and causes a phase advance of about 1.5 hours.

These measurements characterize how the oscillator responds to a metabolic step-change throughout the entire clock cycle. However, when the clock is stably synchronized to a cycling environment, dawn and dusk fall only in a limited window of clock phases. To determine this window, we returned to our measurements in Figure 2.2C. We identified phases that correspond to dawn or dusk in entrained conditions mimicking LD 6:18 to LD 18:6 and marked these phases on the $L(\theta)$ and $D(\theta)$ functions (Figure 2.3C-D, colored arrows). These points fell on gradually changing, approximately linear, regions of both curves, spanning roughly 6-hour windows near subjective dawn (for $L(\theta)$) and subjective dusk (for $D(\theta)$). Because these regions of $L(\theta)$ and $D(\theta)$ represent phase shifts comparable in magnitude but opposite in sign, we hypothesized that their opposing forces could enable oscillator entrainment to light-dark cycles.

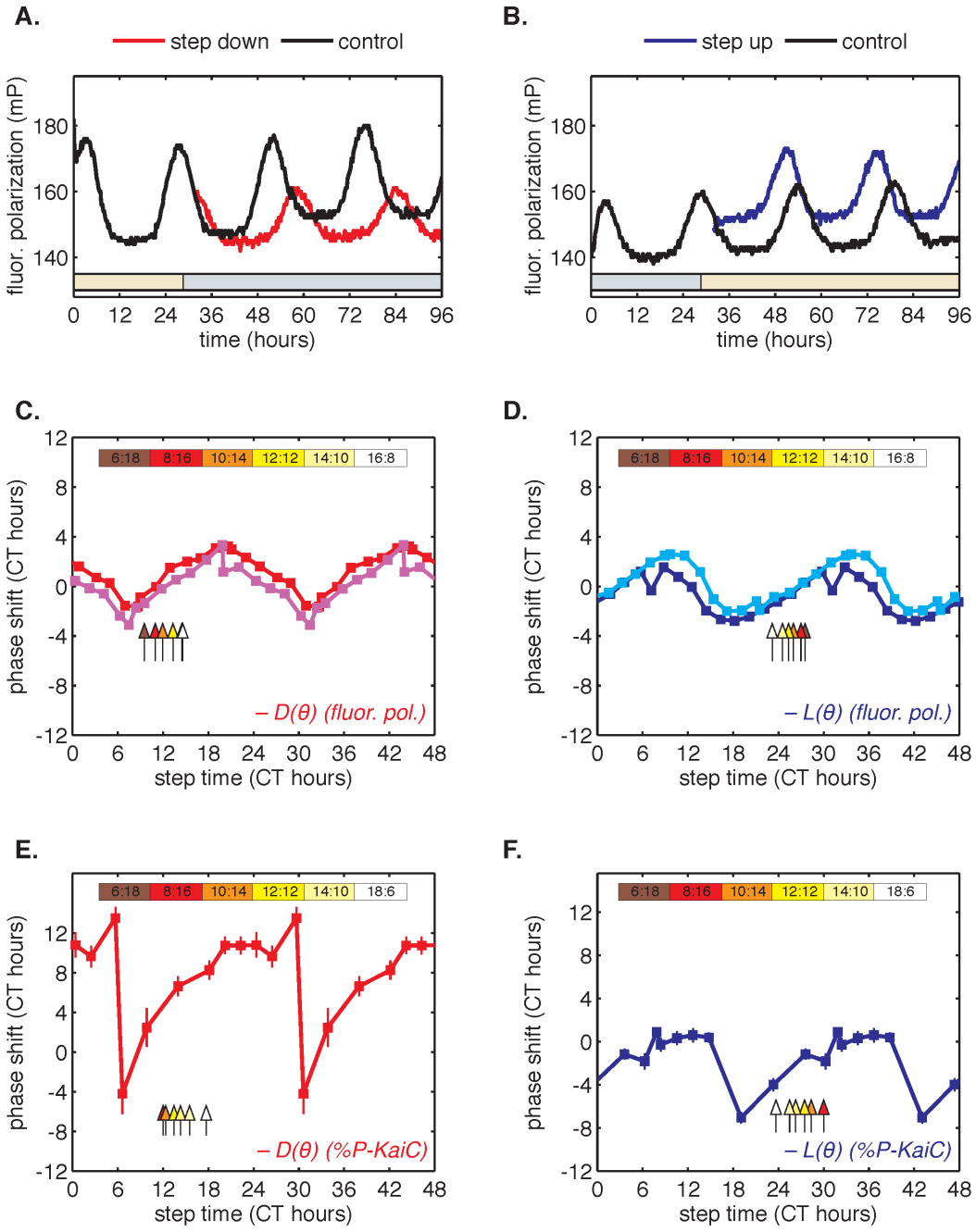

Figure 2.3. Clock responses to metabolic steps mimicking dawn (step up) and dusk (step down).

(A) Phase shift in fluorescence polarization (*red curve*) caused by a shift to a buffer that mimics the nucleotide pool at night (7.5 mM ADP, 2.5 mM ATP, *gray bar*). The control reaction remained in the original buffer (*black curve*).

(Figure 2.3, continued) (B) Phase shift in fluorescence polarization (*blue curve*) caused by a shift from night buffer back to day buffer (2.5 mM ATP, *beige bar*).
(C, D) Summary of phase shifts caused by metabolic step-down (C) or step-up (D) perturbations throughout the clock cycle. Simulated day-night or night-day steps were administered as in (A) and (B). Different colors represent independent measurements. To estimate the phase of each reaction, trajectories were fit to sinusoids. Phase shifts were determined relative to the respective control reactions. The times at which buffer steps were administered were converted to circadian time (CT 0 corresponds to the estimated trough of KaiC phosphorylation based on Figure S2.4). Colored arrows indicate clock phases when metabolic shifts occur in entrained conditions.
(E, F) Analogs of (C, D) for the gel-based phosphorylation measurements on an independent preparation of Kai proteins. Simulated day-night or night-day steps were administered by ADP addition to simulate nighttime (7.5 mM ADP, 2 mM ATP) or buffer exchange into a high-ATP buffer to simulate daytime (2 mM ATP). Data analysis was analogous to (C, D). Error bars represent standard deviations calculated by bootstrapping (see Computational Methods). Horizontal error bars are smaller than marker widths.

To check this hypothesis, we simulated a simple (phase-only) oscillator that runs at constant frequencies in the light and dark and adjusts its phase in response to dawn and dusk according to the phase shift functions that we measured in Figure 2.3C-D (see Computational Methods). This model essentially maps the one-dimensional phase variable from one cycle to the next according to $L(\theta)$ and $D(\theta)$. We analyzed the stability properties of this map and found that the oscillator could entrain with a unique phase to driving periods of within 4-5 hours of its natural circadian period. Outside this range, the oscillator failed to entrain or exhibited more complex dynamics (Figure S2.6).

We proceeded to test whether the measured $L(\theta)$ and $D(\theta)$ step-response functions could successfully reproduce the entrainment of the oscillator to repeated 24-hour metabolic cycles of varying day length, shown in Figure 2.2. When subjected to light-dark cycles in simulations, the oscillator model stably entrains to the diurnal schedule within two-to-five cycles (Figure 2.4A-B, Figure S2.7A). Importantly, the simulated entrained phase scales linearly with day length with a slope similar to the experimental data, indicating that the driven clock response can indeed be

decomposed into a series of step responses to environmental transitions (Figure 2.4C, Figure S2.7).

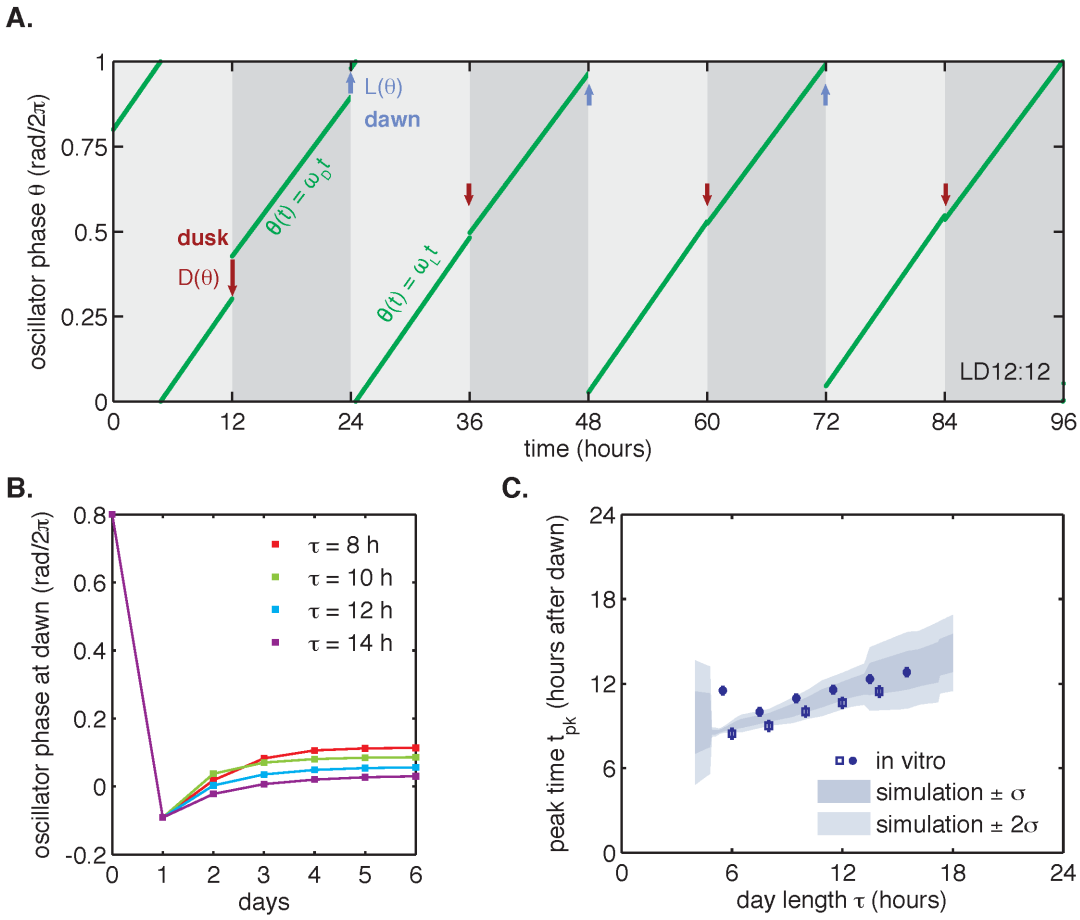

Figure 2.4. Entrainment of the phase oscillator model to a driving cycle.
(A) Schematic of a phase-only oscillator that responds to dawn and dusk with instantaneous phase shifts. The oscillator runs at constant velocities ω_L during the day and ω_D at night (*green lines*), except for dawn and dusk where sudden shifts occur (*red and blue arrows*). This simulation illustrates entrainment to a LD 12:12 diurnal cycle for an oscillator with ω_L (1/23.7 hours), ω_D (1/25.7 hours), and $L(\theta)$ and $D(\theta)$ as experimentally measured for the KaiABC oscillator (see main text, Computational Methods). Refer to Figure S2.7B for illustrations of $L(\theta)$ and $D(\theta)$ used in this simulation.
(B) Simulated approach to stable entrainment in the model (as in Figure 2.4A) for light-dark cycles of different day length (τ=8-14 hours).
(C) Simulated seasonal response of an oscillator that responds rapidly to light-dark cues according to the phase shift functions in Figure 2.3C (see text). In simulations, t_{pk} is defined as the time when oscillator phase θ equals 0.5 rad/2π, corresponding to the peak of KaiC phosphorylation. Shaded areas correspond to standard deviations of entrainment simulations

(Figure 2.4 continued) using the four possible combinations of *L* and *D* functions shown in Figure 2.3(C-D). *Blue squares and circles* indicate experimentally determined entrained phases measured using the fluorescence polarization reporter in Figure 2.2C. Peak times in polarization data were converted to equivalent peak KaiC phosphorylation times using the measured phase offset for the polarization reporter of 2π/3 rad (Figure S2.4. Validation of KaiB fluorescence polarization reporter against KaiC phosphorylation rhythm.). Error bars on *in vitro* data are based on uncertainty of fit phase of sinusoidal trajectories.

As mentioned above, we also measured $L(\theta)$ and $D(\theta)$ step-response functions with a separate preparation of Kai proteins using a gel-based assay to read out the phase of the KaiC phosphorylation rhythm (Figure 2.3E-F). Though the absolute magnitude of the step responses in these measurements was larger, they still predict linear scaling of entrained phase in simulations for day lengths between 6 and 14 hours (Figure S2.8B). The discrepancy in magnitude between these measurements may point to differences in sensitivity to input cues between different preparations of Kai proteins, or to a slight perturbative effect of fluorescently labeled KaiB.

We found that simulated entrainment of the phase oscillator model was particularly sensitive to the regions surrounding subjective dusk (on $D(\theta)$) and subjective dawn (on $L(\theta)$) (Figure 2.3E-F, *colored arrows*), which were only sampled with small numbers of points. Because the fluorescence polarization approach allows us to measure many conditions in an automated way over many days, and thus to disentangle phase shifts from period differences (Figure S2.5), these higher time resolution measurements better constrain the portions of the response functions critical for entrainment.

Given the observation that oscillator entrainment was sensitive to local shapes of $L(\theta)$ and $D(\theta)$, we wondered if midday tracking required a specific form of these response functions or if certain generic features are enough to account for midday tracking. Based on our observation that $L(\theta)$ and $D(\theta)$ in the KaiABC system are approximately linear in the regions

used during metabolic entrainment, we asked whether linear $L(\theta)$ and $D(\theta)$ were sufficient to result in a linear dependence of clock phase on day length.

Linear regions of step-response functions underlie proportional tracking of day length.

Consider a phase oscillator driven by light-dark cycles of period T and day length τ (Eq. 1). When the oscillator is entrained (phase-locked) to the light-dark cycle, the oscillator returns to the same state by the end of a full cycle. Starting from an initial phase θ_0, the clock accumulates phase $\omega_L\tau$ during the day, then experiences a phase shift of magnitude $D(\theta_\tau)$ at dusk, accumulates phase $\omega_D(T-\tau)$ at night, and finally responds to dawn with a phase shift $L(\theta_T)$:

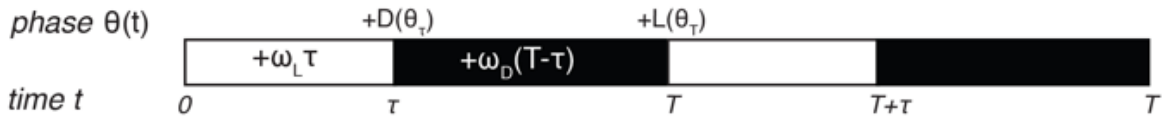

$$\theta_T = \theta_0 + \omega_L\tau + D(\theta_\tau) + \omega_D(T-\tau) + L(\theta_T), \qquad \text{(Eq. 1)}$$

where all angles are measured in units of cycles (1 cyc $= 2\pi$), and ω_L and ω_D are the oscillator frequencies in the light and dark, respectively. For stable entrainment, the effects of $L(\theta)$ at dawn and $D(\theta)$ at dusk must balance the phase accumulated by the oscillator, so that the phase returns to the same point at the end of each cycle.

his expression for the entrained clock phase scales linearly with day length if its derivative with respect to τ is constant. The simplest way to achieve this condition is if $L(\theta)$ and $D(\theta)$ are themselves linear functions of θ, such that $D(\theta) \approx -d(\theta - \theta_D)$ and $L(\theta) \approx -l(\theta - \theta_L)$ over the relevant range of clock times. If oscillator frequency is the same in light and dark, as

is approximately true for the Kai oscillator ($\omega_D/\omega_L = 0.93 \pm 0.01$, see Computational Methods), the peak time of the oscillation (measured in hours after dawn) can be expressed as $t_{pk} = m\tau + C$, with the slope $m(l,d) = d(1-l)/(d+l-ld)$ determined by the slopes of the linear $L(\theta)$ and $D(\theta)$ functions. If the day and night oscillator frequencies differ, we still obtain a linear dependence on day length, but with an altered expression for the proportionality constant *m* (see Mathematical Appendix). This expression for *m* imposes constraints on values of *l* and *d* required for an oscillator to track different portions of the day-night cycle. Figure S2.9 highlights such requirements on *l* and *d* for a midday-tracking clock.

To determine whether $L(\theta)$ and $D(\theta)$ for the Kai oscillator are in line with this mathematical requirement, we examined the linear portions of the step-response functions in Figure 2.3C-D. Indeed, the slopes of $L(\theta)$ and $D(\theta)$ from the fluorescence polarization assay ($l = 0.34 \pm 0.03$, $d = 0.38 \pm 0.05$) predict an *m* value consistent with our measurements of the entrained *in vitro* oscillator using the same method ($m(l,d) = 0.34 \pm 0.04$, calculated in the linear model vs. $m = 0.38 \pm 0.07$, measured) (Figure S2.9).

Because $L(\theta)$ and $D(\theta)$ are periodic functions on a circle, they cannot be linear everywhere with non-integer slope. However, maintaining the linear scaling of phase with day length only requires that both $L(\theta)$ and $D(\theta)$ be linear over the range of clock times when dawn and dusk occur, respectively, with the nonlinearities required to satisfy periodicity appearing at other times. The exact width of the linear region of $L(\theta)$ and $D(\theta)$ depends on *m* and the range of day lengths that the oscillator is required to track. For example, an oscillator capable of tracking midday (*m*=0.5) over a 12-hour range of day lengths requires that $L(\theta)$ and $D(\theta)$ be

linear over at least one quarter of the cycle. This criterion is met by the measured $L(\theta)$ and $D(\theta)$ (Figure 2.3C-D).

To further test whether entrainment of the Kai system can be described by this framework, we returned to our phase oscillator simulations (Figure 2.4C). When we replaced our experimentally measured $L(\theta)$ and $D(\theta)$ functions with linear approximations, the simulated oscillator exhibited a similar scaling of entrained phase over a wide range of day lengths (Figure S2.8A-B). The linear approximations work because the regions where the step response functions deviate strongly from linearity are avoided in our entrainment simulations (Figure S2.8C).

Together, these results indicate that the driven behavior of the cyanobacterial circadian clock in 24-hour cycles can be approximated as a simple oscillator that shifts in response to light-dark transitions with a sensitivity that varies linearly with phase. To test whether this linear mathematical framework holds more generally and to understand how the cyanobacterial clock responds to a broader range of environments, we sought to measure clock response to a variety of external conditions with both single and repeated light-dark transitions.

The behavior of the driven circadian clock across diverse conditions can be collapsed to a simple mathematical representation.

The phase oscillator model described above was inspired by the observation of linear scaling of clock phase in 24-hour days with various day lengths. The key model assumptions are (i) a unique clock cycle in the light and in the dark, (ii) rapid relaxation from one cycle to another when conditions change, and (iii) sensitivity to environmental changes that varies linearly with

clock time. While these assumptions hold, the model should be capable of describing the behavior of a biological clock in arbitrary fluctuating environments. For example, the response to a single dark pulse can be decomposed into sequential step-down and step-up responses.

To test the range of validity of this mathematical model, we used our LED array system (Figure 2.1A) to collect data on *S. elongatus* clock function in response to dark pulses administered at different clock times. This corresponds to a classical phase response curve analysis, a commonly used tool in circadian biology for characterizing the response of a biological clock to perturbations. We also probed clock responses to dark pulses of varying lengths (a so-called "wedge" analysis), and to repeated light-dark cycles with periods different from 24 hours. Our phase oscillator model predicts that the quantitative response to these various perturbations should all be related through the step-up and step-down functions (see Mathematical Appendix). One specific prediction of the model is that changing the time at which a dark pulse begins and the duration of a dark pulse should have separable linear effects on the oscillator, which would manifest as linear curves in phase response and wedge analyses. These experimental data and a fit of our linear model to the results are presented in Figure 2.5. The lines of best fit in Figure 2.5A-C were obtained from a single global fit to all of the datasets, with two fitting parameters underlying the slopes of the regression lines across all conditions (Mathematical Appendix). The overall agreement between the model and data suggest that limited data on clock response can be successfully extrapolated to other conditions using this approach.

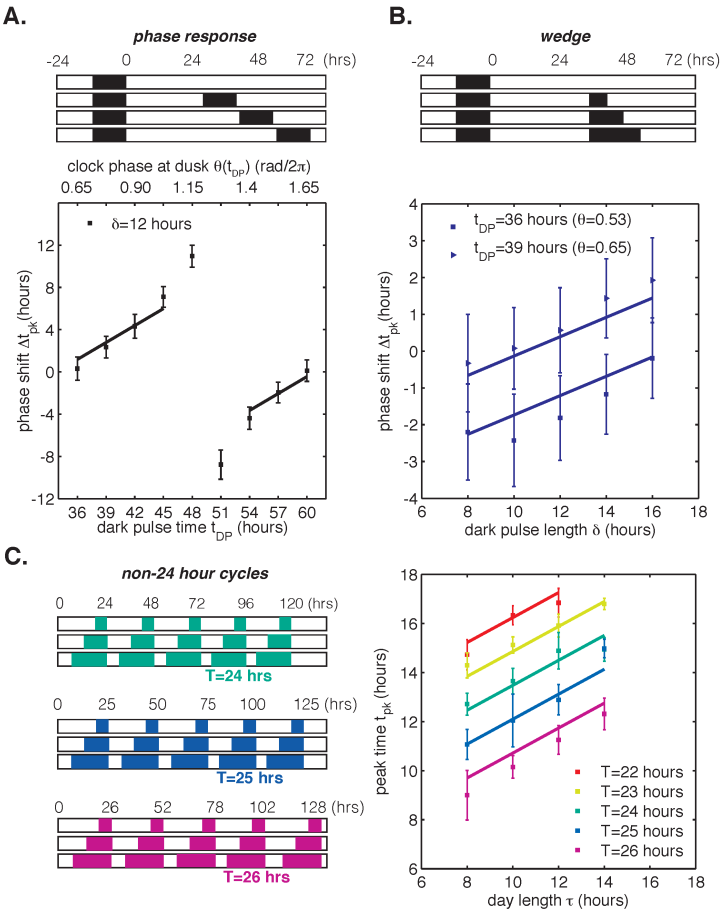

Figure 2.5. Phase oscillator model with linear phase shift functions predicts entrainment of the cyanobacterial clock to different light-dark (LD) patterns.
In all panels, error bars represent standard deviations (n=4-8 technical replicates per point). Lines are fit globally to all three datasets in (A)-(C). See Computational Methods for details.
(A) Phase resetting analysis. Phase shifts of bioluminescence rhythm (P_{kaiBC}::*luxAB*) due to 12-hour dark pulses (δ=12 hours) administered throughout the circadian cycle. The experimental protocol is represented schematically above the graph. Cells were exposed to one 12-hour dark pulse and released into constant light; 12-hour dark pulses were administered at the indicated times. $\theta(t_{DP})$ is the clock phase at beginning of the dark pulse, with θ=0 defined as clock phase at the trough of the bioluminescence rhythm.
(B) Wedge analysis. Phase shifts of bioluminescence rhythm (P_{kaiBC}::*luxAB*) due to dark pulses of varied length (δ=12-16 hours) administered at subjective dusk (36 or 39 hours after an initial 12 hour dark pulse). Clock phases at the beginning of the dark pulse are listed in parentheses; θ=0 is defined as clock phase at the trough of the bioluminescence rhythm. The experimental protocol is represented schematically above the graph as in (A).
(C) Seasonal response in non-24 hour environmental cycles. Cells were grown in LD cycles with period T=20-26 hours and day length τ=8-14 hours (see schematic on left). After five entraining cycles, cells were released into LL and the phase of the circadian rhythm was estimated by sinusoidal regression.

To understand the implications of these results, consider the phase response curve (PRC) for a 12-hour dark pulse (Figure 2.5A). Though phase response analyses frequently separate PRCs into regions of low sensitivity to perturbation ("dead zones") followed by highly nonlinear regions with large phase shifts, our model suggests a different interpretation [18,24–26]. Clock response is weakest at times when nightfall is expected (t = 36 and 60 hours) and increases gradually with clock time. The slowly changing regions of the PRC are well described by line segments with the same slope, in agreement with our model based on linear step-response functions $L(\theta)$ and $D(\theta)$. The "breakpoint" in the PRC near 50 hours is a consequence of the fact that these periodic step-response functions cannot be linear everywhere with non-integer slope, as discussed earlier.

In other words, a circadian clock capable of tracking midday over a wide range of day lengths is expected to have a PRC that is approximately linear over many hours except for a narrow region of rapid change that is required to satisfy periodicity. Indeed, in simulations where $L(\theta)$ and $D(\theta)$ are linear everywhere except for a discontinuous jump, the PRC for a long dark pulse appears as a straight line except for a single breakpoint (Figure S2.10). Near the breakpoint, small changes in the timing of darkness result in large differences in phase shifts, and we would expect to find this region of the PRC at a clock time when such a perturbation is least likely to occur naturally. In the dark-pulse PRC for *S. elongatus*, the breakpoint near 50 hours occurs when prolonged darkness is improbable (Figure 2.5A). The maximal phase shift in a PRC can be a useful tool to characterize clock mutants, but our analysis highlights that these regions are unlikely to be experienced in natural conditions and may exist only as consequences of periodicity constraints.

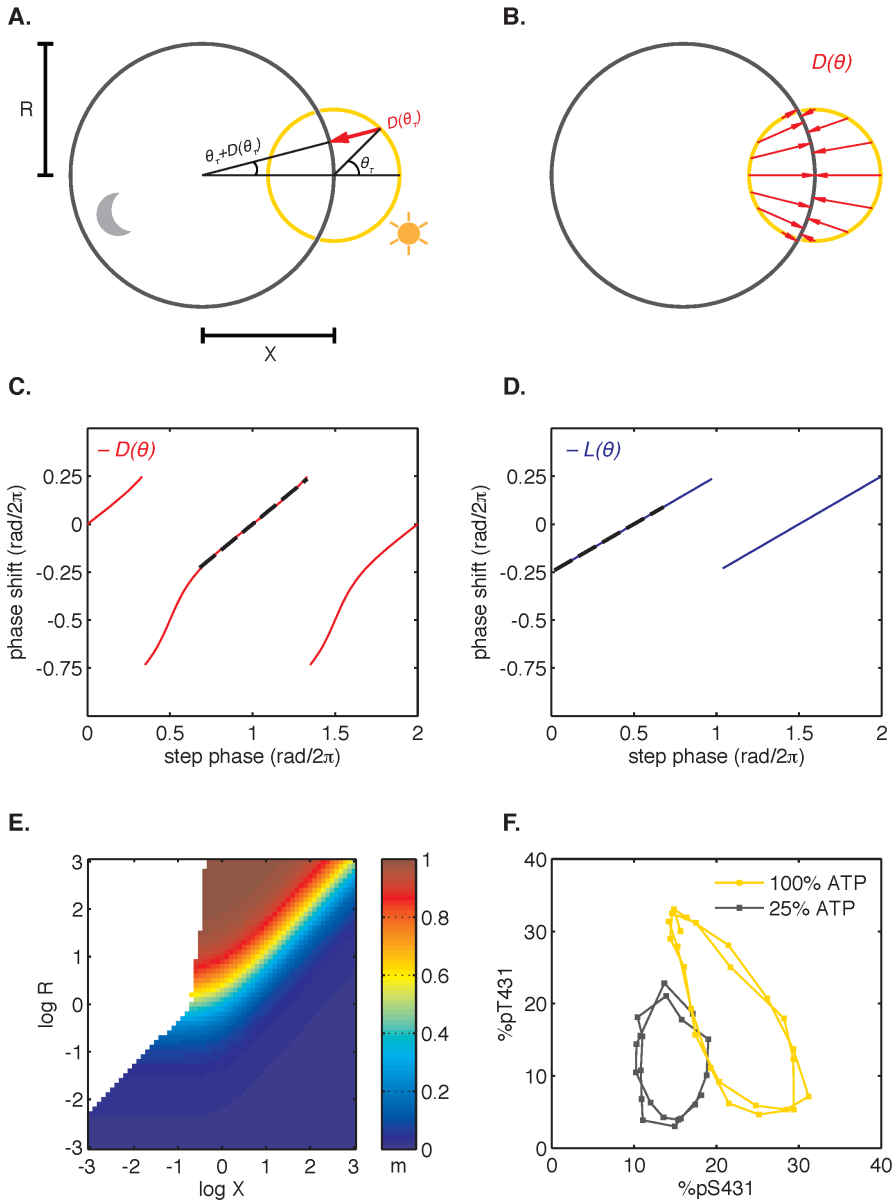

Figure 2.6. Nearly linear step response functions can arise from the relative geometry of day and night limit cycles.
(A) Geometric model of oscillator phase resetting. During the day, the oscillator runs with constant angular velocity along the daytime orbit (*yellow*), which has unit radius and is centered at the origin. At dusk, the oscillator transits to the nighttime orbit (*black*), which has radius R and is displaced from the daytime orbit by X units. In the limit where the nighttime orbit is strongly radially attracting, we can approximate oscillator response to the light-dark transition ($D(\theta_\tau)$, *red arrow*) as an instantaneous jump from phase θ_τ on the daytime orbit towards the center of the nighttime cycle, resulting in phase $\theta_\tau + D(\theta_\tau)$ on the night orbit.

(Figure 2.6 continued) (B) Simulation of oscillator phase shifts due to light-dark transitions at different phases on the day orbit (*red arrows*) for $R = 2$, $X = 2$. For limit cycle geometries with $X \approx R$, phase angles on the day orbit are compressed to an arc on the night limit cycle that subtends a smaller angle. See Computational Methods for calculation details.
(C and D) Simulations of $L(\theta)$ and $D(\theta)$ step response functions arising from the geometric arrangement of day and night cycles in (B). Linear regions of $L(\theta)$ and $D(\theta)$ are marked with black dashes. See Computational Methods and Mathematical Appendix for calculation details.
(E) Heat map of the slope *m* of the approximately linear relationship between entrained phase and day length, plotted as a function of *X* and *R*. In white regions, the oscillator does not entrain stably or the oscillator does not show linear scaling of phase with day length. Slope determined from simulations of oscillator entrainment to 24-hour driving cycles of day length τ=6-18 hours. See Computational Methods for details.
(F) Limit cycles traversed by the KaiABC oscillator *in vitro* in metabolic conditions mimicking day (*black*, 100% [ATP]/([ATP]+[ADP])) and night (*yellow*, 25% [ATP]/([ATP]+[ADP])). Oscillations in KaiC phosphorylation on Ser431 and Thr432 are replotted from data in Phong et al. (2013) [17].

A geometric interpretation of oscillator response to varying day length.

Finally, we asked how step response functions with linearly increasing sensitivity are related to the mathematical structure of the oscillator and ultimately to the underlying molecular mechanism. Do step response functions with these properties arise generically, or do they require fine-tuned choices of parameters? To address these issues, we considered the simplest possible dynamical representation that allows for distinct day and night clock cycles. In this model, the clock cycle during the day is represented by a circular limit cycle with unit radius, and the clock time is defined by the angular coordinate of the oscillator on this limit cycle (Figure 2.6A). The effect of darkness is to deform the limit cycle, transforming the daytime orbit to a nighttime orbit. For simplicity, we assume this night cycle lies in the same plane as the day cycle and is also circular, but may be offset relative to the day cycle and have a distinct radius (Figure 2.6A).

After a transition from one condition to the other, the system state must evolve to the new limit cycle. We suppose that each cycle is very strongly radially attracting. That is, when the

system is in a state off the limit cycle, it is rapidly pulled to the closest point on the cycle. Under these conditions, the step transitions from one cycle to another are determined purely by geometry (Figure 2.6A), and we can connect this picture with the phase-only description we used to analyze the experimental data. Here, linearly increasing sensitivity of a step response has a simple geometric interpretation: when the two cycles are displaced from each other, a step transition maps an arc of one cycle onto an arc of the other cycle that subtends a smaller angle than the original (Figure 2.6B). Thus, step transitions compress or expand angular distance when mapping one circle onto another. The slopes of the step response functions are thus given by the compression factor in this mapping (Figure 2.6C-D, Figure S2.12; see Mathematical Appendix).

To determine how the entrained clock phase depends on geometry in this model, we simulated step transitions and then calculated the slope m of clock phase versus day length (Figure 2.6E). This calculation indicates that midday tracking ($m \approx 0.5$) requires that the separation between the light and dark cycles is comparable to the radius of the cycle ($R \approx X$). This requirement can be understood intuitively by considering three cases where orbits have the same center-to-center separation ($\log X = 0.5$) but different sizes (Figure S2.9). Dusk transitions are strongly resetting for this choice of X, but the strength of dawn resetting varies with the relative size of the orbits. Dawn-tracking entrainment results when the night orbit is much smaller than the day orbit ($l \approx 1$) and dusk-tracking entrainment results when the night orbit is much larger ($l \approx 0$, $d \approx 1$), in accord with how m varies as a function of l and d (Figure S2.9). When the size of both orbits is similar to their center separation, the oscillator can track intermediate phases, such as midday.

Though this model makes a simple connection between attractor geometry and entrainment, it also makes a number of simplifying assumptions about oscillator dynamics that may not hold true for real biological clocks, such as instant transitions between cycles, perfectly circular orbits and constant angular frequencies along each cycle. To test the consequences of relaxing these assumptions, we used a dynamical model where the evolution of the system is described explicitly (see Computational Methods). Our simulations in Figure S2.12 show that in these more complicated scenarios the geometric arrangement of day and night cycles remains a key determinant of the slope of entrained clock phase as a function of day length. Indeed, in all cases we studied, midday tracking was only possible for geometries where the center-to-center distance between the day and night cycles was comparable to the radius of the larger orbit ($R \approx X > 1$).

This dynamical systems perspective allows us to reframe conditions on the underlying biochemical mechanisms that can produce the observed midday tracking behavior. Changes in the external environment caused by transitions between night and day should affect the oscillator in such a way that the period remains close to 24 hours, but that the limit cycle is shifted by an amount comparable to its radius. The relative geometry of the two limit cycles, which is determined by the mechanisms that couple the environment to the clock, must be fine-tuned to give a specific slope for the entrained phase. Indeed, when we plotted experimentally determined orbits of the purified KaiABC oscillator on axes showing the extent of phosphorylation of two key sites, we observed an arrangement similar to the expected geometry ($R \approx X$) using nucleotide conditions that simulate either day or night (Figure 2.6F) [6,17].

DISCUSSION

Though circadian clocks are defined in part by their ability to continue to cycle in constant environments, the defects associated with clock mutants are often most apparent when organisms are faced with fluctuating environments [27–31]. Thus, an important challenge is to understand how biological clocks respond to the cycling environments found in nature, and how they function to appropriately schedule gene expression and behavior.

For most organisms, there is an asymmetry between day and night, in terms of food availability, predation risk, etc., so that the need to carry out certain activities diurnally or nocturnally presents changing demands as the length of the day varies throughout the year. The situation is especially dramatic for cyanobacteria because there is an extreme metabolic contrast between day and night. We found that *S. elongatus* contends with these challenges using a clock that tracks the middle of the day.

The ability of circadian systems to keep track of the phase of the light-dark cycle has been long recognized in plants, insects, rodents and higher mammals [1,32–36]. Though molecular mechanisms that give rise to these entrainment behaviors are still being uncovered, analysis of circadian clock models has found that the presence of multiple feedback loops in complex clocks determines the number of points in the driving cycle that the oscillator can track simultaneously, by allowing different internal phase relationships between the clock components [37]. For example, the multi-feedback loop clocks in plants are able to track phases of both dawn and dusk [33].

Consistent with this picture, we find that the core circadian oscillator in cyanobacteria, which relies on a single posttranslational feedback loop, keeps track of a single phase—the

midpoint of the day portion of the cycle, a property described in our mathematical framework as a linear scaling of entrained phase with day length with slope $m \approx 0.5$. Why might keeping track of midday be useful for a photosynthetic organism with a simple clock? Clock-controlled gene expression in *S. elongatus* tends to be bimodal, with most genes falling into subjective dawn or dusk classes. Because the biosynthetic capacity of *S. elongatus* is severely limited in darkness, the midday tracking effect we describe here could be a mechanism to ensure that biosynthetic resources are partitioned in a balanced way between the dawn and dusk genes, even as the day length changes with the seasons (Figure S2.13). In particular, clock-driven transcription in this organism has been shown to implement a switch between anabolic and catabolic carbon metabolism, suggesting that a role for the midday tracking we observe here is to ensure balanced growth by timing this switch appropriately in days of different length [38].

The ability to reconstitute this effect *in vitro* by delivering metabolic pulses to the purified Kai proteins indicates that midday tracking is not necessarily achieved through additional feedback mechanisms in the cell, but appears to be a property of the clock proteins themselves. The purified clock responds to metabolic steps with phase shifts that are linear functions of the previous phase. The slopes of these response functions are presumably tuned to give an appropriately entrained clock phase. Notably, linear responses have also been observed for the Kai oscillator following temperature steps, suggesting that this is a general reaction of the system to inputs [39].

The mathematical framework that we describe here has deep similarities to the theory of nonparametric entrainment developed by Colin Pittendrigh [40–42]. His work motivated a theory of entrainment to diurnal cycles mediated by instantaneous phase shifts at dawn and dusk, which

can be summarized by a phase response curve. Daan and Pittendrigh suggested that the ability of the clock to track specific phases of the day-night cycle in different seasons depends on the shape of the phase response curve as well as the difference between the free-running period of the clock and the period of the day-night cycle [40,43]. Our decomposition of driven behavior of the KaiABC oscillator into individual step responses is in the spirit of this classic paradigm.

We note that a mismatch between the free-running clock period and the external cycle is not required for stable entrainment in our phase oscillator model (see Mathematical Appendix). Instead entrainment can be achieved from the opposing effects of the step-up and step-down phase shifts, which occur at different clock times in days of different length. The step-response curves underlying entrainment in our model are nonlinear functions of clock phase, but they can be successfully approximated by linear functions over the interval of clock phases used during entrainment. Our simulations suggest that the slopes of these locally linear functions are key determinants of entrained phase, along with changes in clock period in daytime and nighttime conditions. Successful prediction of how the *in vitro* oscillator entrains to rhythmic environments is due in large part to the ability to map out the step-response curves with high temporal resolution. In this study, we achieve this by measuring free-running oscillations in an automated way using the fluorescence polarization probe.

Though there are likely other effects at play in natural environments, as long as the system can be described by fast relaxation back to distinct limit cycles in day and night, instantaneous step-response descriptions of the kind used here should be applicable. The data reduction achieved in our linear model holds the promise of predicting the behavior of the

circadian rhythms in many time-varying environments from a minimal data set that characterizes oscillator response, and may be applicable to clocks in many organisms.

Though the biochemistry of even the simplest circadian clock is complex, our analysis suggests that a key determinant of entrained behavior is how the clock limit cycle is deformed by coupling to the environment. Viewed in this way, the entrainment properties of circadian oscillators arise from simple features of the geometry of the limit cycle attractor that could be measured in any organism. The concept that the phase-shifting of oscillators can be studied in terms of their geometric properties was initially developed by Winfree [44]. In this context, it would be informative to analyze the geometric arrangement of day and night limit cycles of clock gene transcripts in other species. An important goal for the future is to understand how the biochemical properties of the clock components in cyanobacteria and other organisms achieve the effect of shifting the limit cycle without changing the period, allowing us to use dynamical systems theory to bridge the gap between molecular detail and systems-level clock phenotypes.

SUPPLEMENTARY FIGURES

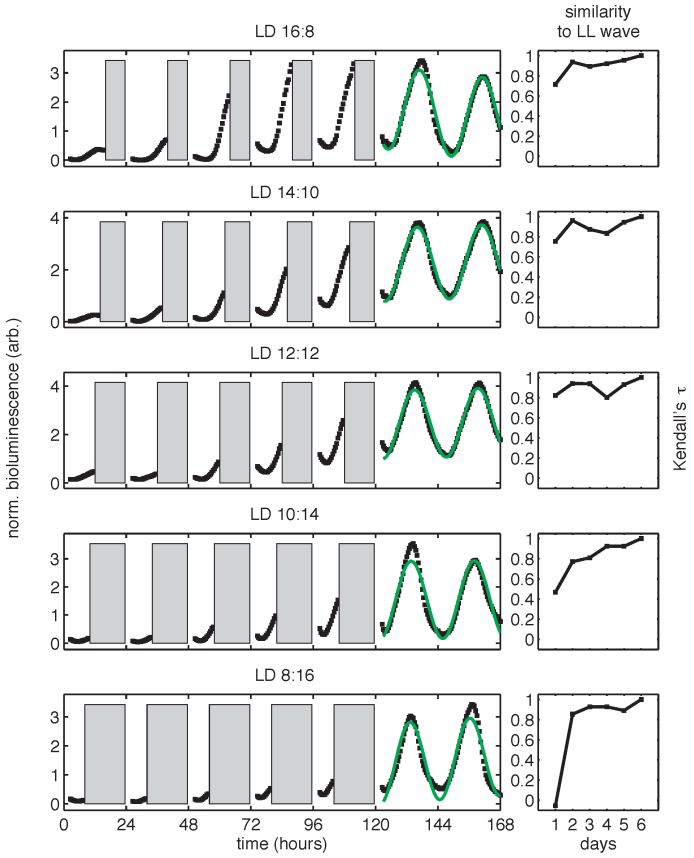

Figure S2.1. Bioluminescence recordings from *P_{kaiBC}::luxAB* reporter in light-dark cycles. (*left*) Selected bioluminescence traces (*P_{kaiBC}::luxAB, black*) recorded from individual wells of the 96-well LED array device in conditions simulating day-night cycles of different day length (same dataset as in Figure 2.1B-C). Data recorded in the dark were omitted from analysis (*gray bars*). Each trajectory was normalized to the mean and variance of the bioluminescence signal recorded after the release into constant light, and trajectories recorded after release into constant light were fit to sinusoids (*green*). For illustration purposes here, trajectories were aligned to zero baseline. See Computational Methods for fitting details. (*right*) Similarity between the bioluminescence rhythms (*P_{kaiBC}::luxAB)* recorded during light-dark entrainment and after release into free running conditions. Nonparametric correlation coefficient (Kendall's τ) between bioluminescence trajectories recorded in the light during entrainment (days 1-5) and the corresponding time period after release into constant light (e.g., a 16-hour window in LL for LD 16:8). See Computational Methods for details.

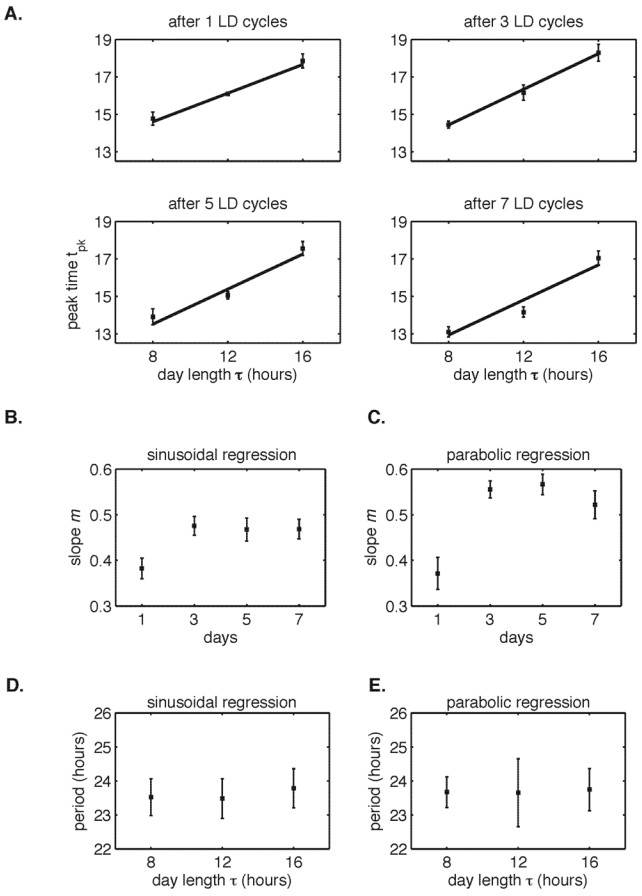

Figure S2.2. The circadian rhythm of *S. elongatus* rapidly entrains to 24-hour diurnal cycles with 8-16 hours of daylight.
(A) Peak times of P_{kaiBC}*::luxAB* reporter after release into LL from 1-7 LD cycles of different day length (LD 8:16, LD 12:12 or LD 16:8), as estimated by sinusoidal regression. Error bars represent the standard deviation (σ) of technical replicates (n=6-8 replicates per condition). Lines mark linear fits to the data.
(B) Slope *m* of clock phase scaling with day length stabilizes after three light-dark cycles. Slope of linear fits in (A) plotted against day length in diurnal cycles. Error bars mark uncertainty in fit slope (±σ).
(C) Slope *m* of clock phase scaling with day length, as estimated by parabolic regression (see Computational Methods).
(D and E) Free-running period of P_{kaiBC}*::luxAB* reporter rhythms, as estimated from sinusoidal fits (D) or local parabolic fits (E), recorded in continuous light after entrainment to 24-hour cycles with 8, 12, or 16 hour of daylight.

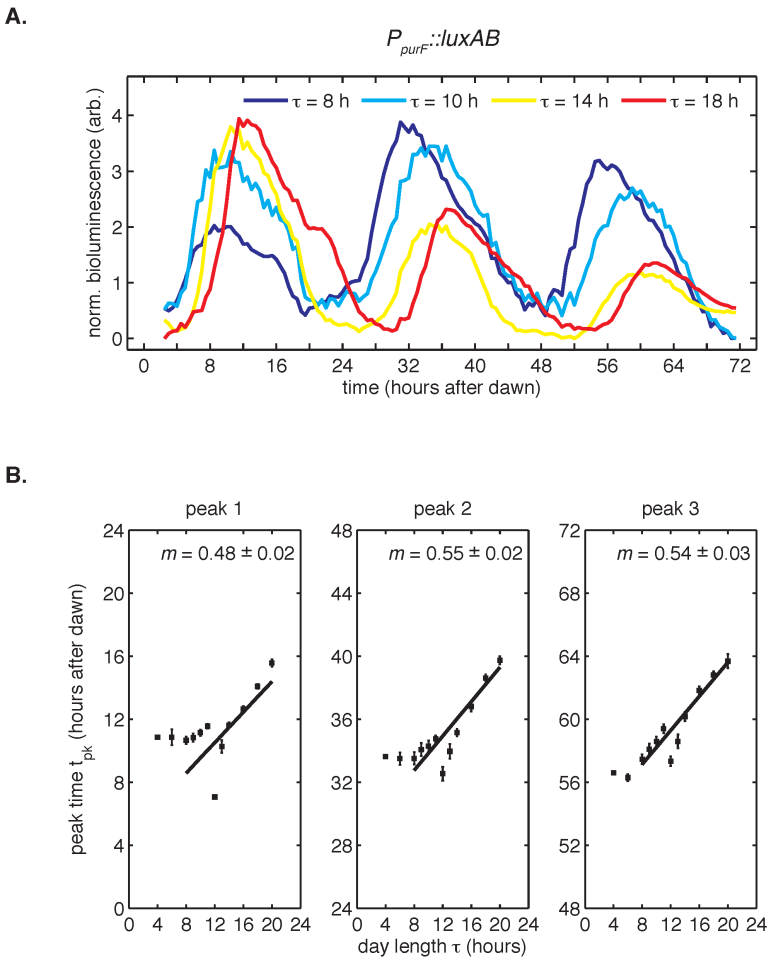

Figure S2.3. Bioluminescence recordings from *P_{purF}::luxAB* reporter in light-dark cycles.
(A) Rhythms in bioluminescence in continuous light recorded from a dawn gene reporter (*PpurF::luxAB)* after entrainment to 24-hour light-dark cycles of different day length τ (LD 8:16, LD 10:14, LD 14:10, LD 18:6). Following the protocol in Figure 2.1, cells received five light-dark cycles and were then placed under continuous illumination. Bioluminescence trajectories from first 72 hours after release into constant conditions were aligned to zero baseline and normalized to unit variance.
(B) Peak times of the *PpurF::luxAB* reporter after release into constant light after five LD cycles of different day length (LD 4:20 to LD 20:4). Peak times were determined by local parabolic regression (see Computational Methods). Error bars represent standard errors of technical replicates (n=4-8). Straight lines represent linear fits to data from wells entrained to day lengths at least 8 hours long.

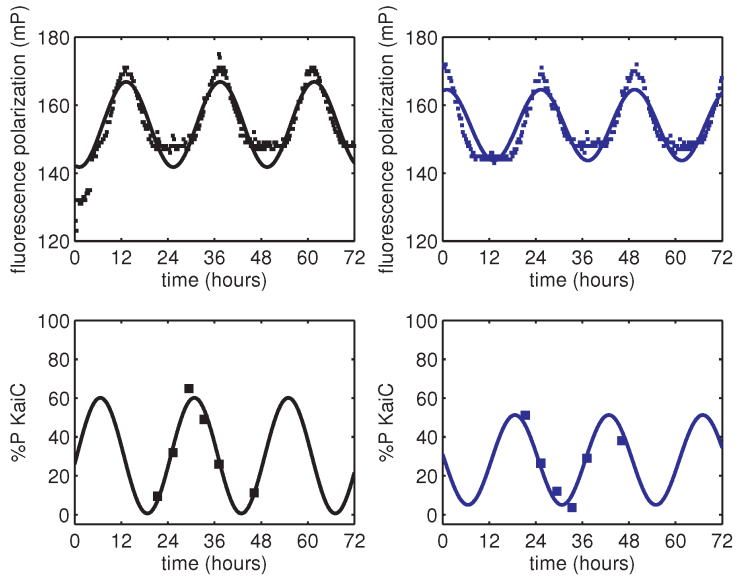

Figure S2.4. Validation of KaiB fluorescence polarization reporter against KaiC phosphorylation rhythm.
(*top*) Fluorescence polarization of KaiABC mixture probed with fluorescently-labeled KaiB exhibits ≈24-hour rhythms (*black and blue squares*). (*bottom*) KaiC phosphorylation rhythm of the same reaction mixtures as in the top panel (*black and blue squares*). *Black vs blue markers* show data from two identical reactions started at different times. Curves show best-fit sinusoids, where all reactions share a common period; the phase offset between out of phase reactions was also a shared parameter in fits to polarization and phosphorylation datasets. This experiment was performed once.

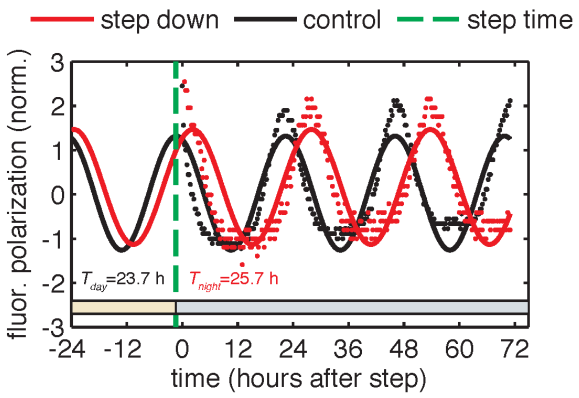

Figure S2.5. Example calculation of phase shifts in response to metabolic step transitions.
Phase shifts are computed from the difference in phase of the control reaction and the perturbed reaction evaluated at the time of the step. Phase of each reaction at the time of the step (*green dashed line*) is calculated based on the sinusoidal fit to the normalized fluorescence polarization trajectory for that reaction. Periods of the oscillator in day and night conditions were fit globally to all reactions measured in one experiment. See Computational Methods for fitting details.

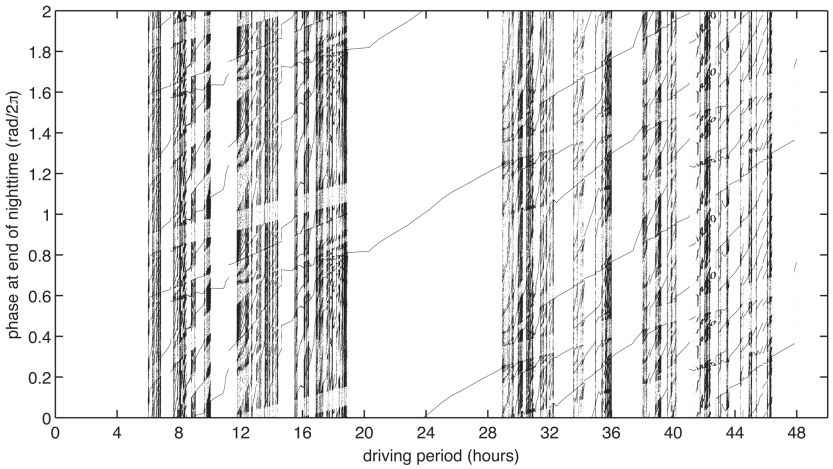

Figure S2.6. Experimentally-measured step-response functions predict entrainment to driving periods near 24 hours.
Entrainment simulations with driving periods 4-48 hours were performed for 1000 cycles, and phases at the end of nighttime (immediately before the action of *L*) of the last 920 cycles were plotted. Simulation results are double-plotted along the vertical axis for clarity. In each simulation, the oscillator runs at constant angular speed in the light and dark, and experiences instantaneous phase shifts at dawn and dusk, according to the values of *L* and *D*. Refer to Figure 2.4A for an illustration of a single entrainment simulation.

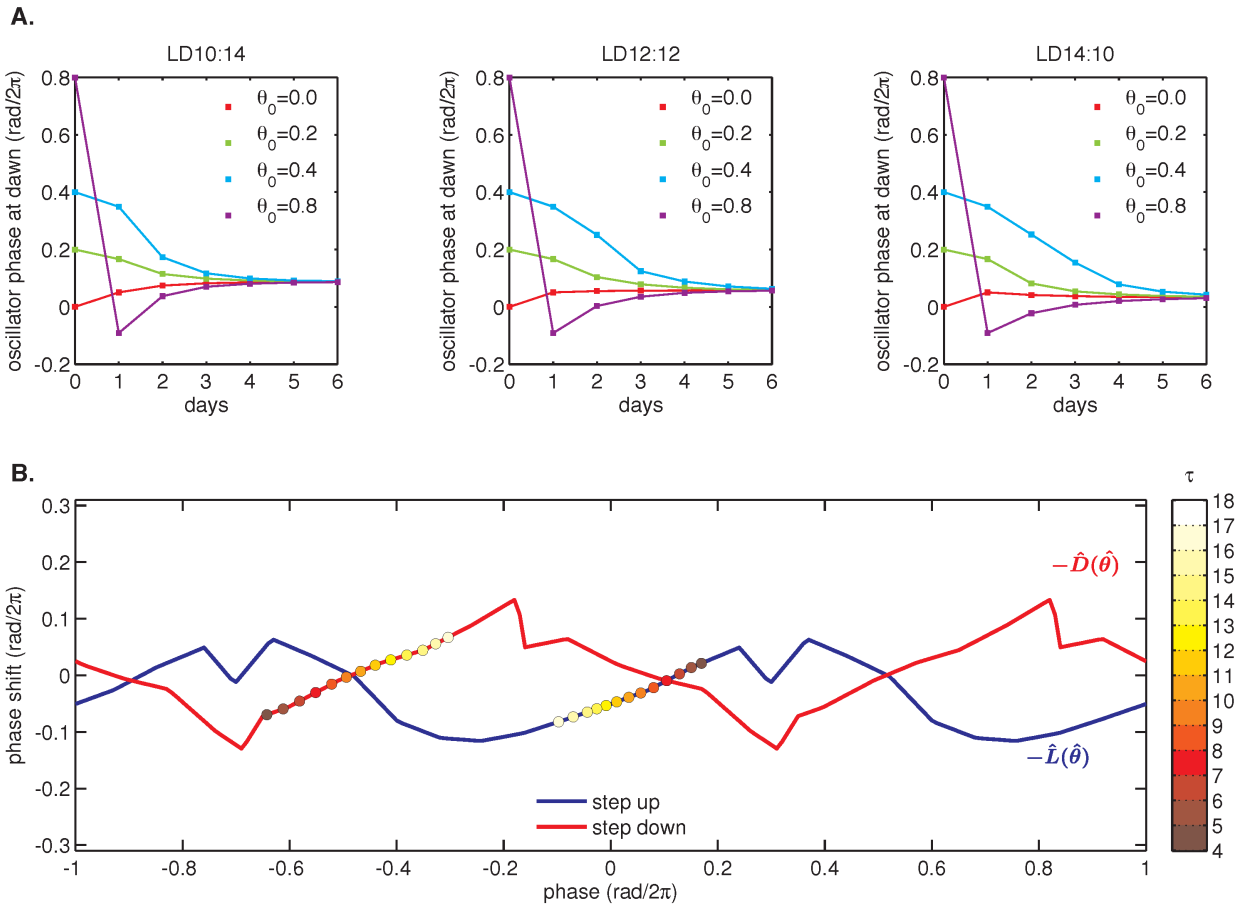

Figure S2.7. Example simulation of a phase oscillator governed by one set of experimentally determined *L(θ)* and *D(θ)* functions and subjected to a driving cycle.
(A) The phase oscillator reaches stable entrainment within 3-5 light-dark cycles (τ=10-14 hours) for a wide range of starting phases. Simulation parameters same as in Figure 2.4B; *L(θ)* and *D(θ)* as shown in (B) below.
(B) Example pair of step response functions, denoted $\hat{L}(\hat{\theta})$ and $\hat{D}(\hat{\theta})$, measured using the fluorescence-polarization reporter of KaiB-KaiC binding (magenta and blue curves in Figure 2.3C-D). Colored circles mark phases corresponding to dawn (on $\hat{L}(\hat{\theta})$) and dusk (on $\hat{D}(\hat{\theta})$) in seasonal entrainment simulations of different day length τ (see color bar). θ=0 refers to the phase when the minimum of the KaiC phosphorylation rhythm occurs. See Computational Methods for details.

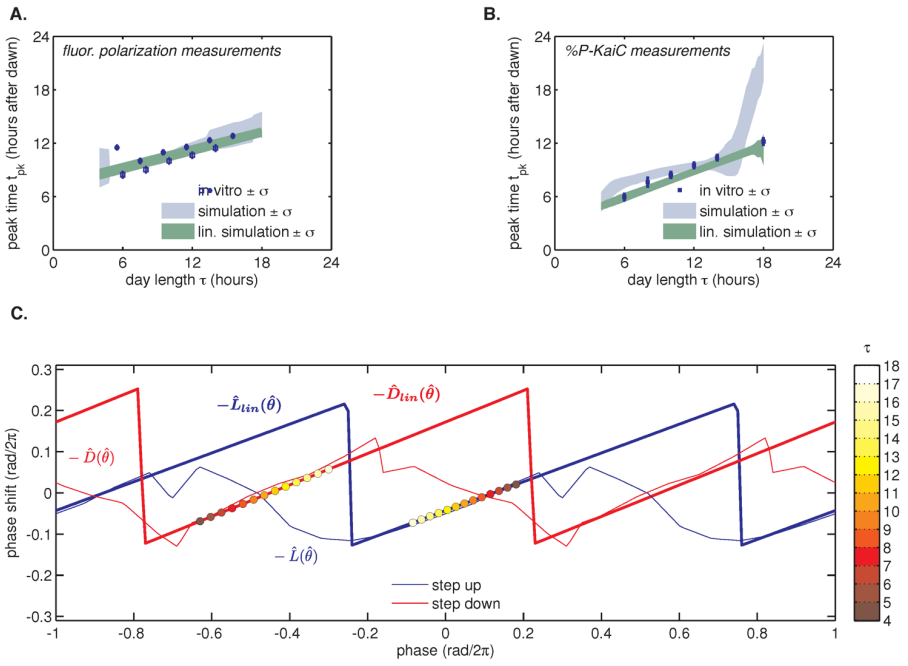

Figure S2.8. Simulations of seasonal entrainment for a phase oscillator driven by linearized step-response functions (L_{lin} and D_{lin}).

(A) Simulated seasonal response of phase oscillators governed by the four possible combinations of nonlinear $\hat{L}(\hat{\theta})$ and $\hat{D}(\hat{\theta})$ step-response functions in Figure 2.3(C-D) (blue shaded areas) and their linearized versions $\hat{L}_{lin}(\hat{\theta})$ and $\hat{D}_{lin}(\hat{\theta})$ (shaded green areas). In simulations, tpk is defined as the time when oscillator phase θ equals 0.5 rad/2π, corresponding to the peak of KaiC phosphorylation. In vitro measurements overlaid in blue as in Figure 2.4C.

(B) Simulated seasonal response of phase oscillators governed by step-response functions measured for an independent preparation of clock proteins using SDS-PAGE analysis of KaiC phosphorylation Figure 2.3(E-F). Shaded areas correspond to standard deviations determined by bootstrapping (see Computational Methods). Blue squares show seasonal response measured in the purified KaiABC oscillator using the same preparation of proteins and measured via SDS-PAGE (Figure 2.2C). tpk is defined as in (B) above. Error bars represent uncertainty of fit phase from sinusoidal regression.

(C) Example pair of step-response functions $\hat{L}(\hat{\theta})$ and $\hat{D}(\hat{\theta})$ and their linearized versions, $\hat{L}_{lin}(\hat{\theta})$ and $\hat{D}_{lin}(\hat{\theta})$, used in simulations in (A) above and measured using the fluorescence-polarization reporter of KaiB-KaiC binding (magenta and blue curves in Figure 2.3C-D). Colored circles mark stably entrained phases corresponding to dawn (on $\hat{L}(\hat{\theta})$) and dusk (on $\hat{D}(\hat{\theta})$) in simulations of different day length τ (see color bar). θ=0 refers to the minimum of KaiC phosphorylation rhythm. See Computational Methods for details.

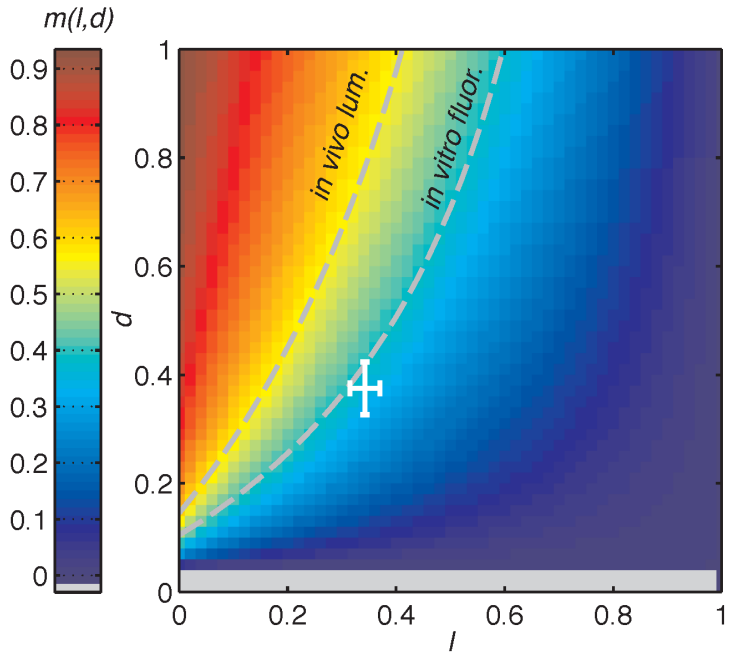

Figure S2.9. Dependence of the slope of entrained phase on the slopes of step response functions.

Heat map of slope *m*, describing the scaling of oscillator peak time with day length, as a function of the slopes *l* and *d* of linear $L(\theta)$ and $D(\theta)$ step response functions and oscillator frequencies in light and dark (ω_D and ω_L) (see main text and Mathematical Appendix). This relationship is described by $m(l,d) = 1 - \frac{-(1-l)\times(\omega_D/\omega_L)}{d+l-ld} - \frac{1}{d+l-ld}$. The ratio of oscillator frequencies in light and dark was estimated to be $\frac{\omega_D}{\omega_L} = 0.94$ based on the analysis of datasets in Figure 2.3(C-D). Dashed isolines connect all points with *m*=0.53 (*left*) and *m*=0.38 (*right*), corresponding to our estimates of scaling coefficients *in vivo* and *in vitro* Figure 2.2C). The approximate range of values of *l* and *d* estimated from experimental measurements in Figure 2.3(C-D) is indicated by the white crosshair. Crosshair lengths represent mean±standard deviation of estimates of *l* and *d* determined by bootstrapping, as described in Computational Methods.

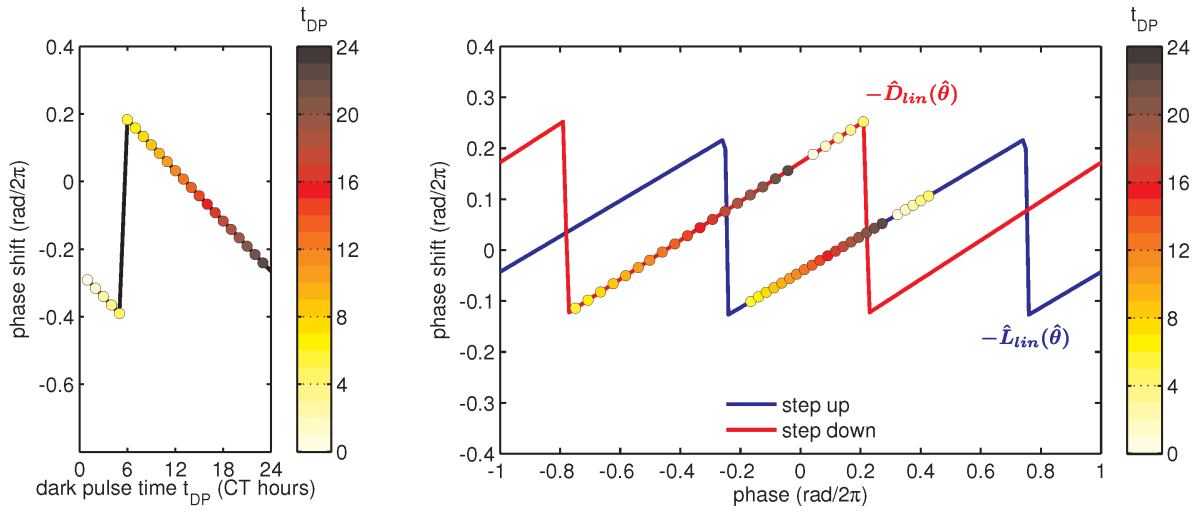

Figure S2.10. Simulation of a phase-resetting curve.
(left) Simulated phase-resetting curve due to a 12-hour dark pulse for a phase oscillator governed by linear step-response functions $\hat{L}_{lin}(\hat{\theta})$ and $\hat{D}_{lin}(\hat{\theta})$ (*right*), as in in Figure S2.8. Colored circles indicate phases at the beginning of the dark pulse (see color bar). θ=0 refers to the trough of the KaiC phosphorylation rhythm.

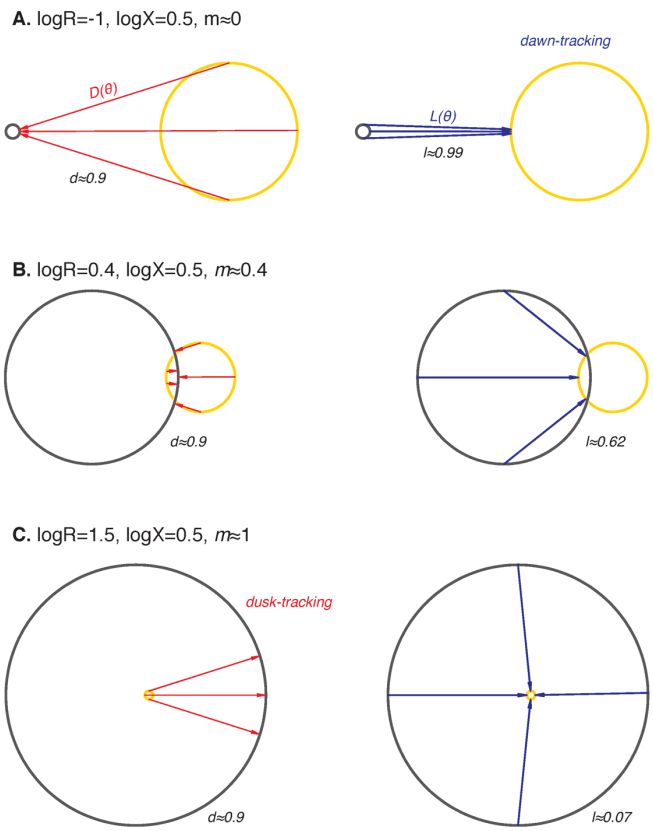

Figure S2.11. Illustrations of limit cycle geometries that give rise to step-response functions *L(θ)* and *D(θ)* with different slopes.
Illustrations of limit cycle geometries that give rise to step-response functions $L(\theta)$ and $D(\theta)$ with different slopes, resulting in dusk-, dawn-, or midday-tracking entrainment. In all schematics, the day orbit (*yellow*) is centered at the origin and has radius 1. The night orbit (*black*) has radius R and is displaced from the day orbit ($\log X = 0.5$) units. Light-dark ($D(\theta)$) and dark-light ($L(\theta)$) transitions are indicated by *red* and *blue arrows*, respectively.
(A) When the night cycle is much smaller than the day cycle ($R << 1$), both dawn and dusk are strongly resetting (l≈1, d≈1). Because all phases on the night orbit are mapped to a small range of phases on the day orbit, oscillator phase at dawn is independent of day length during entrainment (m≈0, dawn-tracking).
(B) When the sizes of day and night orbits are comparable ($R \approx 1$), the slopes of $L(\theta)$ and $D(\theta)$ depend on the fine-tuned arrangement of the orbits. Generally, both $L(\theta)$ and $D(\theta)$ exert entraining effects in this regime ($l > 0$, $d > 0$). The slope of entrained phase with day length depends on both l and d, according to $m(l, d) = d(1 - l)/(d + l - ld)$.
(C) When the night cycle is much bigger than the day cycle ($R >> 1$), dusk is strongly resetting, but dawn transitions have little effect on clock phase (l≈0, d≈1). Entrainment to repeated light-dark cycles maps clock phases on the night orbit to a shrinking range of angles, leading to dusk-tracking entrainment (m≈1).

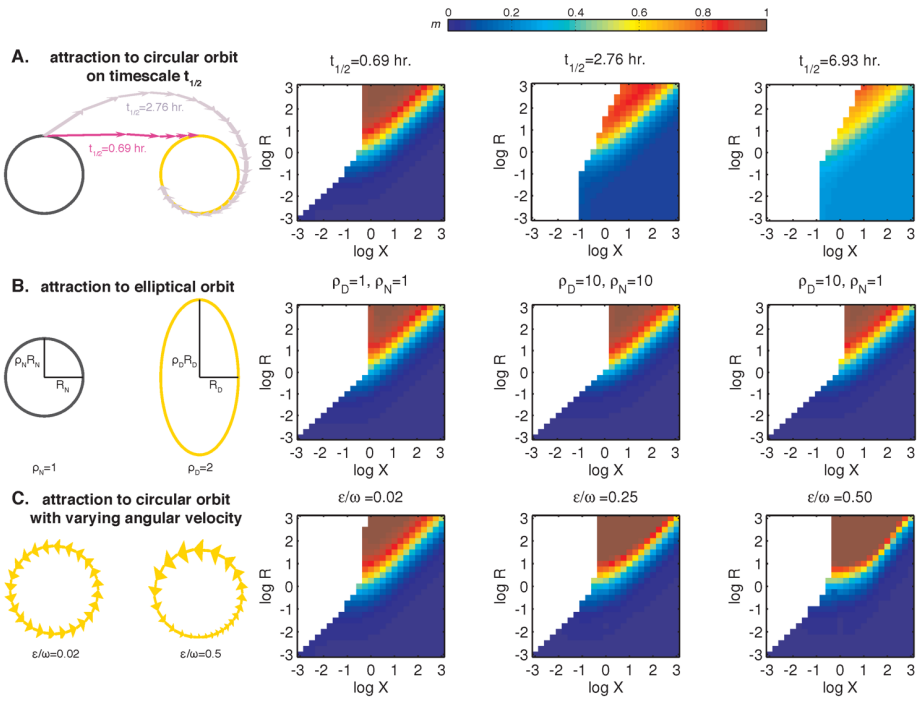

Figure S2.12. The relative size (*R*) and center-to-center distance (*X*) of day and night limit cycles are major determinants of entrained behavior.

Heat maps of *m*, the slope of the approximately linear relationship between entrained phase and day length, are plotted as a function of *X* and *R* on the same color scale as in Figure 2.6E. See Computational Methods for simulation details.

(A) Entrainment simulations with non-instantaneous jumps between day and night limit cycles. The half-times $t_{1/2}$ for transition between the circular orbits are indicated above the heat maps. Schematic on the left illustrates the evolution of the oscillator from a point on the night limit cycle to the day limit cycle in two scenarios with different relaxation times. Each arrow represents the displacement of the oscillator in 1 hour.

(B) Entrainment simulations for day and night limit cycles of varying ellipticity. The ratios of the major axis length to the minor axis length of the day and night orbits (ρ_D and ρ_N) are indicated above the heatmaps. In these simulations we considered strongly attracting orbits ($t_{1/2} = 0.069$ hours) oriented with their major axes perpendicular to the separation between their centers.

(C) Entrainment simulations for day and night limit cycles with non-constant angular velocities. In these simulations we considered circular orbits for both day and night limit cycles. Orbit attraction timescale was set to $t_{1/2} = 0.69$ hours. The variability in angular speed $\dot{\theta}$ throughout the cycle is given by $\dot{\theta} = \omega\ (1 + \frac{\varepsilon}{\omega}\sin \omega t)$. Schematic on the left illustrates the evolution of the oscillator along day limit cycle in two scenarios with different values of $\frac{\varepsilon}{\omega}$. Each arrow represents the displacement of the oscillator in 1 hour; size of the arrowheads illustrates changes in angular velocity throughout the cycle (not to scale).

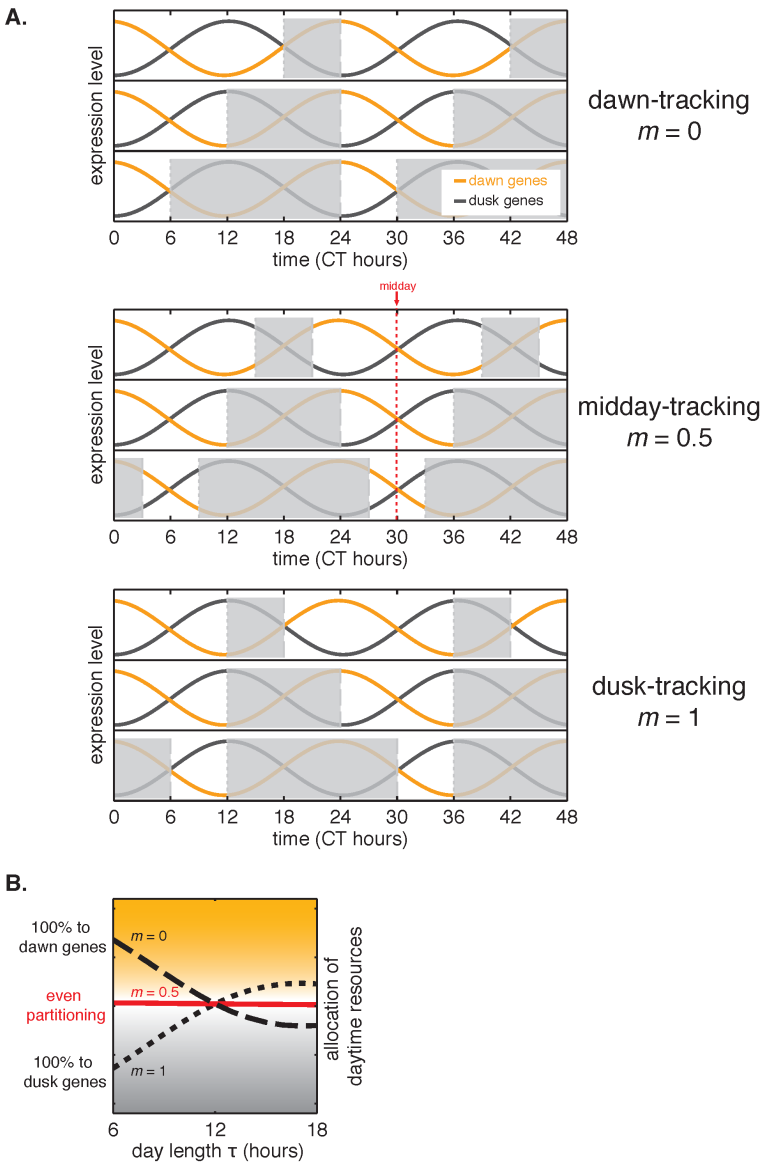

Figure S2.13. Interpretation of *m*, the slope of the approximately linear relationship between entrained phase and day length.
(A) The value of *m* dictates whether the circadian rhythm aligns to dawn (*m* = 0), dusk (*m* = 1), or an intermediate point of the day-night cycle (e.g., midday for *m* = 0.5). Orange and gray curves show sinusoidal fits to average transcriptional profiles of dawn and dusk genes in *S. elongatus* based on data from Vijayan et al. (2009) [50]. Gray bars indicate night in light-dark cycles for *m* = 0, 0.5, and 1.
(B) Tracking midday as the day length varies represents a strategy to balance biosynthetic resources between dawn and dusk transcriptional programs. For each value of *m*, the corresponding curve shows a numerical estimate of the relative fraction of dusk and dawn gene expression that occurs during the day in *S. elongatus* (arbitrary units, see Computational Methods).

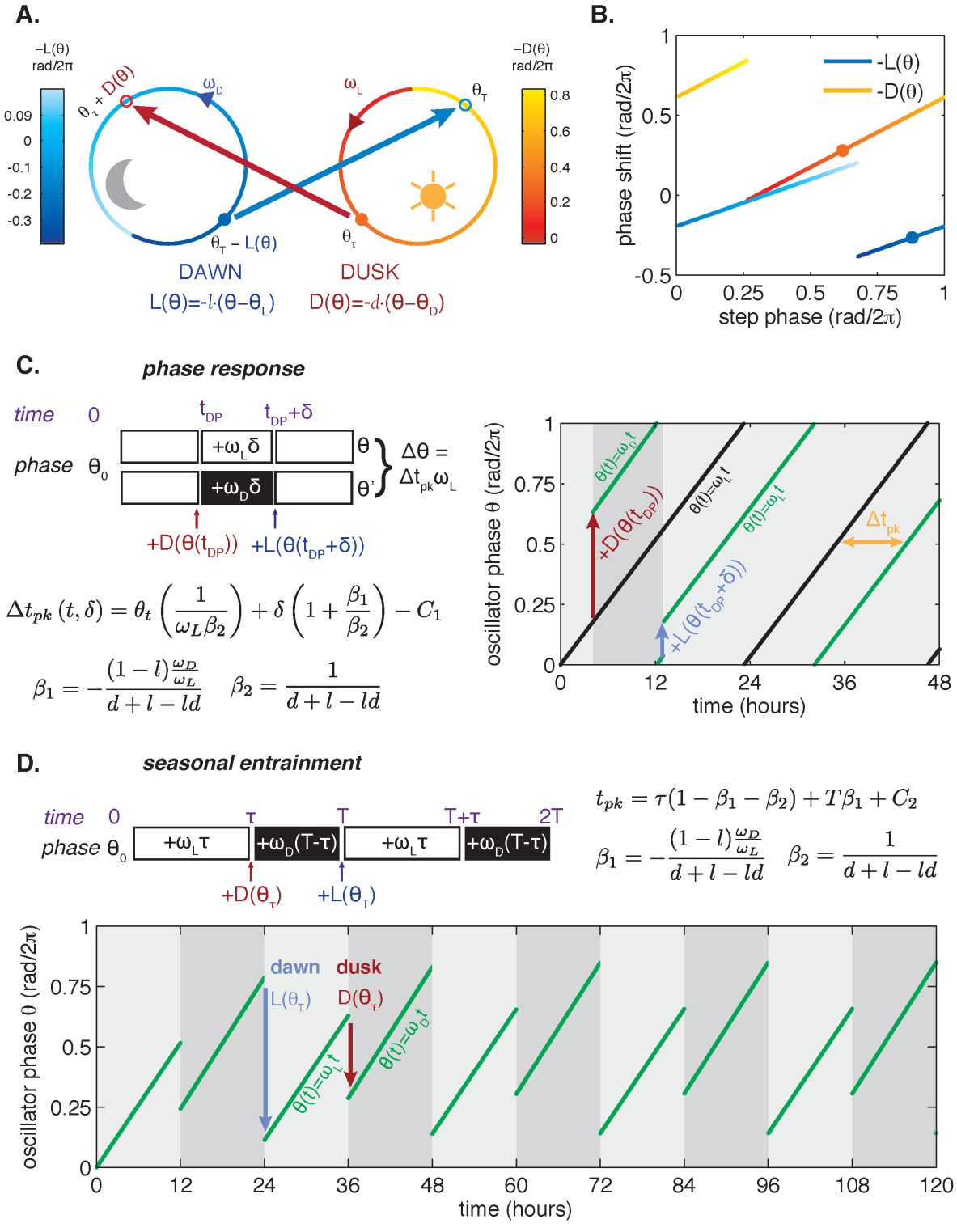

Figure S2.14. Phase oscillator with linear response framework.

(Figure S2.14 continued) (A) Schematic of the phase oscillator framework. In the light portion of the day, the oscillator runs along the "light" limit cycle (*orange*) and accumulates phase θ at constant rate ω_L; in the dark, the oscillator runs along the "dark" limit cycle (*blue*) with frequency ω_D. At dawn (*solid blue circle*) and dusk (*solid orange circle*), the oscillator transitions between the light and dark limit cycles (*blue and orange arrows*) and incurs instantaneous phase shifts given by $L(\theta)$ at dawn and $D(\theta)$ at dusk. In the linear approximation framework, $L(\theta)$ and $D(\theta)$ are linear functions of phase, such that $L(\theta) = -l(\theta - \theta_L)$ and $D(\theta) = -d(\theta - \theta_D)$. Colors along the "light" and "dark" limit cycles indicate the magnitude of phase shifts due to light-to-dark ($D(\theta)$) and dark-to-light ($L(\theta)$) responses throughout the cycle for a single set of linearized $L(\theta)$ and $D(\theta)$, shown in (B), generated by bootstrapping the measurements in Figure 2.3E-F. $\theta = 0$ refers to the minimum of KaiC phosphorylation rhythm.
(B) One set of linearized step response functions $\hat{L}_{lin}(\hat{\theta})$ and $\hat{D}_{lin}(\hat{\theta})$ for the KaiABC oscillator determined by SDS-PAGE analysis of KaiC phosphorylation rhythms (see Figure 2.3E-F). The functions plotted represent one pair of $\hat{L}_{lin}(\hat{\theta})$ and $\hat{D}_{lin}(\hat{\theta})$ generated by bootstrapping (see Computational Methods). Colors denote phase shift magnitude as in (A). Solid circular markers correspond to dawn and dusk transitions in (A).
(C) (*left*) Schematic of phase response analysis in the phase oscillator framework. The phase shift is a linear function of the dark pulse time (t_{DP}) and duration (δ) if $L(\theta)$ and the $D(\theta)$ are linear functions. Slopes of linear dependencies on t_{DP} and duration δ can be computed based on clock frequencies in light and dark (ω_L, ω_D) and slopes of $L(\theta)$ and $D(\theta)$ functions. (*right*) Simulation of a phase response experiment for a phase oscillator with experimentally determined parameters (ω_L, ω_D, l, and d from the same bootstrapped parameter set as in (B)). A 9-hour dark pulse applied 4 hours after the beginning of the simulation to an oscillator (*green*) results in a ≈8 hour phase delay relative to a control (*black*) that remains in light throughout the simulation.
(D) (*top*) Schematic of analysis of seasonal entrainment in the phase oscillator framework. Entrained phase is a linear function of day length (τ) and driving period (T) if $L(\theta)$ and the $D(\theta)$ are linear functions. Slopes of linear dependencies on τ and T can be computed based on four parameters (ω_L, ω_D, l, and d). (*bottom*) Simulation of entrainment to a LD 12:12 cycle for a phase oscillator with experimentally determined parameters (ω_L, ω_D, l, and d from the same bootstrapped parameter set as in (B)).

SPECIFIC ACKNOWLEDGEMENTS FOR CHAPTER 2

We thank Arvind Murugan and members of the Rust and Dinner labs, particularly H. Gudjonson and G. Pattanayak, for feedback and useful discussions. Joel Heisler and Andy LiWang assisted us with fluorescence polarization measurements. This work was supported by NIH Training Grant 5T32EB009412 (E.L.), NIH Training Grant T32GM07197 (U.L.), NIH R01 GM107369-01 (to M.J.R.), NSF PHY-1305542 (to A.R.D.), a Pew Biomedical Scholarship (to M.J.R.). E.L, J.L, H.Y., and U.L. carried out experiments. E.L. analyzed data. E.L., A.R.D. and M.J.R. designed the study, performed mathematical modeling, and wrote the paper.

EXPERIMENTAL MATERIALS AND METHODS

EXPERIMENTAL METHODS

Cyanobacterial strains and culture conditions. Two strains of *Synechococcus elongatus* PCC 7942 were used for this study. AMC1300 is a wild-type derivative carrying a bacterial luciferase bioluminescent reporter of *kaiBC* expression. AMC1300 carries *PkaiBC::luxAB* at NS1 and *PpsbAI::luxCDE* at NS2, which enables the cells to produce the luciferase enzyme and the long-chain aldehyde substrate for the luminescent reaction [45]. AMC408 carries a *purF* reporter (*PpurF::luxAB* at NS2*, PpsbAI:luxCDE* at NS1) [46]. Prior to experimental measurements, all cultures were grown in test tubes in BG11M liquid medium at 30 °C with shaking under cool white fluorescent bulbs (≈60 μmol photons m^{-2} s^{-1}, Philips AltoII).

Creating custom light-dark environments using LED arrays. To simulate different light-dark cycles, we used custom-built red LED arrays in a 96-well format (LEDs from

superbrightleds.com, cat. no. RL5-R12008; 96-well plates from Corning, cat. no. 3916). The LEDs were mounted into a hollowed-out 96-well plate and the tails of the LEDs were soldered into a circuit board, where they were wired in parallel in groups of four to the analog inputs of an Arduino Mega 2560 microcontroller. Another hollow 96-well plate was glued to the bottom of the LED-carrying plate, beneath the LEDs, in order to create a light baffle and prevent light leakage between the wells. These devices were placed ≈2 mm above a black 96-well plate containing cells growing on BG11-agar, such that every well of the growth plate received illumination from a single LED (≈1.8 cm between LED and agar surface). The growing plate was sealed with transparent film, with holes punctured above each well to provide aeration. Custom Arduino scripts were written to administer appropriate light-dark schedules to cells in the growth plates. Every well received the same light intensity (1.8 V across each LED, ≈200 μmol photons m^{-2} s^{-1}) in the light portion of the day. The temperature of the agar was 31.6 ± 0.8 °C underneath LEDs that were turned on and 28.9 ± 0.3 °C under LEDs that were off (mean ± standard deviation of 6-10 wells).

Monitoring gene expression in vivo using bioluminescent reporters. Cells were grown in test tubes until OD 0.5-0.8, as described above, and diluted to OD 0.2 immediately prior to experiment. A black 96-well plate was filled (200 μL/well) with BG11M-agar (15 g/L agar) supplemented with sodium thiosulfate (1 mM) and HEPES (20 mM, pH 8.0). When the BG11M-agar mixture cooled to room temperature, 35 μL of cells from growing culture at OD 0.2 were added to each well of the plate. The plate was sealed with transparent UniSeal (GE HealthCare Life Sciences cat no. 7704-0001), holes were punched above each well using 26G½ needle (BD Falcon, cat. no. 305111), and the plate was placed underneath an LED array. Bioluminescence

from luciferase reporters was measured every 30 minutes using a TopCount scintillation counter (PerkinElmer, IL). Each well of a 96-well plate was read for 1 second per measurement.

KaiABC in vitro reactions. KaiA, KaiB and KaiC were recombinantly expressed and purified as previously described [47], though the anion exchange chromatography purification step was omitted in the preparation of KaiC used for fluorescence polarization experiments. Protein concentration was measured via Bradford Assay Kit (Promega). For experiments relying on SDS-PAGE analysis of KaiC phosphorylation, KaiABC proteins were mixed in master reaction buffer (20 mM Tris [pH 8], 150 mM NaCl, 5 mM $MgCl_2$, 10% glycerol, 0.5 mM EDTA) supplemented with a mixture of ATP and ADP (day buffer: 2 mM ATP, night buffer: 2 mM ATP, 7.5 mM ADP). All reactions were incubated at 31 °C. To mimic light-to-dark transitions, ADP stock (400 mM, pH 7.5) was added to appropriate reactions to 7.5 mM final [ADP]. To mimic dark-to-light transitions, the reactions were passed through Zeba desalting columns (7 MW kDa cutoff, ThermoFisher) equilibrated in day buffer. Because every buffer exchange step dilutes the proteins by about 10%, the reactions were performed at 3× protein concentration (10.5 μM KaiB and KaiC, 4.5 μM KaiA). At every measured time point, 2 μL of reaction mixture was removed from the reaction mixture and mixed with 4 μL of 1.5× SDS-PAGE sample buffer. KaiC phosphorylation was assayed by SDS-PAGE and quantified by densitometry, as previously described [17].

In the cases where oscillations were read out by monitoring fluorescence polarization, KaiABC proteins were mixed at 3× standard protein concentration in the master reaction buffer supplemented with a mixture of ATP and ADP (day buffer: 2.5 mM ATP, night buffer: 2.5 mM ATP, 7.5 mM ADP). All reactions were incubated at 31 °C. Day-to-night transitions were

mimicked by addition of 7.5 mM ADP (final), and night-to-day transitions were mimicked by passing the reactions through Zeba desalting columns twice.

For step-up perturbations shown in blue in Figure 2.3D, buffer exchange steps were administered every 2 hours over a 24-hour interval, and phase shifts were measured relative to an unperturbed control reaction. For every other experiment in Figure 2.3C-D, buffer exchange or ADP addition steps were performed every 2 hours over a 12-hour interval on two out-of-phase reactions, prepared as follows. A master mix containing proteins and appropriate nucleotides was split into two tubes, which were flash-frozen in liquid nitrogen immediately after mixing and stored at −80 °C. To prepare out-of-phase reactions, one of the two tubes was thawed in a 30 °C water bath 12 hours later than the other.

After all buffer exchanges were completed, the reactions were supplemented with fluorescently labeled KaiB (0.2 μM final) and transferred to the plate reader.

Preparation and labeling of fluorescently tagged KaiB. We introduced a K25C mutation in KaiB using site-directed mutagenesis of the pMR0019 plasmid carrying 6xHis-PSP-KaiB^{WT} construct in the pET47b(+) backbone. KaiB^{K25C} was expressed in BL-21 (DE3) *E. coli* by overnight induction with IPTG at 18 °C and purified following the standard protocol [47]. Labeling with 6-iodoacetofluorescein (6-IAF) was performed as previously described [19] with minor modifications. Briefly, 130 μL of KaiB^{K25C} stock (50-100 μM) was buffer-exchanged into labeling buffer (20mM Tris, 1 mM TCEP, pH 7.0 – 7.5) using a Zeba desalting column (7 MW kDa cutoff). A freshly prepared solution of 6-IAF in DMSO was added to the protein solution in 10-fold molar excess, and the mixture was incubated overnight at 4 °C in the dark. The labeling reaction was quenched by addition of DTT in approximately 10-fold molar excess relative to 6-

IAF. Unincorporated dye was removed through three rounds of 5-fold dilution in reaction buffer and subsequent concentration using a centrifugal filter (10 kDa cutoff, Amicon, Millipore). Concentration of final fluorescein-labeled KaiB^{K25C} solution was determined by Bradford assay.

Monitoring fluorescence polarization rhythms using labeled KaiB. Oscillations in KaiABC reaction mixtures supplemented with fluorescently labeled KaiB^{K25C} (10.5 μM KaiB and KaiC, 4.5 μM KaiA, 0.2 μM KaiB-fluorescein) were monitored on an Infinite F500 plate reader equipped with a fluorescence polarization module (Tecan Trading AG, Switzerland). At least 30 minutes prior to measurement, the built-in heating module was turned on to warm the instrument and a black 384 well-plate (Greiner, cat. no. 781900) was loaded into the plate reader. For the metabolic entrainment experiment shown in blue in Figure S2.4A and the step-up experiment shown in blue in Figure 2.3D, the plate reader temperature was 28 °C; for all other experiments, the plate reader temperature was 31 °C. Reactions were quickly transferred onto the pre-warmed plate (20-35 μL/well) and 1-3 wells were filled with master reaction buffer. The plate was sealed with a polyethylene silicone plate sealer (Nunc™, ThermoFisher cat. no. 235307) and returned to the instrument. Fluorescence polarization of wells of interest (exc. 485 nm, 20 nm bandpass; emm. 535 nm, 25 nm bandpass; dichroic 510 nm.) was read out every 15 minutes using a script created in iControl software (v. 1.12, Tecan Trading AG). Wells containing reaction buffer only were used as blanks, and the G factor was calibrated such that a solution of free fluorescein in reaction buffer produced a reading of ≈20 mP.

Data analysis. All oscillating trajectories were fit to sinusoids using optimization routines written in MATLAB (Mathworks, Inc.) (RRID: SCR_001622). See Computational Methods for detailed fitting procedures and descriptions of simulations. Computational pipelines used for

analysis and simulations have been deposited to GitHub at https://github.com/euleip/Simulations_and_analysis_pipelines_github_repo [48].

COMPUTATIONAL METHODS

Optimization and curve-fitting routines

All nonlinear fitting procedures were written in MATLAB using the lsqnonlin() or nlinfit() routines. Linear regressions were performed using the polyfit() function. Uncertainties around the best-fit slopes were evaluated using standard formulas for linear regression with known errors in dependent variables [49]. For *in vivo* experiments, these errors were computed as standard errors of the mean from replicate measurements; for *in vitro* measurements in Figure 2.2, the errors in fit phases were computed from the curvature of the cost function at the optimum using the nlpredci() function in MATLAB. Where indicated, 95% confidence intervals were also estimated by nlpredci().

Normalization of bioluminescent reporter traces recorded in light-dark cycles or in continuous light

Prior to fitting, bioluminescence trajectories were normalized to zero mean and unit standard deviation over the fitting interval, unless specified otherwise. In all analyses, we discarded data from the first 2.5 hours after lights-on to avoid masking effects.

Estimation of clock phase *in vivo* in light-dark cycles

The bacterial luciferase reporter system that we use exhibits transient masking effects following dark-to-light transitions. To overcome this issue in determining the phase of gene expression in light-dark cycles of varied day length, we employed a drive-and-release strategy. In this approach (illustrated for LD 8:16, LD 12:12 and LD 16:8 in Figure 2.1A), cells were first entrained to a given diurnal schedule and then released into constant light for several days to determine the peak times of the entrained rhythm.

We relied on two approaches to calculate the peak times of normalized bioluminescence trajectories recorded after release into constant light: (i) we fit sinusoids to 48-hour segments of the trajectories in constant light, and (ii) we locally fit parabolas near the maxima of the trajectories. The advantage of sinusoidal fitting is that it captures phase information for the entire waveform; on the other hand, local parabolic fitting allows for a precise determination of the time of an individual peak without influence from others. In practice, we found that the estimates of the scaling between entrained phase and day length derived from the two approaches are in good agreement with each other (Table 2.1. Summary of biologically independent ***in vivo*** experiments measuring entrainment to 24-hour light-dark cycles of varying day length., Figure S2.2). Fitting details are described in the following two subsections.

Error bars in Figure 2.1C, Figure S2.2A, and Figure 2.5 represent the standard deviation of peak times calculated from technical replicates (n=4-8). Technical replicates refer to measurements obtained from side-by-side cultures subjected to the same light-dark conditions. In rare cases, cells in individual wells died or produced noisy bioluminescent signals or trajectories

that fit poorly to sinusoids or parabolas. We rejected trajectories as outliers from our analysis if they produced fits with a squared error greater than 10 (0-13 outliers per 96 wells).

(i) Estimation of period and peak times from sinusoidal regression

Sinusoidal fits were performed by least-squares minimization of the cost function:

$$cost = \sum_{i=1}^{N} \left[y_i - \left(A \sin\left(\frac{2\pi x_i}{T} - \phi \right) + m x_i + C \right) \right]^2 ,$$

where y_i and x_i represent, respectively, the normalized bioluminescence signal and the time after release into constant light for the i-th timepoint. The period in the fits was constrained to $23 < T < 25$ hours. The best-fit period was distributed within these bounds, independent of the day length of the preceding entraining cycle (Figure S2.2D), a conclusion we confirmed in a peak-to-peak analysis described below.

We considered whether the quality of sinusoidal fits affected the estimated slope m. When we performed sinusoidal fits of the dataset in Figure 2.1C, the least-squares errors, normalized by degrees of freedom, were distributed between 0 and 1. If data from all of the wells were included in the analysis, linear regression to this data yielded a slope of $m = 0.55 \pm 0.02$ (Figure 2.2). As the table below shows, imposing stricter cutoffs on least-square fitting error did not significantly impact the estimate of the slope, so an estimate of m based on all of the data is reported in Figure 2.2.

Table S2.1. Quality of sinusoidal fits and corresponding values of *m*.

least-squares error threshold	% wells satisfying	m ± SD of estimate
1	100%	0.55 ± 0.02
0.5	90%	0.53 ± 0.01
0.1	45%	0.51 ± 0.03
0.05	17%	0.64 ± 0.03

(ii) Estimation of period and peak times from local parabolic regression

We found that certain bioluminescent trajectories were fit poorly by sinusoids. As Figure S2.3 shows, *purF* reporter waveforms display (a) strong asymmetry, marked by faster rising and slower falling dynamics (e.g., second peak in τ = 18 hours curve), (b) wide peaks (e.g., first peak in τ = 8 hours curve), and (c) broad "shoulders" after the peak that occasionally give rise to secondary peaks (e.g., first peak in τ = 18 hours curve). In some cases *kaiBC* reporter trajectories also exhibited successive peaks with significantly different amplitudes. In Figure 2.1C and Figure S2.3, we fit parabolas to 6-hour intervals around the peaks of normalized bioluminescence trajectories and estimated phases from the first peak positions and periods from the average peak-to-peak times (n=4-8). We verified that this peak-fitting procedure produced comparable results to sinusoidal fitting for the *kaiBC* datasets in Figure 2.1C and Figure S2.2 (see Figure 2.2 and Figure S2.2B-E).

Comparison of waveforms during light-dark cycling and in continuous light

To compare clock reporter dynamics during entrainment and in continuous light in Figure S2.1, we computed nonparametric correlations (Kendall's τ coefficient) between the reporter signal (P_{kaiBC}*::luxAB*) measured during the "day" windows in light-dark cycles (days 1-5) and during the corresponding time interval after release into continuous light (day 6). For example, in the case of LD 10:14, the normalized luminescence data recorded between 2.5 and 14 hours during each of the five entraining cycles were correlated with the luminescence dynamics measured between 2.5 and 14 hours after release into constant light. The fact that we observe Kendall's $\tau > 0.8$ after the second driving cycle suggests that cells are effectively entrained

within three cycles and that rhythms observed during the lights-on portion of a light-dark cycle can be thought of as a fragment of a free-running rhythm.

Estimation of clock phase *in vitro* in metabolic cycles

For the %P-KaiC measurements in Figure 2.2C, normalized KaiC phosphorylation time courses from day 3 of each reaction were fit independently to sinusoids. Best-fit parameters were obtained by minimizing the cost function:

$$cost = \sum_{i=1}^{N} \left[y_i - \left(A \sin\left(\frac{2\pi x_i}{T} - \phi \right) + C \right) \right]^2 ,$$

with the period T fixed at 24 hours to match the period of the imposed metabolic cycles.

For the fluorescence polarization experiments in Figure 2.2C, fluorescence polarization dynamics were recorded for 48 hours after the last buffer exchange, normalized (to zero mean, unit variance) and fit to sinusoids according to the expression above, with fits to all reactions from the same experiment sharing a globally-fit period T.

Fitting and error propagation analysis of step-response experiments

Step-response experiments described in this section were performed a total of three times: once using KaiC phosphorylation to read out clock phase and twice using the fluorescence polarization reporter of KaiB-KaiC interaction. The phosphorylation measurements were made using an independent preparation of proteins from the fluorescence polarization experiments.

We performed step-response experiments in Figure 2.3 in order to determine whether the behavior of the clock in metabolic cycles could be decomposed into a sum of phase shifts due to individual clock transitions. To do so, we first needed (a) to extract L and D functions from step

response measurements, and then (b) to use these L and D functions in numerical simulations of clock entrainment to light-dark cycles, as described in the main text and Mathematical Appendix.

In our experiments, we directly observed how the dynamics of the fluorescence polarization reporter or KaiC phosphorylation changed as a function of lab time (e.g., Figure 2.3A-B), but for our downstream simulations and analysis (e.g., Figure 2.4) these values had to be converted to clock phase coordinates (e.g., Figure 2.3C-D) consistent with how $L(\theta)$ and $D(\theta)$ are defined. Specifically, we needed to (i) convert the lab time of each step to corresponding clock phase θ (or clock time, CT), and then (ii) determine the phase of each fluorescence polarization trace or KaiC phosphorylation trajectory after the perturbation in order to compute the phase shift ($L(\theta)$ and $D(\theta)$) relative to an unperturbed control.

Though these conversions are straightforward in principle, it is important to note that both (i) and (ii) rely on sinusoidal regression of phase from measured data, and that the best-fit phases in both cases are only estimates of the true values. The corresponding uncertainty in the best-fit parameters must be propagated through numerical simulations of entrainment.

Because the temporal resolutions of the KaiC phosphorylation and fluorescence polarization measurements are very different (3 hours vs. 15 minutes, respectively), we expected the sources of uncertainty in fitting these data to be different (see Figure S2.4), and we thus analyzed their errors in different ways. The sparse measurement of KaiC phosphorylation dynamics leads to relatively high uncertainty in best-fit phase and period, and we propagated the errors through our simulations using nonparametric bootstrapping of the datasets. In the case of the fluorescence polarization measurements, experiment-to-experiment variability is the major source of uncertainty. We therefore performed two replicate measurements of L and D (Figure

2.3C-D) and used the four possible combinations of *L* and *D* in entrainment simulations to assess the range of entrainment behavior constrained by our measurements of these step-response measurements. We describe each of these approaches in turn in the following two sections.

Error propagation analysis of step-response experiments performed using the fluorescence polarization reporter of KaiB-KaiC interaction

Periods and phases of reactions in each set were determined by global sinusoidal fitting: amplitude, offset and phase terms were fit independently for each reaction, but a single best-fit period was shared among all fits in a given step-up or step-down set. To avoid transient effects due to a metabolic pulse, only those data points which were collected at least 16 hours after a step-up or step-down perturbation were used for fitting. Mathematically, we used a non-linear least-squares optimization routine to minimize the cost functions:

$$cost_{day} = \sum_{r=1}^{N_{rxns}} \sum_{i=1}^{N_r} \left[y_{r,i} - \left(A_r sin\left(\frac{2\pi t_{r,i}}{T_{day}} - \phi_r \right) + C_r \right) \right]^2 \text{ (for reactions in day buffer)}$$

and

$$cost_{night} = \sum_{r=1}^{N_{rxns}} \sum_{i=1}^{N_r} \left[y_{r,i} - \left(A_r sin\left(\frac{2\pi t_{r,i}}{T_{night}} - \phi_r \right) + C_r \right) \right]^2 \text{ (for reactions in night buffer),}$$

where $y_{r,i}$ refers to the *i*-th data point in the *r*-th normalized fluorescence polarization trajectory, $t_{r,i}$ refers to the lab time when that data point was collected, and N_r is the number of data points fit in the *r*-th reaction. Here A_r, φ_r and C_r are the best-fit parameters for the *r*-th reaction; T_{day} and T_{night} are best-fit periods for all reactions in the 100% ATP and 25% ATP datasets, respectively.

These best-fit parameters were used to determine the phase θ of each step perturbation and corresponding phase shifts L(θ) and D(θ), analogously to the way described for the KaiC phosphorylation datasets below. The step-response functions were interpolated linearly to generate smooth curves while enforcing 2π-periodicity.

Linearized step-response functions $L_{lin}(\theta)$ and $D_{lin}(\theta)$ were prepared by linear regression of $L(\theta)$ and $D(\theta)$ centered on the regions used during metabolic entrainment: D functions were linearized between 6 and 22 CT hours; L functions were linearized between 18 and 34 CT hours (see Figure 2.3C-D). To satisfy periodicity, the step-response functions were assembled as piecewise-linear functions with the same slope everywhere but with offsets every 2π radians at "breakpoints," which were selected by manual inspection. See Figure S2.8C for an illustration of $L(\theta)$ and $D(\theta)$ and the corresponding $L_{lin}(\theta)$ and $D_{lin}(\theta)$.

Finally, step phases deduced from polarization trajectories were adjusted to match the phases of the KaiC phosphorylation rhythm. This conversion made use of measurements in Figure S2.4, which indicated that the phase of oscillation in KaiC phosphorylation lags behind the phase of the polarization reporter of KaiB-KaiC binding by approximately $2\pi/3$.

By performing this analysis for the two step-up and two step-down datasets in Figure 2.3C-D, we generated two sets of $\{L, L_{lin}, T_{day}, T_{night}\}$ and two sets of $\{D, D_{lin}, T_{day}, T_{night}\}$. The phase oscillator simulations described below require using the L and D functions together in each simulation. To propagate the experiment-to-experiment variability in step-response measurements through our simulations, we combined the two measurements of L and two measurements of D into the four possible combinations of $\{L, D\}$ pairs. This resulted in four sets of $\{L, L_{lin}, D, D_{lin}, T_{day}, T_{night}\}$, which were used in the simulations below.

The ratio of oscillator frequencies in dark and light, $\frac{\omega_D}{\omega_L} = \frac{T_{day}}{T_{night}} = 0.94 \pm 0.01$, was determined by averaging the values of T_{day} and T_{night} from the two step-up and two step-down sets above. Best estimates for the slopes l and d in Figure S2.9 were computed via the following bootstrap analysis. For each L and D function in Figure 2.3C-D, we selected points from the regions used for linearization above (6-22 CT hours on D, 18-34 CT hours on L). We sampled these data points with replacement until we generated 500 samples containing at least 3 unique points. For each set of resampled points, we computed the slope of the best-fit line, for a total of 1000 samples of l and d. The crosshair in Figure S2.9 marks the average ± standard deviation of these values ($l = 0.34 \pm 0.03$, $d = 0.38 \pm 0.05$).

The phase oscillator model discussed in the main text and the Mathematical Appendix makes the prediction that the proportionality constant m between entrained phase and day length depends on l and d coefficients according to $m(l,d) = 1 - \frac{-(1-l)\times(\omega_D/\omega_L)}{d+l-ld} - \frac{1}{d+l-ld}$. To check whether this prediction is in line with our experimental measurement of m, we used this formula to calculate m for every pair of l and d samples generated in the bootstrapping procedure above, assuming $\frac{\omega_D}{\omega_L} = 0.94$. According to this calculation, $m(l,d) = 0.34 \pm 0.04$ (mean ± standard deviation of the distribution), which is in agreement with the experimental measurement in Figure 2.2C ($m = 0.38 \pm 0.07$).

Non-parametric bootstrapping of step-response datasets collected using SDS-PAGE analysis of KaiC phosphorylation

Recall that measuring each step-response function requires (i) conversion of the lab time of each step to corresponding clock phase θ (or clock time, CT), and then (ii) determination of

the phase of each KaiC phosphorylation trajectory after the perturbation in order to compute the phase shift ($L(\theta)$ and $D(\theta)$) relative to an unperturbed control. In particular, uncertainties in (i) manifest as x errors on L and D in Figure 2.3E-F; these errors are correlated across all points on the step-response function. Uncertainties in (ii) manifest as y errors on L and D; these errors derive from the errors in the phase estimates of both the control and step reactions. To propagate both of these sources of error, we used the following non-parametric bootstrapping strategy.

First, KaiC phosphorylation dynamics from all step-response measurements were assembled into a master dataset containing 9 step-up trajectories, 9 step-down trajectories, as well as two control reactions. These measurements were performed once on an independent preparation of proteins from the batch used to generate data in Figure 2.3C-D. This master dataset was then trimmed to include only data collected at least 16 hours after a step transition, and every trajectory was normalized. To generate bootstrapped datasets, we sampled with replacement from the entire master dataset (as opposed to resampling reactions individually) 1000 times.

Next, we used each resampled dataset to compute phase shifts in KaiC phosphorylation due to step-up and step-down transitions; in other words, each bootstrapped dataset was used to derive a bootstrapped pair of $L(\theta)$ and $D(\theta)$. For a given dataset, we globally fit all 100% ATP trajectories (9 step-up trajectories, plus the 100% ATP control reaction) such that all fits shared a best-fit period (T_{day}), but phase, amplitude and offset terms were fit independently for each reaction, as described above for polarization datasets. Likewise, we fit all 20% ATP trajectories (9 step-down reactions, plus the 20% ATP control reaction) to obtain a globally best-fit period (T_{night}) and independently fit phases for every reaction.

L(θ) and *D(θ)* map the phase at which a metabolic step occurs to the resulting phase shift. The phase at which the metabolic step occurred for every reaction *r* was computed from the best-fit phase of the appropriate control reaction at step time $t_{r,step}$:

$$\theta_{r,step}^{control} = \frac{2\pi t_{r,step}}{T_{con}} - \phi_{con},$$

where ϕ_{con} is the best-fit phase of the control reaction and T_{con} is the globally-fit oscillator period in the appropriate control condition (i.e., $T_{con} = T_{day}$ for step-down reactions, $T_{con} = T_{night}$ for step-up reactions).

Similarly, we computed the apparent phase of each perturbed reaction at the time of each step:

$$\theta_{r,step} = \frac{2\pi t_{r,step}}{T_{pert}} - \phi_{r},$$

where ϕ_r is the best-fit phase of the *r*-th reaction and T_{pert} is the globally-fit oscillator period in the perturbed condition ($T_{pert} = T_{night}$ for step-down reactions, $T_{pert} = T_{day}$ for step-up reactions).

Finally, we defined the phase shift in response to each step perturbation as the difference in phase of the perturbed reaction and the appropriate unperturbed control.

$$L\left(\theta_{r,stepUp}^{control}\right) = \theta_{r,stepUp} - \theta_{r,stepUp}^{control}.$$

$$D\left(\theta_{r,stepDown}^{control}\right) = \theta_{r,stepDown} - \theta_{r,stepDown}^{control}.$$

To estimate phase shifts at other values of *θ,* we linearly interpolated *L* and *D* between the measured values while enforcing 2π-periodicity.

For each set of *L* and *D* generated in this way, we also prepared linearized versions L_{lin} and D_{lin}. Linear fits to *L* and *D* were performed over the range of step times similar to the ones

we selected for fluorescence polarization-based step-response functions as discussed above (L between 18 and 33 CT hours, D between 6 and 23 CT hours). These regions of L and D were selected by visual inspection because they are centered on phases used by the KaiABC oscillator in diurnal cycles (i.e., see arrows in Figure 2.3E-F) but also contain enough points (5-7) to avoid biasing the slope estimate by a single poorly fit data point.

We extrapolated the linear approximations to L and D over the entire cycle, with a single breakpoint away from the linear region to satisfy 2π-periodicity. Breakpoints were selected by visual inspection. While interpolating between data points near the breakpoint, we assumed that L and D (or L_{lin} and D_{lin}) never generate phase shifts larger than one cycle (i.e., winding number of 0). We anticipate that this choice does not significantly affect entrained phase in most of our simulations because the regions of L and D near the breakpoint are rarely used by the oscillator during entrainment when $\tau < 14$ hours.

We repeated this procedure for each of the 1000 bootstrapped datasets, thereby generating 1000 sets of $\{L, D, L_{lin}$ and $D_{lin}, T_{day}, T_{night}\}$ that were used for subsequent analysis. Figure 2.3E-F shows the mean ± standard deviation of the distribution of bootstrapped L and D generated this way.

Simulations of a phase oscillator driven by a light-dark cycle

We simulated entrainment to a step-like driving cycle for a phase oscillator governed by the four combinations of $\{L, L_{lin}, D, D_{lin}, T_{day}, T_{night}\}$ determined from the fluorescence polarization assays and the 1000 bootstrapped sets of $\{L, D, L_{lin}$ and $D_{lin}, T_{day}, T_{night}\}$ derived from KaiC phosphorylation measurements. Electing to work in units of cycles (1 cycle = 2π rad),

we defined a phase variable $\hat{\theta} = \frac{\theta - \pi/2}{2\pi}$, such that $\hat{\theta} = 0$ cycles and $\hat{\theta} = 1$ cycles correspond to the trough of the KaiC phosphorylation trajectory and $\hat{\theta} = 0.5$ cycles corresponds to the peak. Where circadian time (CT) is mentioned in the text, we have adopted the convention that CT = 0 and 24 hours refer to $\hat{\theta} = 0$ and 1 cycles, respectively; CT = 12 hours refers to $\hat{\theta} = 0.5$ cycles. We also defined corresponding analogs of *L* and *D* in units of cycles:

$$\hat{\theta} = \frac{\theta - \pi/2}{2\pi}$$
$$\hat{L}(\hat{\theta}) = \frac{L(\theta)}{2\pi}$$
$$\hat{D}(\hat{\theta}) = \frac{D(\theta)}{2\pi}$$

See Figure S2.8C for examples of $\hat{L}, \hat{D}, \hat{L}_{lin}$ and $\hat{D}_{lin}$. For each set of $\{\hat{L}, \hat{D}, \hat{L}_{lin}, \hat{D}_{lin}, T_{day}, T_{night}\}$ generated in this way, we modeled oscillator entrainment to a driving cycle. As shown schematically in Figure 2.4A and the Mathematical Appendix, oscillator phase increases with constant angular velocity (given by $\omega_L = \frac{1}{T_{day}}$ during the day and $\omega_D = \frac{1}{T_{night}}$ during the night); at dawn and dusk, oscillator phase shifts instantaneously according to $\hat{L}$ and $\hat{D}$, respectively. Therefore, oscillator phases at dusk and dawn of the *n*-th entraining cycle can be computed iteratively:

$$\hat{\theta}_n^{dawn} = \hat{\theta}_{n-1}^{dusk} + \hat{D}\left(\mathrm{mod}(\hat{\theta}_{n-1}^{dusk}, 1)\right) + \frac{T - \tau}{T_{night}}$$

$$\hat{\theta}_n^{dusk} = \hat{\theta}_n^{dawn} + \hat{L}\left(\mathrm{mod}(\hat{\theta}_n^{dawn}, 1)\right) + \frac{\tau}{T_{day}}$$

We simulated oscillator behavior in 24-hour light-dark cycles (T_{dr} = 24) with day length τ lasting from 4 to 18 hours. In simulations relying on $\hat{L}$ and $\hat{D}$ determined from KaiC

phosphorylation measurements, we set the initial condition $\hat{\theta}_0$ for a given value of τ based on our measurements of entrained phase of the KaiABC oscillator in corresponding metabolic cycles (i.e., based on values interpolated between black markers in Figure 2.2C). Simulations using step-response functions based on fluorescence polarization measurements were started from $\hat{\theta}_0 = 0$. We simulated 10 light-dark cycles and recorded oscillator phase after each dawn (immediately after $\hat{L}(\hat{\theta}_t)$ phase shift).

For each set of $\hat{L}$ and $\hat{D}$, we performed simulations for τ = 4-18 hours for both the phosphorylation-based step functions and fluorescence polarization-based step functions. Figure S2.7 illustrates simulations governed by one such set of $\hat{L}$ and $\hat{D}$ (derived from magenta and blue step-response measurements shown in Figure 2.3C-D). We also carried out entrainment simulations for the linearized step-response functions described above. For each value of τ, mean entrained phase at dawn and its standard deviation are plotted as shaded areas in Figure S2.8A. Figure S2.8B illustrates one example of the driven behavior of a phase oscillator driven by the linearized versions of $\hat{L}$ and $\hat{D}$ shown in Figure 2.3E-F.

We judged that the oscillator entrained stably to a given diurnal cycle if the standard deviation of clock phases at dawns of the last five driving cycles was less than 0.01 cycles. For each value of τ, we selected those simulations where the oscillator entrained stably to the light-dark cycle, and computed the mean phase at dawn and its standard deviation (σ) for that set of simulations. These values are represented in shaded areas in Figure 2.4C (for fluorescence polarization data) and Figure S2.8C (for KaiC phosphorylation data).

We were also interested in how quickly the oscillator approached entrainment in simulations for $6 \leq \tau \leq 18$, the range we profiled experimentally in Figure 2.2. To make this

determination for a given value of τ, we computed how much oscillator phase at dawn varied over 3 successive cycles in a sliding window:

$$EC_n = \sqrt{var\left(\hat{\theta}_{n\times T_{dr}}, \hat{\theta}_{(n+1)\times T_{dr}}, \hat{\theta}_{(n+2)\times T_{dr}}\right)} \text{ for } n = 1\text{-}8$$

We used the first value of n for which $EC_n < 0.01$ as a proxy for the speed of approach to entrainment.

The tables below display summary statistics for the entrainment simulations.

Table S2.2. Simulations based on step-response functions measured via fluorescence polarization reporter.

step fun. type	τ's profiled	no. sim.	% entrained sim. 4 < τ < 18	8 < τ < 16	% entrained within 3 cycles (8 < τ < 16) all sim.	all sim entr. within 8 cyc.
$\hat{L}$ and $\hat{D}$	4, 4.01, …, 18 hours	564	100%	100%	83%	83%
$\hat{L}_{lin}$ and $\hat{D}_{lin}$	4, 4.01, …, 18 hours	564	100%	100%	100%	100%

Table S2.3. Simulations based on step-response functions measured via SDS-PAGE analysis of KaiC phosphorylation.

step fun. type	τ's profiled	no. sim.	% entrained sim. 4 < τ < 18	8 < τ < 16	% entrained within 3 cycles (8 < τ < 16) all sim.	all sim entr. within 8 cyc.
$\hat{L}$ and $\hat{D}$	4, 4.25, …, 18 hours	57 000	76%	87%	86%	97%
$\hat{L}_{lin}$ and $\hat{D}_{lin}$	4, 4.25, …, 18 hours	57 000	98%	100%	99%	100%

In the large majority of our simulations, we found that the phase oscillator entrained stably within 3 light-dark cycles. For simulations derived from KaiC phosphorylation datasets, we found that the oscillator either entrained to the driving cycle quickly or not at all. Indeed,

when we restricted our analysis only to those simulations that were judged as entrained within 8 cycles, over 96% entrained within 3 light-dark cycles. Generally, the oscillator entrained readily for day lengths shorter than 14 hours, but often failed to entrain for longer day lengths. We determined that this occurs because for $\tau > 14$ dawn phases often sample the $\hat{L}$ function near the breakpoint of the curve (near 18 CT hours in Figure 2.3F), leading to erratic responses to driving cues (i.e., lack of entrainment) or disagreement between simulations and experiment (Figure S2.8B). Relatedly, we believe that the better agreement with experiment achieved in simulations using the step functions derived from the fluorescence polarization data than from the KaiC phosphorylation data reflects the better temporal resolution of the breakpoint (4 hours using polarization approach vs. 8 hours for KaiC phosphorylation).

In simulations of entrainment to light-dark cycles of varying period in Figure S2.6, we relied on a single set of $\{L, D, L_{lin}$ and $D_{lin}, T_{day}, T_{night}\}$ based on step-response measurements shown in blue and magenta in Figure 2.3C-D. We simulated entrainment to driving periods from 6-48 hours, in increments of 0.0025 hours. For each driving period T_{drive}, we subjected the phase oscillator to 1000 cycles with equal day and night durations ($\tau = T_{drive}/2$) and plotted the phases attained by the oscillator at the end of night-time (immediately preceding the action of L) at the last 950 cycles.

Simulations of phase resetting

We used $\hat{L}_{lin}$ and $\hat{D}_{lin}$ derived from the same step-response measurements as in Figure S2.7 to simulate response of a phase oscillator to 12-hour dark pulses administered throughout

the circadian cycle (Figure S2.10, Figure S2.14D). Phase evolution of the oscillator was simulated explicitly for 120 hours using a timestep of dt = 0.01 hours:

$$\hat{\theta}_{t+dt} = \begin{cases} \hat{\theta}_t + \dfrac{dt}{T_{day}} & \text{(in light)} \\ \hat{\theta}_t + \dfrac{dt}{T_{night}} & \text{(in dark)} \\ \hat{\theta}_t + \hat{L}\big(\mathrm{mod}(\hat{\theta}_t, 1)\big) & \text{(at dawn)} \\ \hat{\theta}_t + \hat{D}\big(\mathrm{mod}(\hat{\theta}_t, 1)\big) & \text{(at dusk)} \end{cases}$$

Estimation of phase shifts in response to dark pulses *in vivo*

For phase resetting and wedge experiments (Figure 2.5), clock phase was estimated by sinusoidal regression of normalized bioluminescence data collected 36-48 hours after the end of the applied dark pulse. Phase shifts in response to dark pulses were computed as differences in average peak times between perturbed wells ($t_{pk,DP}$) and controls ($t_{pk,LL}$): $\Delta t_{pk} = \bar{t}_{pk,DP} - \bar{t}_{pk,LL}$, where overbars indicate averages over replicate wells (n=4-8). Clock phases at which the dark pulses were applied were determined from the average fit phase and period of the unperturbed (control) wells ($\bar{\phi}_{LL}$ and $\bar{T}_{LL}$) according to $\theta_t = \frac{t}{\bar{T}_{LL}} - \frac{\bar{\phi}_{LL}+0.5\pi}{2\pi}$, where θ_t is measured in cycles and $\theta = 0$ corresponds to the minimum of an oscillatory trajectory.

Global fit to phase response and seasonal entrainment datasets

In the Mathematical Appendix, we show that in the regime where the circadian clock is well-approximated by a phase oscillator governed by linear L and D step-response functions, the slopes of seasonal entrainment and phase resetting of the clock can be described by a model with two free parameters β_1 and β_2: for phase resetting, $\Delta t_{pk} = \theta_t \left(\frac{1}{\omega_L \beta_2}\right) + \delta\left(1 + \frac{\beta_1}{\beta_2}\right) + C_1$ and for

entrainment $t_{pk} = \tau(1 - \beta_1 - \beta_2) + T\beta_1 + C_2$. Here δ is dark pulse duration (in hours), τ is day length (in hours), θ_t is the clock phase at time t (in cycles), ω_L is the clock frequency in the light (in units of cycles/hour), T is the driving period (in hours), and C_1 and C_2 are constants that do not depend on θ_t, δ, τ, or T. For phase resetting experiments, θ_t and ω_L were estimated based on the average of the best sinusoidal fits to unperturbed wells in each experiment ($\bar{\phi}_{LL}$ and $\bar{T}_{LL}$). In particular, we set $\theta_t = \omega_L t - \frac{\bar{\phi}_{LL}+0.5\pi}{2\pi}$. In the formula for Δt_{pk}, the term $\theta_t \left(\frac{1}{\omega_L \beta_2}\right)$ thus simplifies to $\frac{t}{\beta_2} - (\frac{\bar{\phi}_{LL}+0.5\pi}{2\pi\beta_2})$, and the term to the right of the minus sign was incorporated into the constant term C_1.

In the global fits of all datasets in Figure 2.5A-C, we varied β_1 and β_2 to simultaneously fit Δt_{pk} to our phase-resetting and wedge data and t_{pk} to our seasonal entrainment data. The constant terms were allowed to vary as follows:

- in Figure 2.5C, a single C_2 term was fit for all curves, referred to as $C_{entrainment}$ below;
- in Figure 2.5B, a single C_1 intercept was fit for both datasets (t_{DP} = 36 and t_{DP} = 39 hours), referred to as C_{wedge} below;
- in Figure 2.5A, the points before and after the breakpoint were fit using the same slope, but varying constant (C_1) terms. The breakpoint was selected by visual inspection. Below, the intercepts to the left and right of the breakpoint are referred to as C_{PRC_left} and C_{PRC_right}, respectively.

In total, only two parameters (β_1 and β_2) were used to determine the slopes of all curves, and six parameters in total were used for the entire global fit of nine linear segments, which

minimized the cost function:$\chi^2 = \sum_{i=1}^{N} \left(\frac{\hat{y}_i - y_{fit,i}}{\sigma_i}\right)^2$, where each y_i represents the average measurement of phase shift or peak time and σ_i represents the standard error of that measurement. The reduced chi-squared value of the fit was $\chi_\nu^2 = 5.67$. The best-fit coefficients determined in the fit are summarized in the table below.

Table S2.4. Best-fit values of model parameters.

parameter	**best-fit value**	**95% CI**
β_1	−1.31	[−1.46 −1.17]
β_2	1.79	[1.64 1.95]
C_{PRC_left}	−22.11	[−24.3 −19.9]
C_{PRC_right}	−36.98	[−40.0 −34.0]
C_{wedge}	−24.52	[−26.6 −22.5]
$C_{entrainment}$	39.8	[36.3 43.3]

Simulations of entrainment in the limit cycle geometry model

To simulate entrainment to light-dark cycles of different day length in the geometric resetting framework in Figure 2.6, we modeled an oscillator running along the daytime limit cycle (centered at 0, radius 1) in the light and the nighttime cycle (centered at *X*, radius *R*) in the dark. We set the angular frequency to be $\frac{2\pi \text{ rad}}{24 \text{ hours}}$ in both light and dark. As described in the Mathematical Appendix, dusk and dawn transitions were modeled as radial jumps from one cycle to the nearest point on the other cycle.

We considered values of *R* and *X* spanning six orders of magnitude and studied entrainment to 24-hour cycles with day length lasting from 6 to 18 hours. For each pair of *R* and *X*, we simulated oscillator dynamics in 30 light-dark cycles of a given day length. We judged that an oscillator failed to entrain to a given diurnal schedule if oscillator phases after 29 and 30 cycles were more than π/180 radians apart, or if simulations starting from different initial phases (θ_0 = π/4 and 5π/4) reached phases over π/180 radians apart after 30 light-dark cycles.

For every simulation that passed the entrainment criteria above, we computed the best linear fit and slope m of oscillator phase dependence on day length τ. We assessed goodness of fit by computing the mean fit error, defined as the average absolute value of the deviations between the linear fit and simulation results. If the mean fit error was greater than 10% of the deviation between maximum and minimum phases to which the oscillator entrained for this range of τ, the phase dependence on day length was judged to be non-linear.

Relaxing assumptions of the limit cycle geometry model

The results of the simulations described immediately above strongly suggest that the relative geometry of day and night orbits determines the scaling of entrained phase with day length. However, those simulations are based on idealized infinitely-attracting circular limit cycles with constant angular frequency, assumptions which are likely to be violated for biological clocks. For example, the KaiC phosphorylation limit cycles in Figure 2.6F are somewhat elliptical. We were therefore interested in understanding whether the relative geometry of the limit cycles would be the dominant determinant of oscillator entrainment if our assumptions were relaxed. To this end, we explored entrainment in limit cycle models where these features—(i) orbit attraction strength, (ii) orbit ellipticity, and (iii) variation in angular frequency throughout the cycle—could be treated explicitly.

(i) Orbit attraction strength

To consider the effect of orbit attraction strength (Figure S2.12A), we studied an oscillator with constant angular frequency ω orbiting a circular limit cycle of radius R_{orb} that is exponentially attracting:

$$\dot{\theta} = \omega = \frac{2\pi}{24}\ \frac{\text{rad}}{\text{hr}}$$
$$\dot{r} = -a(r - R_{orb}),$$

where the polar coordinates (r, θ) are defined relative to the center of the limit cycle. Here, the attraction strength a determines the half-time for relaxation to the orbit according to $t_{1/2} = \ln(2)/a$ (hrs). During the day, the equations of motion were integrated with respect to the daytime orbit of radius 1 centered at the origin. At night, the oscillator coordinates were computed with respect to the night limit cycle of radius R centered at (0, X). We considered geometries with R and X ranging over six orders of magnitude and a = 10, 1, and 0.1. For each set of R, X and a, we simulated entrainment to ten 24-hour light-dark cycles of day length τ between 6 and 18 hours starting from two out-of-phase initial conditions ($\theta_0 = 0$ and $\theta_0 = \pi$). After the end of the tenth entraining cycle, the oscillator was allowed to relax back to the daytime orbit. We judged the relaxation to be complete at time t_{relax} when the radial coordinate of the oscillator was within 0.02 units of the daytime orbit ($|r(t_{relax}) - R| < 0.02$). We then computed the "peak time" (t_{pk}) of this oscillator as t_{relax} plus the additional time required to reach phase $\theta = \pi/2$ after return to the orbit. For every simulation that passed the entrainment criteria as defined above, we computed the slope m the best linear fit of oscillator peak time dependence on day length τ. We assessed goodness of fit by computing the mean fit error, defined as the

average absolute value of the deviations between the linear fit and simulation results. The phase dependence on day length was judged to be non-linear if the mean fit error was greater than 0.5 hours and also greater than 10% of the deviation between maximum and minimum peak times to which the oscillator entrained for this range of τ.

(ii) Orbit ellipticity

To consider the effect of orbit ellipticity (Figure S2.12B), we studied an oscillator with constant angular frequency ω orbiting an elliptical limit cycle that is exponentially attracting. We only considered orbits with their minor axes (length R_{orb}) positioned along the x axis and major axes (length $\rho \times R_{orb}$) lying parallel to the y axis. Mathematically, such an oscillator is defined by:

$$\dot{\theta} = \omega = \frac{2\pi}{24}\ \frac{\text{rad}}{\text{hr}}$$
$$\dot{r} = -a \times d_{ellipse}(r, \theta) - \dot{r}_{ellipse}(\theta),$$

where the polar coordinates (r, θ) are defined relative to the center of the limit cycle. Here $d_{ellipse}(r, \theta)$ is the distance from the current point to the nearest point on the ellipse, and $\dot{r}_{ellipse}(\theta)$ measures how the radial coordinate changes as a function of the angle on an elliptical trajectory, assuming that $\dot{\theta}$ is constant. $d_{ellipse}(r, \theta)$ was evaluated numerically at every integration time step using the fminbnd() routine in MATLAB. $\dot{r}_{ellipse}(\theta)$ was computed explicitly based on the definition of the ellipse in polar coordinates: $\dot{r}_{ellipse}(\theta) = -\frac{1}{2}\left(\frac{\cos^2\theta}{R_{orb}^2} + \frac{\sin^2\theta}{\rho^2 R_{orb}^2}\right)^{-3/2}\left(\frac{-2\,\dot{\theta}\cos\theta\sin\theta}{R_{orb}^2} + \frac{2\,\dot{\theta}\cos\theta\sin\theta}{\rho^2 R_{orb}^2}\right)$. For all simulations in Figure S2.12B, the day orbit was centered at (0, 0) with minor axis length 1 and major axis length ρ_D; the night orbit was centered at (0, X) with minor axis length R and major axis length $\rho_N R$. The attraction

strength of both orbits was set to $a = 1$. Entrainment simulations were carried out for 4 light-dark cycles. Slope m was computed as in (i) above.

(iii) Varying angular velocity along the limit cycle

We also considered the case of circular orbits with nonconstant angular velocities (Figure S2.12). To do so, we considered an oscillator defined by the following equations:

$$\dot{\theta} = \omega\left(1 + \frac{\varepsilon}{\omega}\sin\omega t\right)$$
$$\dot{r} = -a(r - R_{orb}),$$

where $\omega = \frac{2\pi}{24}\ \frac{\text{rad}}{\text{hr}}$ is the natural oscillator frequency. As above, the polar coordinates (r, θ) are defined relative to the center of the limit cycle. Such an oscillator completes one full cycle around the orbit within 24 hours, but the oscillator speed varies sinusoidally along the orbit. Here, the ratio ε/ω defines the maximal deviation of the angular velocity from the natural frequency. In the most perturbative case we considered, $\frac{\varepsilon}{\omega} = \frac{1}{2}$, the oscillator runs at 1.5 times the natural frequency at the peak of the oscillation and at 0.5 times natural frequency at the trough of the cycle. Simulations were carried out for ten light-dark cycles for orbits with attraction strength $a = 1$. Slope m was computed as in (i) above.

Simulations of daytime resource allocation in days of different length

Phase of transcriptional dynamics of dawn and dusk genes in Figure S2.13 were derived from a sinusoidal fit to the transcriptional profiles of dawn and dusk genes identified in microarray time courses by Vijayan et al. [50,51]. Briefly, normalized time course data from Vijayan et al. was downloaded from the GEO depository, and time series for transcripts

annotated as dawn genes were averaged to obtain the average dawn gene transcriptional profile. The average dusk gene trajectory was obtained analogously. Average dawn and dusk waveforms were fit to sinusoids with 24-hour period, and the resulting phase estimates were used to define the phase shift between the orange and grey curves in Figure S2.13.

In Figure S2.13, nightfall in LD 12:12 for all values of *m* coincides with the 12-hour dark pulses administered during the initial synchronization in the Vijayan et al. experiment. In simulations of other day lengths (τ), we assumed that the only effect of diurnal cycling is to adjust the phase of the circadian transcriptional program relative to dawn and dusk, without affecting the shape or relative timing of dawn and dusk gene transcriptional waveforms. The bias in allocation of daytime resources between dawn and dusk genes was then computed according to the expression: $\frac{I(dawn\ gene)-I(dusk\ gene)}{I(dawn\ gene)+I(dusk\ gene)}$, where $I(gene)$ is the integrated RNA signal for that gene over the daytime hours.

MATHEMATICAL APPENDIX

Here we outline a simple and general mathematical framework for describing the interaction between a circadian clock and its environment. The essential idea is that we model only the phase of the oscillator and decompose its dynamics into a sequence of free runs interrupted by step responses to changes in the environment (Figure S2.14). We present the assumptions of the model and then derive key formulas for interpreting our measurements.

Modeling a Circadian Clock as a Phase Oscillator With Linear Response to Light-Dark Cues

Circadian rhythms are characterized by the ability to maintain self-sustaining ≈24-hour oscillations in constant conditions and to adjust the phase of those oscillations in response to environmental signals (e.g., transitions between light and dark). To represent the first feature, we model a circadian clock as an oscillator that runs along a "light" limit cycle with speed ω_L when lights are on, and along a "dark" limit cycle with speed ω_D when lights are off (Figure S2.14A). Because the oscillator is always on one of the limit cycles, its state can be fully described by a single variable, the phase $\theta(t)$:

$$\frac{d\theta}{dt} = \omega_L \quad \text{(in light)}$$

$$\frac{d\theta}{dt} = \omega_D \quad \text{(in dark)}$$

We define frequencies in units of cycles per hour (1 cycle $= 2\pi$ radians), so that the duration of one cycle in constant conditions is $T = 1/\omega$ hours, and phase $\theta(t)$ is defined between 0 and 1.

We assume that the oscillator transitions between the two limit cycles immediately at dark-to-light ("dawn") and light-to-dark ("dusk") transitions, with a change in phase. We define $L(\theta)$ and $D(\theta)$ as phase-shifts accompanying clock responses to lights on and lights off cues, respectively:

$$\theta(t) \rightarrow \theta(t) + L(\theta(t)) \quad \text{(at dark-to-light)}$$

$$\theta(t) \rightarrow \theta(t) + D(\theta(t)) \quad \text{(at light-to-dark)}$$

Though in principle $L(\theta)$ and $D(\theta)$ could be arbitrary periodic functions, our measurements in Figure 2.3 suggest that $L(\theta)$ and $D(\theta)$ are approximately linear over the range of clock phases when dawn and dusk occurred in our experiments. Henceforth we consequently assume that L and D are linear functions of θ:

$$L(\theta) = -l(\theta - \theta_L)$$

$$D(\theta) = -d(\theta - \theta_D).$$

Given this framework, we can now determine the change in clock state over any interval simply by adding the changes in phase at the transitions and accumulated during the free runs. We now explicitly compute the change in clock state in response to a dark pulse and the state of stable entrainment for light-dark cycles of arbitrary period.

Modeling Phase Resetting

To probe the response of an oscillator, one can subject it to a perturbation of duration δ and compare the resulting phase to that of an unperturbed oscillator. Plotting the results of such an assay as a function of the phase θ_t at which the perturbation is delivered yields a phase response curve (PRC; Figure S2.14C, Figure 2.5A). Alternatively, varying the duration of the

perturbation while delivering it at a fixed phase corresponds to a "wedge" experiment (Figure 2.5B).

To determine the phase response, we need to determine the phase evolution as the system transitions to dark, free runs in the dark, and then transitions to light. Note that because this model treats the transitions between the light and dark cycles as instantaneous, we expect that it will only be valid for dark pulses that are long compared to the true relaxation time of the clock. Mathematically,

$$\theta'_{t+\delta,+} = \theta_t + D(\theta_t) + \delta\omega_D + L\left(\theta'_{t+\delta,-}\right),$$

where the prime denotes the perturbed oscillator, and the + and – in the subscripts distinguish the phase after and before the transition from dark-to-light at $t + \delta$. (That is, $\theta'_{t+\delta,-} = \theta_t + D(\theta_t) + \delta\omega_D$.) Substituting the linear forms above for D and L and grouping like terms,

$$\theta'_{t+\delta,+} = \theta_t[(1-d)(1-l)] + \delta(1-l)\omega_D + [(1-l)d\theta_D + l\theta_L].$$

Subtracting the unperturbed phase $\theta_{t+\delta} = \theta_t + \delta\omega_L$,

$$\Delta\theta = \theta'_{t+\delta,+} - \theta_{t+\delta} = \theta_t[ld - d - l] + \delta[(1-l)\omega_D - \omega_L] + [(1-l)d\theta_D + l\theta_L].$$

Thus we obtain a formula for the change in phase in response to a dark pulse, with linear dependences on the phase of the perturbation, θ_t, and its duration, δ.

Modeling Entrainment to Light-Dark Cycles

We can similarly describe the phase of a clock stably entrained to light-dark cycles of varying day length. To this end, consider a phase oscillator subjected to light-dark cycles of period T and day length τ (Figure S2.14D). In this case, rather than a phase difference, we need

to determine θ_τ such that $\theta_{T+\tau} = \theta_\tau + 1$. If this condition is met, the oscillator is stably entrained to a cycle of period *T*. In other words, we enforce periodicity.

Proceeding analogously to above, we determine the evolution over a full driving period, starting at dusk. This comprises a transition to the dark at time τ, free run in the dark for duration $T - \tau$, a transition to the light at time T, and free run in the light for duration τ. Mathematically,

$$\theta_{T+\tau} = \theta_\tau + D(\theta_\tau) + \omega_D(T - \tau) + L(\theta_T) + \omega_L\tau.$$

Again, substituting the linear forms above for D and L and grouping like terms,

$$\theta_{T+\tau} = \theta_\tau[(1-d)(1-l)] + T(1-l)\omega_D + \tau[(1-l)\omega_D - \omega_L] + [(1-l)d\theta_D + l\theta_L].$$

Setting $\theta_{T+\tau} = \theta_\tau + 1$ and solving for θ_τ,

$$\theta_\tau = \tau\frac{(1-l)\omega_D - \omega_L}{ld - d - l} - T\frac{(1-l)\omega_D}{ld - d - l} - \frac{(1-l)d\theta_D + l\theta_L - 1}{ld - d - l}.$$

Again, we obtain a formula with linear dependence, here on the day length τ and the driving period T.

Comparison with Experiment

The expressions above describe phases, but we do not measure phase directly. Rather, we measure the time of peak expression of a reporter. Thus it is necessary to convert from phase to the time of peak expression. To this end, we arbitrarily assign the peak expression to occur at $\theta = 0.5$ (midway through the cycle). Because phase advance and delay correspond to earlier and later peak times respectively, the time of the peak shifts with opposite sign to the phase. In each case above, we are interested when the peak (or $\theta = 0.5$) occurs relative to the last dawn (i.e., immediately after the action of *L*). We can solve for this peak time:

$$t_{pk} = \frac{0.5 - \theta_x}{\omega_L},$$

where $x = t + \delta$ (end of dark pulse) in the case of phase resetting and $x = 0$ (last dawn) in the case of entrainment. To solve for t_{pk} in entrained conditions, we make use of the fact that $\theta_0 = \theta_\tau - \omega_L \tau$, allowing us to substitute the expression above for θ_τ. For phase resetting, we must apply this formula to both the perturbed and unperturbed phase and then subtract: $\Delta t_{pk} = t_{pk}(\theta'_{t+\delta+}) - t_{pk}(\theta_{t+\delta}) = -\Delta\theta/\omega_L$.

Furthermore, we note that certain combinations of the frequencies ω_L and ω_D and the linear sensitivities l and d occur repeatedly. We thus define

$$\beta_1 = \frac{\omega_D}{\omega_L}\left[\frac{(1-l)}{ld - d - l}\right]$$

$$\beta_2 = -\frac{1}{ld - d - l}.$$

Then, for phase resetting

$$\Delta t_{pk} = \theta_t\left(\frac{1}{\omega_L \beta_2}\right) + \delta\left(1 + \frac{\beta_1}{\beta_2}\right) + C_1$$

and for entrainment

$$t_{pk} = \tau(1 - \beta_1 - \beta_2) + T\beta_1 + C_2,$$

where C_1 and C_2 are constants that do not depend on θ_t, δ, τ, or T.

In the global fits for all datasets in Figure 2.5A-C, we varied β_1 and β_2 to simultaneously fit Δt_{pk} to our phase-resetting and wedge data and t_{pk} to our seasonal entrainment data. Thus, the slopes of all the linear fits in Figure 2.5A-C were derived from the same values of β_1 and β_2. See Computational Methods for further details.

Geometric Resetting

In our experimental measurements, we observed *L* and *D* step-response functions with linear regions with slopes < 1. Here we present a simple dynamical systems picture where a tunable, linear dependence of phase shift magnitude on oscillator phase arises from the geometry of how a strongly attracting limit cycle is deformed by a changing external input.

We suppose that the oscillator during the day is described by a circular limit cycle in the plane with unit radius. During the night, we assume that the limit cycle remains in the plane, but is offset a distance *X* from the daytime cycle and has an altered radius *R* (Figure 2.6A). At the moment of the light-to-dark transition, the state of the system is on the daytime limit cycle—it is then attracted to the nighttime limit cycle. The step-response function $D(\theta)$ describes the shift between the new phase angle (measured relative to the center of the nighttime limit cycle) and the original phase θ (Figure 2.6).

If we place the origin at the center of the nighttime limit cycle, the Cartesian coordinates of the system state immediately before the light-to-dark transition, when the system is still on the daytime orbit, are:

$$(\cos\theta + X, \sin\theta)$$

If we assume that the fixed point giving rise to the nighttime orbit is very strongly attracting, then the system approaches the limit cycle much faster than any circulation occurs. In this limit, the light-to-dark transition leads to a purely radial jump from the daytime orbit towards the center of the nighttime orbit (Figure 2.6A-B). Under these conditions, the new phase θ_{night} on the nighttime cycle is simply the angle measured relative to the center of the new limit cycle:

$$\theta_{\text{night}} = \tan^{-1}\left(\frac{\sin\theta}{\cos\theta + X}\right)$$

To develop intuition about how this mapping between phase on day and night orbits is affected by their geometric arrangement, we can perform a Taylor expansion for angles near $\theta = 0$ at dusk, corresponding to conditions close to LD 12:12:

$$\theta_{\text{night}} \approx \frac{\theta}{1 + X}$$

Likewise, it can be shown that for transitions from nighttime to daytime cycles, near $\theta = \pi$, the phase immediately after transition to the daytime cycle at dawn can be given by:

$$\theta_{\text{day}} \approx \frac{\theta}{X/R + 1}$$

These expressions show that, in the linear portion of the step response function, angles are compressed by a factor tunable by the relative geometry of the light and dark limit cycles. In this way, the geometric arrangement of the limit cycles sets the slopes of $L(\theta)$ and $D(\theta)$. Numerical simulations in Figure 2.6 and Figure S2.12 were carried out using trigonometric formulas as above to convert phases between the daytime and nighttime limit cycles. Details of simulations in Figure S2.12 are described in Computational Methods.

REFERENCES

1. de Montaigu, A., Giakountis, A., Rubin, M., Tóth, R., Cremer, F., Sokolova, V., Porri, A., Reymond, M., Weinig, C., and Coupland, G. (2015). Natural diversity in daily rhythms of gene expression contributes to phenotypic variation. Proceedings of the National Academy of Sciences of the United States of America *112*, 905–10.

2. Rémi, J., Merrow, M., and Roenneberg, T. (2010). A circadian surface of entrainment: varying T, τ, and photoperiod in Neurospora crassa. Journal of biological rhythms *25*, 318–328.

3. Herzog, E.D. (2007). Neurons and networks in daily rhythms. Nature reviews. Neuroscience *8*, 790–802.

4. Daan, S., Beersma, D.G.M., and Spoelstra, K. (2003). Dawn and Dusk – specialisation of circadian system components for acceleration and deceleration in response to light? In Biological Rhythms (10th Sapporo Symposium), K. Honma and S. Honma, eds., pp. 110–125.

5. Nishiwaki, T., Satomi, Y., Nakajima, M., Lee, C., Kiyohara, R., Kageyama, H., Kitayama, Y., Temamoto, M., Yamaguchi, A., Hijikata, A., *et al.* (2004). Role of KaiC phosphorylation in the circadian clock system of Synechococcus elongatus PCC 7942. Proceedings of the National Academy of Sciences of the United States of America *101*, 13927–32.

6. Rust, M.J., Markson, J.S., Lane, W.S., Fisher, D.S., and O'Shea, E.K. (2007). Ordered phosphorylation governs oscillation of a three-protein circadian clock. Science (New York, N.Y.) *318*, 809–12.

7. Flombaum, P., Gallegos, J.L., Gordillo, R. a, Rincón, J., Zabala, L.L., Jiao, N., Karl, D., Li, W., Lomas, M., Veneziano, D., *et al.* (2013). Present and future global distributions of the marine Cyanobacteria Prochlrococcus and Synechococcus. Pnas *110*, 9824–9829.

8. Liu, Y., Tsinoremas, N.F., Johnson, C.H., Lebedeva, N. V, Golden, S.S., Ishiura, M., and Kondo, T. (1995). Circadian orchestration of gene expression in cyanobacteria. Genes & development *9*, 1469–78.

9. Ito, H., Mutsuda, M., Murayama, Y., Tomita, J., Hosokawa, N., Terauchi, K., Sugita, C., Sugita, M., Kondo, T., and Iwasaki, H. (2009). Cyanobacterial daily life with Kai-based circadian and diurnal genome-wide transcriptional control in Synechococcus elongatus. Proceedings of the National Academy of Sciences of the United States of America *106*, 14168–73.

10. Hosokawa, N., Hatakeyama, T.S., Kojima, T., Kikuchi, Y., Ito, H., Iwasaki, H., Mutsuda, M., Murayama, Y., Tomita, J., Hosokawa, N., *et al.* (2011). Circadian transcriptional regulation by the posttranslational oscillator without de novo clock gene expression in

Synechococcus. Proceedings of the National Academy of Sciences of the United States of America *108*, 15396–401.

11. Tomita, J., Nakajima, M., Kondo, T., and Iwasaki, H. (2005). No transcription-translation feedback in circadian rhythm of KaiC phosphorylation. Science (New York, N.Y.) *307*, 251–4.

12. Zhang, C.C., Jeanjean, R., and Joset, F. (1998). Obligate phototrophy in cyanobacteria: more than a lack of sugar transport. FEMS Microbiology Letters *161*, 285–292.

13. Nakajima, M., Imai, K., Ito, H., Nishiwaki, T., Murayama, Y., Iwasaki, H., Oyama, T., and Kondo, T. (2005). Reconstitution of circadian oscillation of cyanobacterial KaiC phosphorylation in vitro. Science (New York, N.Y.) *308*, 414–5.

14. Kageyama, H., Nishiwaki, T., Nakajima, M., Iwasaki, H., Oyama, T., and Kondo, T. (2006). Cyanobacterial Circadian Pacemaker: Kai Protein Complex Dynamics in the KaiC Phosphorylation Cycle In Vitro. Molecular cell *23*, 161–171.

15. Rust, M.J., Golden, S.S., and O'Shea, E.K. (2011). Light-driven changes in energy metabolism directly entrain the cyanobacterial circadian oscillator. Science (New York, N.Y.) *331*, 220–3.

16. Kim, Y.-I., Vinyard, D.J., Ananyev, G.M., Dismukes, G.C., and Golden, S.S. (2012). Oxidized quinones signal onset of darkness directly to the cyanobacterial circadian oscillator. Proceedings of the National Academy of Sciences of the United States of America *109*, 17765–9.

17. Phong, C., Markson, J.S., Wilhoite, C.M., and Rust, M.J. (2013). Robust and tunable circadian rhythms from differentially sensitive catalytic domains. Proceedings of the National Academy of Sciences of the United States of America *110*, 1124–9.

18. Pattanayak, G.K., Phong, C., and Rust, M.J. (2014). Rhythms in energy storage control the ability of the cyanobacterial circadian clock to reset. Current Biology *24*, 1934–1938.

19. Chang, Y.-G., Tseng, R., Kuo, N.-W., and LiWang, A. (2012). Rhythmic ring-ring stacking drives the circadian oscillator clockwise. Proceedings of the National Academy of Sciences of the United States of America *109*, 16847–51.

20. Heisler, J., Chang, Y.-G., Chavan, A., and LiWang, A. Real-time In Vitro Fluorescence Anisotropy of the Cyanobacterial Circadian Clock (in press). In Circadian Clocks Methods and Protocols (in press), S. Brown, ed. (Springer).

21. Takai, N., Nakajima, M., Oyama, T., Kito, R., Sugita, C., Sugita, M., Kondo, T., and Iwasaki, H. (2006). A KaiC-associating SasA-RpaA two-component regulatory system as a major circadian timing mediator in cyanobacteria. Proceedings of the National Academy of Sciences of the United States of America *103*, 12109–14.

22. Gutu, A., and O'Shea, E.K. (2013). Two antagonistic clock-regulated histidine kinases time the activation of circadian gene expression. Molecular cell *50*, 288–94.

23. Markson, J.S., Piechura, J.R., Puszynska, A.M., and O'Shea, E.K. (2013). Circadian Control of Global Gene Expression by the Cyanobacterial Master Regulator RpaA. Cell *155*, 1396–1408.

24. Johnson, C.H. (1999). Forty years of PRCs--what have we learned? Chronobiology international *16*, 711–743.

25. Schmitz, O. (2000). CikA, a Bacteriophytochrome That Resets the Cyanobacterial Circadian Clock. Science *289*, 765–768.

26. Pfeuty, B., Thommen, Q., and Lefranc, M. (2011). Robust entrainment of circadian oscillators requires specific phase response curves. Biophysical Journal *100*, 2557–2565.

27. Ouyang, Y. (1998). The Biological Significance of the Circadian Clock in Cyanobacteria. *33*.

28. Woelfle, M., Ouyang, Y., Phanvijhitsiri, K., and Johnson, C. (2004). The adaptive value of circadian clocks: an experimental assessment in cyanobacteria. Current Biology *14*, 1481–1486.

29. Pittendrigh, C.S. (1972). Circadian surfaces and the diversity of possible roles of circadian organization in photoperiodic induction. Proceedings of the National Academy of Sciences of the United States of America *69*, 2734–2737.

30. Spoelstra, K., Wikelski, M., Daan, S., Loudon, A.S.I., and Hau, M. (2015). Natural selection against a circadian clock gene mutation in mice. Proceedings of the National Academy of Sciences, 201516442.

31. Pittendrigh, C.S., and Minis, D.H. (1972). Circadian systems: longevity as a function of circadian resonance in Drosophila melanogaster. Proceedings of the National Academy of Sciences of the United States of America *69*, 1537–1539.

32. Daan, S., Albrecht, U., van der Horst, G.T., Illnerová, H., Roenneberg, T., Wehr, T. a, and Schwartz, W.J. (2001). Assembling a clock for all seasons: are there M and E oscillators in the genes? Journal of biological rhythms *16*, 105–116.

33. Edwards, K.D., Akman, O.E., Knox, K., Lumsden, P.J., Thomson, A.W., Brown, P.E., Pokhilko, A., Kozma-Bognar, L., Nagy, F., Rand, D.A., *et al.* (2010). Quantitative analysis of regulatory flexibility under changing environmental conditions. Molecular systems biology *6*, 424.

34. Hut, R. a., Oort, B.E.H. Van, and Daan, S. (1999). Natural Entrainment without Dawn and Dusk: The Case of the European Ground Squirrel (Spermophilus citellus). Journal of Biological Rhythms *14*, 290–299.

35. Hut, R., Paolucci, S., Dor, R., Kyriacou, C.P., and Daan, S. (2013). Latitudinal clines: an evolutionary view on biological rhythms. Proceedings. Biological sciences / The Royal Society *280*, 20130433.

36. Wehr, T. a (2001). Photoperiodism in humans and other primates: evidence and implications. Journal of biological rhythms *16*, 348–364.

37. Rand, D. a, Shulgin, B. V, Salazar, D., and Millar, a J. (2004). Design principles underlying circadian clocks. Journal of the Royal Society, Interface / the Royal Society *1*, 119–30.

38. Diamond, S., Jun, D., Rubin, B.E., and Golden, S.S. (2015). The circadian oscillator in Synechococcus elongatus controls metabolite partitioning during diurnal growth. Proceedings of the National Academy of Sciences *2015*, 201504576.

39. Yoshida, T., Murayama, Y., Ito, H., Kageyama, H., and Kondo, T. (2009). Nonparametric entrainment of the in vitro circadian phosphorylation rhythm of cyanobacterial KaiC by temperature cycle. Proceedings of the National Academy of Sciences of the United States of America *106*, 1648–53.

40. Pittendrigh, C.S., and Daan, S. (1976). A functional analysis of circadian pacemakers in nocturnal rodents - IV. Entrainment: Pacemaker as clock. Journal of Comparative Physiology A *106*, 291–331.

41. Daan, S. (2000). The Colin S . Pittendrigh Lecture: Colin Pittendrigh, Jürgen Aschoff, and the Natural Entrainment of Circadian Systems. Journal of Biological Rhythms, 195–207.

42. Pittendrigh, C.S., and Minis, D.H. (1964). The Entrainment of Circadian Oscillations by Light and Their Role as Photoperiodic Clocks. The American Naturalist *98*, 261.

43. Johnson, C.H., Elliott, J. a, and Foster, R. (2003). Entrainment of circadian programs. Chronobiology international *20*, 741–74.

44. Winfree, A. (1973). The Investigation of Oscillatory Processes by Perturbation Experiments. In Biological and Biochemical Oscillators, B. Chance, A. Ghosh, and E. K. Pye, eds. (New York, New York, USA: Academic Press, Inc.), p. 461.

45. Chen, Y., Kim, Y.I., Mackey, S.R., Holtman, C.K., LiWang, A., and Golden, S.S. (2009). A novel allele of kaiA shortens the circadian period and strengthens interaction of oscillator components in the cyanobacterium Synechococcus elongatus PCC 7942. Journal of Bacteriology *191*, 4392–4400.

46. Nair, U., Ditty, J., Min, H., and Golden, S. (2002). Roles for Sigma Factors in Global Circadian Regulation of the Cyanobacterial Genome. Journal of bacteriology *184*.

47. Lin, J., Chew, J., Chockanathan, U., and Rust, M.J. (2014). Mixtures of opposing phosphorylations within hexamers precisely time feedback in the cyanobacterial circadian clock. Proceedings of the National Academy of Sciences *111*, E3937–E3945.

48. Leypunskiy, E. (2017). Simulations_and_analysis_pipelines_github_repo.

49. Press, W.H., Teukolsky, S. a, Vettering, W.T., and Flannery, B.P. (1992). Modeling of Data. In Numerical Recipes in Fortran 77: The Art of Scientific Computing (Cambridge University Press), pp. 650–699.

50. Vijayan, V., Zuzow, R., and O'Shea, E.K. (2009). Oscillations in supercoiling drive circadian gene expression in cyanobacteria. Proceedings of the National Academy of Sciences of the United States of America *106*, 22564–8.

51. Vijayan, V., Zuzow, R., and O'Shea, E.K. (2009). Oscillations in supercoiling drive circadian gene expression in cyanobacteria.

Chapter 3 GEOGRAPHICALLY RESOLVED RHYTHMS IN TWITTER USE REVEAL SOCIAL PRESSURES ON DAILY ACTIVITY PATTERNS

This chapter is a draft of a manuscript in preparation for submission to *Current Biology*.

Eugene Leypunskiy[1], Emre Kıcıman[2], Olivia J. Walch[3], Andrey Rzhetsky[4], Aaron R. Dinner[5,*], Michael J. Rust[6,*]

[1] Graduate Program in Biophysical Sciences, The University of Chicago, Chicago, IL 60637

[2] Information and Data Science Group, Microsoft Research, Redmond, WA, 98052

[3] Department of Mathematics, University of Michigan, Ann Arbor, MI 48109

[4] Departments of Medicine, Human Genetics, and the Computational Institute, The University of Chicago, Chicago, IL 60637

[5] Department of Chemistry and the James Franck Institute, The University of Chicago, Chicago, IL 60637

[6] Department of Molecular Genetics and Cell Biology and Department of Physics, The University of Chicago, Chicago, IL 60637

ABSTRACT

Daily rhythms in human physiology and behavior are driven by the interplay of circadian rhythms, environmental cycles, and social schedules. Much research has focused on the mechanism and function of circadian rhythms in controlled laboratory settings, most often in constant conditions or in idealized light-dark environments. There have been comparatively few studies into how social pressures, such as work and school schedules, affect human activity rhythms day to day and season to season. To address this issue, we analyzed activity on Twitter in >1,500 US counties throughout the 2012-2013 calendar years in 15-min intervals, using geographically tagged tweets representing ≈0.1% of the total population each day. We find that periods of low Twitter activity are consistent with geographical patterns of human sleep recorded in conventional surveys. We show that the nighttime lull in Twitter activity is generally shifted to later times on weekends relative to weekdays, a phenomenon we term "Twitter social jet lag." The magnitude of this social jet lag varies seasonally and geographically, with the West Coast experiencing less Twitter social jet lag compared to the Central and Eastern US, and is correlated with average commuting schedules and disease risk factors such as obesity. Most counties experience the largest amount of Twitter social jet lag in February and the lowest in June or July, when the onset of Twitter activity on weekdays is surprisingly shifted later in the day. We present evidence that these shifts in weekday activity coincide with relaxed social pressures due to local K-12 school holidays, and that the direct seasonal effect of altered day length is comparatively weaker.

INTRODUCTION

The daily pattern of activity and rest in human life is familiar to all of us, and there is a growing body of evidence indicating that disrupting this rhythm has severe consequences for health [1,2]. Despite its importance, it is poorly understood how daily patterns of activity vary geographically and seasonally. Further, it is unclear what influence biological clocks and social constraints have on activity patterns outside of a controlled laboratory setting [3]. Circadian clocks provide an innate pressure to sleep at night and be active during the day, but the internal rhythms of the circadian clock can be at odds with the timing of social obligations, such as work and school. Indeed, studies suggest that when people deliberately disconnect from such social constraints and spend time without alarm clocks or electric lights, their sleep-wake rhythms shift to align to sunrise and sunset [4,5]. In non-industrialized societies without access to electricity, activity is similarly timed according to availability of daylight [6,7]. However, in the modern "24-hour society," which makes available round-the-clock food, entertainment, and social interaction, many people live out of synchrony with the pattern of sunrise and sunset [8,9].

To quantify how social pressures disrupt the natural activity patterns of humans in industrialized societies, Roenneberg and colleagues introduced the concept of "social jet lag," defined as the difference between the midpoints of sleep on work and free days [10]. Extensive surveys of sleep timing in Central Europe have revealed that almost 70% of respondents experience over 1 hr of social jet lag, and nearly a third experience over 2 hr, suggesting that, as the name implies, our internal rhythms are forced to constantly readjust to shifting social demands on a weekly basis [11]. People employed on evening, night, or rotating shifts, who

currently comprise roughly 20% of workers [12,13], contend with the most extreme social jet lag (1-6 hr) [14].

The widespread mismatch between sleep timing on work and free days appears to have negative consequences for human health [15,16]. Social jet lag magnitude has been shown to correlate with the likelihood of smoking, consumption of alcohol and caffeine [2,10,11,17], and mood disorders [18,19]. Additionally, social jet lag has been implicated as a risk factor for metabolic dysfunction and obesity [20–22], and it is thought to lower academic performance [23–25]. Some of these effects may be exacerbated in proverbial "night owls," for whom social jet lag goes hand-in-hand with chronic sleep debt accumulated during the workweek [1].

Given the mounting evidence of the negative effects of social jet lag on human health and performance, it is important to gain a systematic understanding of how social jet lag varies with social and geographic factors. It is not known how the amount of social jet lag varies from region to region, and whether cultural factors play a role independently of latitude and longitude. It is also poorly understood to what extent there are seasonal variations in social jet lag and, more generally, in the timing of daily rhythms of human activity, and how much they are affected by social and geographic pressures.

To gain a complete picture of the diversity of human activity rhythms and uncover possible demographic and environmental correlates, it is necessary to collect data on natural activity patterns of populations with different cultural norms, in different locations, and at different times of year [3,26]. The advent of mobile devices and wearable activity trackers is enabling collection of unprecedented amounts of data on human behavior *in situ*, surpassing the geographic reach and temporal resolution typically achieved with surveys [26–30]. In particular,

Twitter logs have become popular sources of accessible, easily-minable observations of social interactions in space and time among hundreds of millions of people [30,31]. These data present new opportunities for characterizing daily activity rhythms, and several studies have analyzed Twitter activity for this purpose [32–35]. One such study concluded that a single user's Twitter activity record can be used to infer sleep-wake patterns [32], and, intriguingly, another found evidence of social jet lag in German-speaking users [33]. In parallel, the ability to mine the contents of tweets has enabled researchers to detect how mood and emotional states change diurnally and seasonally, suggesting that Twitter can be a powerful tool to study how activity schedules are linked with emotional wellbeing [34,35].

In this work, we study daily rhythms in Twitter activity in approximately half of the counties in the United States over a two-year timespan (2012-2013), monitoring the average activity of ≈0.1% of the population every day, county-by-county, in 15-min time intervals. This dataset provides us with a unique opportunity to understand how 24-hr activity patterns vary geographically across the United States, and to examine how daily rhythms in Twitter usage correlate with county-level demographics. Crucially, the ability to monitor how Twitter activity patterns change season-to-season and county-by-county allows us to separately assess the influences of the socially defined calendar and changes in daylight hours throughout the year.

We focus on how daily rhythms in Twitter usage are affected by four kinds of characteristics of US counties: (i) geographic coordinates, (ii) seasonal variation in sunrise and sunset at each location (i.e., "solar calendar"), (iii) school and federal holidays, which are social pressures that change seasonally (i.e., the "social calendar"), and (iv) other social factors that we consider static throughout the year (e.g., demographic, socioeconomic and health factors).

We find that each county has a unique temporal signature of Twitter activity, with a peak in afternoon or evening hours and a trough during nighttime. By separately studying activity patterns on weekends and weekdays, we detect an analog of social jet lag in this signal and analyze how it varies over the year. In many US counties, shifts in patterns of activity on weekdays decrease Twitter social jet lag during the summer break in the school calendar and during major holidays, suggesting that this socially imposed calendar is a major factor determining the daily timing of human activity.

RESULTS

County-level records of Twitter activity report on the aggregate daily behavior of over 240,000 users in over 1,500 US counties

We analyzed all publicly-visible geolocated tweets that were sent in 2012-2013 by users in the United States. After applying a cutoff to ensure a sufficient number of users per county, the final dataset contains, for each day on average, tweets from ≈246,000 Twitter users located in 1,521 counties spanning all 50 US states and Washington, DC. The number of daily Twitter users in our dataset from a given county is proportional to the county population (Pearson ρ=0.95, p-value<7e-15). On an average day in 2012-2013, our dataset contains tweets from 0.018-0.38% of the population in every represented county (Figure S3.1A). For comparison, this dataset captures activity from as many individuals on every calendar day as the total number of records in the MCTQ database to-date and about half as many individuals as are interviewed annually in the CDC Behavioral Risk Factor Surveillance Survey [3,36].

To study daily patterns of activity on Twitter on a county-by-county basis, we aggregated tweeting events into 15-minute bins. For each county, 24-hr activity profiles were averaged across all users. We normalized each user's activity pattern, giving equal weight to each user on a given day, and then normalized the signal from every calendar day in each county (Figure 3.1A). This suppresses the impact of both highly-active users and of unusually active days (e.g., notable events and holidays). We refer to the resulting profile as a "tweetogram," showing the normalized pattern of activity in a US county by analogy with the traditional "actograms" used to display logs of activity of individuals in laboratory studies [37].

Nighttime periods of low Twitter activity correspond to patterns of sleep across the United States

In Figure 3.1B, we show an averaged tweetogram for Cook County, IL, home to the city of Chicago. Twitter activity is lowest at night, hitting a minimum around 4:30 a.m., then increases until a local maximum (≈13 hr or 1 p.m.) following conventional lunchtime and decreases until a local minimum in late afternoon (≈16 hr or 4 p.m.) near the end of conventional workday [38]. Tweeting becomes more frequent in the evening, peaking around the time when many people have dinner (≈19 hr or 7 p.m.) [38], and then decreases again until the nighttime trough, consistent with previous reports [39]. We focused our analysis on the troughs of the tweetograms because they are the most pronounced and consistent features of activity profiles among different counties. The trough position indicates the time at which Twitter users in a county are most inactive. The trough width reflects the typical interval over which users are inactive, though it may also be affected by variability in schedules between users. We checked

that tweetogram widths depend only weakly on the prevalence of Twitter usage (Figure S3.1B), which argues against the possibility that troughs appear wider in counties with fewer Twitter users simply because low-activity portions of the tweetograms are sparsely sampled in these counties.

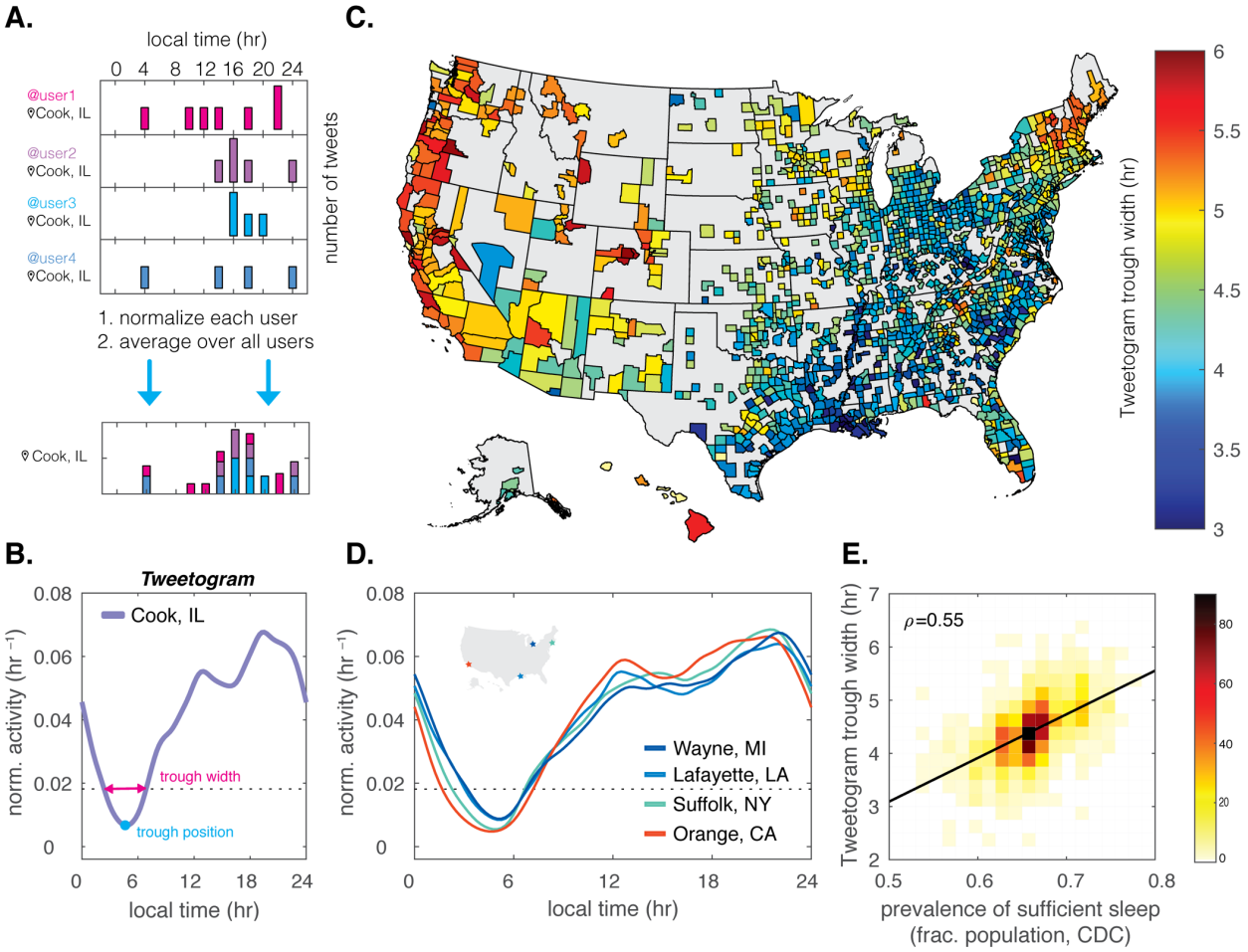

Figure 3.1. Daily rhythms in Twitter activity are related to sleep patterns across the US. (**A**) Methodology for collection of Twitter activity data and aggregation across independent users. Each user's Twitter activity (number of tweets) was binned into 15-min windows spanning the 2012 and 2013 calendar years. Activity counts were then normalized such that the total activity for each user over every calendar day summed to 1 (to suppress bots and highly active users). Normalized counts averaged over all users in the same US county make up the "tweetogram" for that county. Geo-location metadata of the tweets was used to assign users to counties. The dataset was limited to users who geotagged their tweets in 2012-2013 and only to those counties with a median activity of over 10 tweets per day.

(Figure 3.1 continued) (**B**) Example tweetogram showing the average 24-hr Twitter activity profile in 2012-2013 for Cook County, IL. The total signal from each day was normalized so that every calendar day contributes equally to the average. The resulting curve was smoothed using a 150-minute Gaussian kernel.
(C) Map of US counties colored according to the trough width of each county's tweetogram based on all calendar days in 2012-2013. Data from each county was processed as in (B). The positions of tweetogram troughs were determined via parabolic fitting; trough widths were computed at 0.25× the median tweetogram height among all 1521 counties in the dataset. Grey regions represent counties missing from the dataset. Color limits are set to the 1st and 99th percentiles of the data.
(D) Tweetograms for four US counties with different tweetogram widths. Curves are colored using the color scale in (C). The dotted line marks the height at which tweetogram widths were computed. Inset indicates geographical locations of the counties.
(E) The width of tweetogram troughs correlates with the prevalence of sufficient sleep (Pearson's ρ=0.55, p-value < 1e-120). Tweetogram widths for all counties in the Twitter dataset are plotted against county-level data on the prevalence of sufficient sleep collected by the CDC using telephone surveys. Prevalence of sufficient sleep is defined as the fraction of the population sleeping over 7 hours per night. Line of best fit determined by linear regression.

We hypothesized that the nighttime lull in activity represents the time period when most users are asleep. To test this idea, we characterized the positions and widths of the tweetogram troughs for all counties in our dataset. When we marked the trough widths on a map of the US (Figure 3.1C), we observed a striking geographic dependence. The nighttime troughs of Twitter activity profiles are widest on the West Coast and become progressively narrower towards the Great Lakes and the Southeast of the US. Figure 3.1D shows four example counties that illustrate the broader trend: the nighttime lull in Twitter activity in Orange County, CA, is 5.5 hr wide; that is over an hour longer than in Suffolk County, NY, in the Northeast (4.4 hr), and almost two hours longer than in Wayne County, MI (3.6 hr) in the Midwest or in Lafayette County, LA, in the Southeast (3.8 hr).

To check if the widths of the nighttime lulls in Twitter activity correlate with patterns of sleep, we compared our calculations with the county-level data on the prevalence of sufficient sleep collected by the Centers for Disease Control and Prevention of the United States (CDC)

(Figure 3.1E) [36]. The correlation between sleep survey data and tweetogram widths suggest that the period of lowest activity on Twitter reflects regional sleep patterns.

Daily rhythms of activity on Twitter exhibit social jet lag

Roenneberg and colleagues defined social jet lag for an individual as the difference in midsleep points between work days and free days. To study an analog of this phenomenon in our aggregated Twitter data, we defined "Twitter social jet lag" for a county as the shift in trough positions between weekends and weekdays based on our earlier observation that tweetogram troughs are correlated with sleep statistics (Figure 3.1E). We then calculated Twitter activity profiles averaged separately over weekdays and weekends for each county in our dataset, taking care to avoid major holidays in the work and school calendar (Figure 3.2 caption). We find that tweetogram troughs generally occur later on weekends than weekdays, even as the timing of afternoon and evening activity patterns is relatively unchanged (Figure 3.2A-B). For example, in Lafayette County, LA, the trough of the weekend tweetogram is translated over 90 minutes later in the day relative to the trough of the weekday tweetogram (Figure 3.2B). By contrast, the corresponding shift in Orange County, CA, is only about 50 minutes (Figure 3.2A).

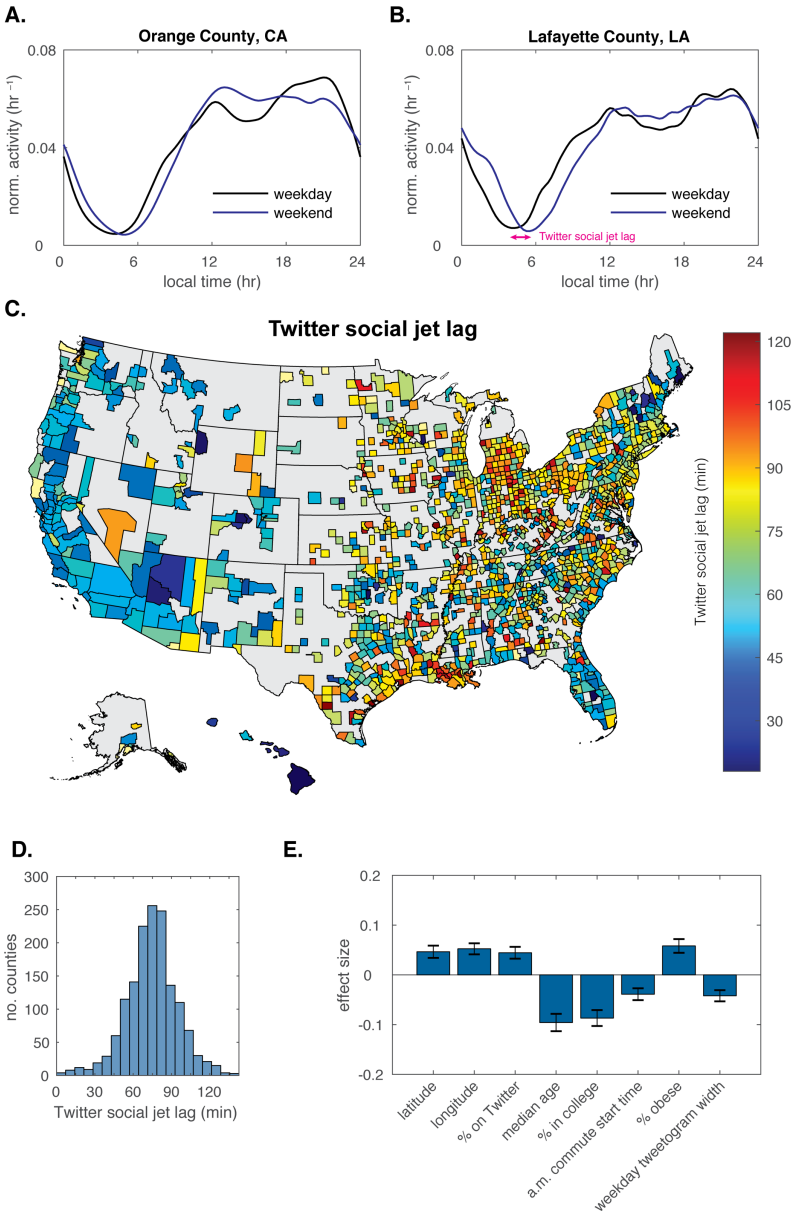

Figure 3.2. Twitter social jet lag.
(**A-B**) Average weekday and weekend tweetograms for Orange County, CA, and Lafayette County, LA. Twitter social jet lag is defined as the time delay that maximizes the cross correlation between the troughs of the weekday and weekend tweetograms. All averages are taken over 2012-2013 using only February, March April, and October in this Figure to minimize the effect of holidays.
(**C**) Map of US counties colored by the magnitude of Twitter social jet lag. Grey regions represent counties missing from the dataset and outliers (n=8). Color limits are set to the 1st and 99th percentiles of the data.
(**D**) Distribution of Twitter social jet lag across US counties.

(Figure 3.2 continued) (**E**) Effect sizes of demographic predictors with statistically-significant nonzero coefficients in a linear model of social jet lag (R^2_{adj}=0.21, p-value < 1e-61). The model included 21 predictors taken from US Census and publicly available databases, including geographic, sex, age, race, employment, commuting characteristics, educational attainment, population level, political leaning and health metrics. See Table S3.3 for detailed descriptions, effect sizes and p-values for all covariates. Effect size of 1 means that an increase in the predictor value by 1 z-score leads to a 1-hr increase in Twitter social jet lag. Coefficient p-values were controlled at a 0.1 family-wise error rate (FWER) using the Bonferroni correction.

The magnitudes of Twitter social jet lag across US counties correlate with geographic, socioeconomic, and health indicators

We calculated the average magnitude of Twitter social jet lag for all US counties in our dataset (Figure 3.2C-D). Twitter social jet lag has a unimodal distribution, with the average county experiencing about 75 min of social jet lag (Figure 3.2D), a value in good agreement with the average social lag measured in Germany using sleep surveys [22]. However, different parts of the United States show substantial variation, with counties in Central and Eastern regions experiencing higher levels of Twitter social jet lag compared to those in the along the West Coast (Figure 2C).

We sought to understand if social and cultural factors exert additional pressures on social jet lag independently of geography. First, we compiled a set of 130 descriptors capturing geographic, demographic, socioeconomic, health and religious characteristics of US counties (Table S3.4). One-way correlations of these predictors with Twitter social jet lag allowed us to estimate the importance of different categories of descriptors, and suggested the most predictive descriptor within each category, e.g. commuting patterns are more strongly correlated with Twitter social jet lag than employment characteristics (Figure S3.2A). To obtain a qualitative picture of the importance of individual predictors while accounting for the interplay between them, we sought to combine the most salient descriptors into a single model. We manually

selected a subset of 21 descriptors to include in a linear model of the magnitude of Twitter social jet lag (Figure 3.2E-F, Figure S3.2). Descriptors were included in the model on the basis of correlation with social jet lag in our calculations or in previous reports [18,22], if they captured basic demographic trends (age, race, income, etc.), or if they represented previously unstudied population characteristics which we hypothesized could influence social jet lag (e.g., proportion of students) (Table S3.3).

We found a significant association (family-wise error rate < 0.1) in the linear model between Twitter social jet lag and eight predictors describing geographic, demographic and Twitter usage characteristics of US counties. The magnitude of Twitter social jet lag correlates with latitude and longitude, supporting the qualitative picture in Figure 3.2C that Twitter social jet lag is lowest on the West Coast and increases towards the East of the US. Counties with older populations, greater proportions of students, and later commute times experience lower Twitter social jet lag, perhaps because these populations have more flexibility to set their weekday schedules. Twitter social jet lag also correlates with the incidence of obesity, in agreement with previous findings [22], and with narrower tweetogram troughs on weekdays, suggesting that sleep debt may influence Twitter social jet lag in our sample (Figure 3.2E). Together, these findings suggest that the variation in Twitter social jet lag across the United States is due to both geographic and demographic factors.

Seasonal variation in social jet lag largely reflects changes in weekday tweeting rhythms

Since the concept of social jet lag was first defined over a decade ago [10], most studies have surveyed social jet lag without regard to time of year. In many animal species, seasonal

variation in the environment is linked to dramatic annual changes in behavior including altered fertility, and metabolism [40,41]. For humans, external pressures on activity schedules, such as work and school times, can also exhibit seasonal variation. We therefore asked if social jet lag varies across the calendar year. The answer to this question is important because it may uncover factors that mitigate social jet lag magnitude. Because our database of Twitter activity rhythms spans two calendar years, our dataset affords an opportunity to examine seasonal variation in social jet lag.

We found that the times of tweetogram troughs, particularly on weekdays, vary substantially from season to season in many counties. For an example of a location with high seasonal variability, consider Wayne County, MI (Figure 3.3A-C), where the time of minimum Twitter activity on weekdays varies from ≈4:25 a.m. in February-May to ≈5:35 a.m. in July and August; patterns of weekend activity are less variable, but nonetheless become ≈45 min earlier in the spring than in the summer. As a result, social jet lag also exhibits pronounced seasonal variation: weekend and weekday schedules are misaligned by almost 90 min in February-March and September-October but are only separated by 30 min in July-August (Figure 3.3D).

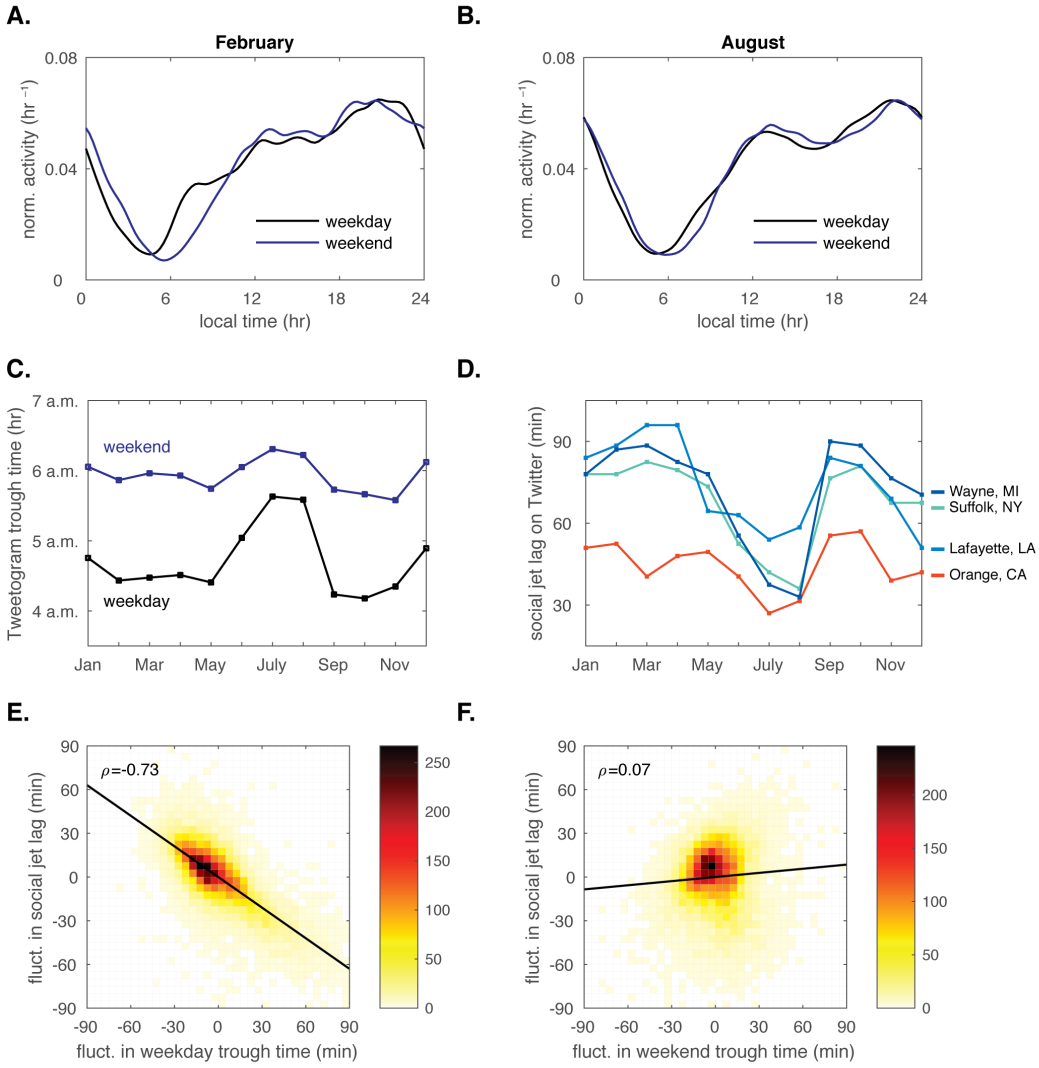

Figure 3.3. Seasonal variation in the magnitude of Twitter social jet lag.
(A-B) Sample tweetograms for Wayne County, MI, calculated for the average weekday and weekend in February and August of 2012-2013.
(C) Seasonal changes in the position of tweetogram troughs on weekdays and weekends averaged monthly in 2012 and 2013 for Wayne County, MI.
(D) Seasonal changes in Twitter social jet lag in 2012-2013 in Wayne County, MI, and three other US counties shown in Figure 1D.
(E-F) Two-dimensional histograms showing the relationships between seasonal fluctuations in Twitter social jet lag and seasonal fluctuations in the tweetogram trough positions on weekdays and weekends for all counties in the dataset. Fluctuations were calculated as the monthly deviations from the annual mean. Pearson correlation coefficients (ρ) are displayed in top left corners of the histograms: (E) ρ=-0.73, p-value<3e-16; (F) ρ=0.07, p-value<5e-14. Counties with greater than 30 daily users on average were used for this analysis (n=943).

Though monthly social jet lag curves in different counties show substantial variability in magnitude, the broad pattern of lowest social jet lag in the summer with a maximum in late winter or early autumn is general (Figure 3.3D). Furthermore, because Twitter activity patterns on weekdays generally show higher seasonal variability than on weekends, seasonal variation in Twitter social jet lag is primarily due to variability in weekday tweeting rhythms (Figure 3.3E-F).

Patterns of seasonal variation in social jet lag are associated with distinct geographic and demographic characteristics

To identify counties with similar patterns of seasonal variation, we subtracted the mean from each monthly social jet lag curve and then clustered the resulting residual curves (Figure 3.4A). We analyzed the 943 counties with over 30 average daily users. Counties separated into three major clusters, which differ both in the seasonal amplitude of Twitter social jet lag and the month of the year when it reaches its minimum (Figure 3.4A,C). Counties in the first (red) cluster bear similar levels of social jet lag year-round (53 min average amplitude, i.e., the difference between maximum and minimum social jet lag over the year), whereas the other two clusters experience significantly more seasonal variability (72 and 87 min average amplitudes in clusters 2 and 3). The second (green) and third (blue) clusters are set apart by the timing of the summer dip in Twitter social jet lag, which occurs in June-July in the third (blue) cluster and in July-August in the second (green) group of counties.

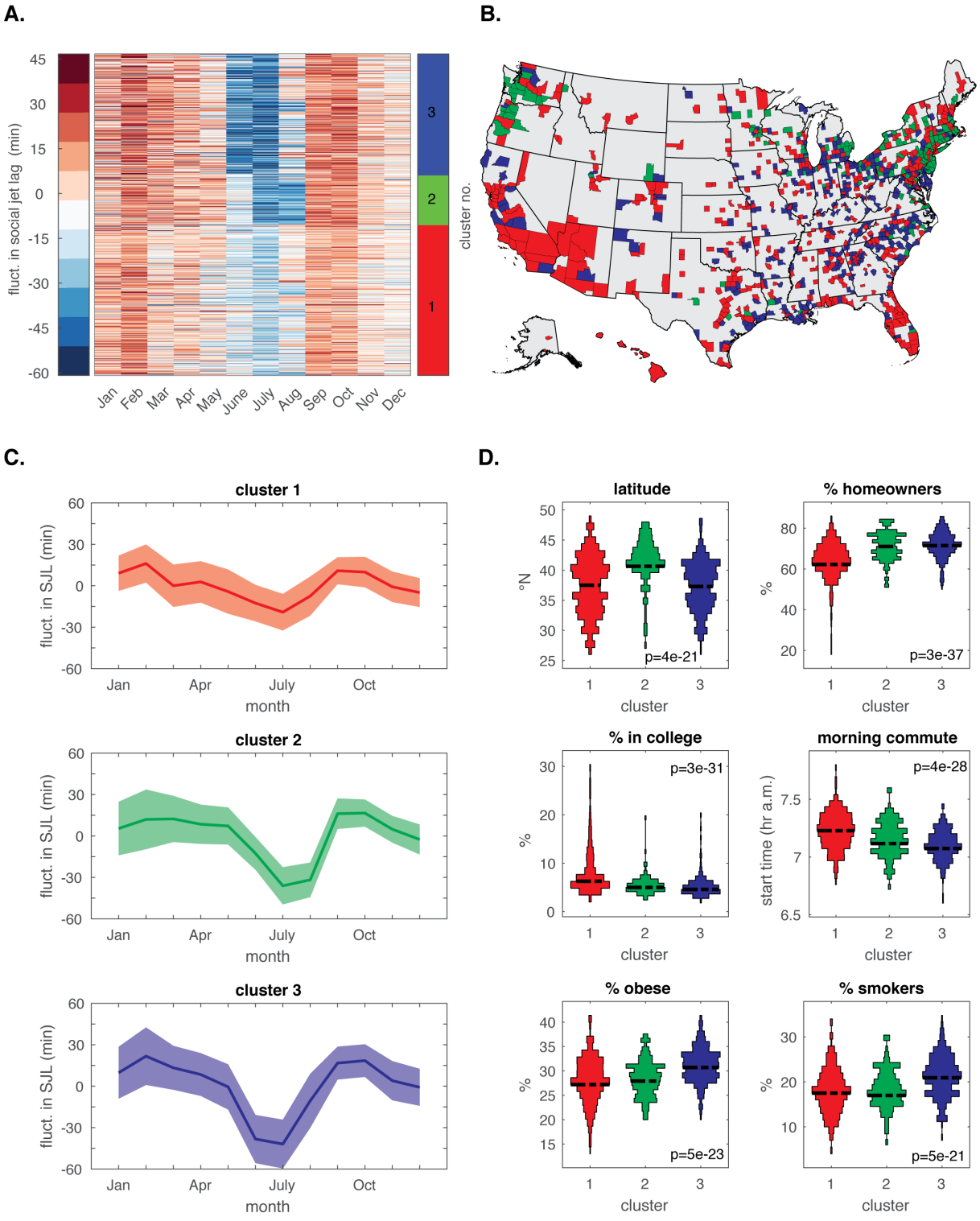

Figure 3.4. Seasonal patterns of Twitter social jet lag cluster US counties into groups with distinct geographic and socioeconomic characteristics.

(Figure 3.4 continued) (A) Agglomerative clustering of mean-subtracted monthly social jet lag curves reveals three clusters with distinct seasonal patterns of Twitter social jet lag. Each row of the heat map represents seasonal fluctuations in social jet lag from one county as in Figure 3D. Heat map color limits are set to the 1st and 99th percentiles of the data. Cluster assignments are indicated in the color bar on the right. Only those counties which had over 30 daily users in 2012-2013 on average were used for this analysis (n=943).
(B) Map of US counties colored according to their cluster assignment in (A). Grey areas indicate counties missing from the dataset, counties with fewer than 30 daily users in 2012-2013 on average or outliers (n=10 outliers).
(C) Seasonal changes in Twitter social jet lag by cluster. Seasonal fluctuations in Twitter social jet lag averaged across all counties in each cluster (solid lines) overlaid with shaded areas indicating the mean ± one standard deviation of the values. Clusters are colored as in (A).
(D) Distributions of demographic predictors within counties grouped according to their cluster assignments in (A). These six predictors had the most significantly different distributions between the clusters out of the 21 predictors studied (as in Figure 2E). Statistical differences in the distributions between clusters were evaluated using the three-way Kruskall-Wallis test (controlled at FWER < 0.05, p-values listed on charts). See Table S1 for detailed description of the covariates.

These cluster assignments appear to map onto coherent geographic regions (Figure 3.4B). The first (red) cluster covers much of the Southwest of the US, Hawaii, and Florida, in addition to urban centers elsewhere in the US. The second (green) cluster predominantly consists of counties in the North and Northeast of the US (Figure 3.4D), whereas the third (blue) cluster appears frequently in the Rust Belt and the South. Counties in Central United States appear mixed between the first (red) and third (blue) clusters, though the latter is enriched for counties further West in their time zones (Figure S3.3).

Do patterns of seasonal changes in social jet lag group counties into clusters with distinct demographic features? To address this question, we performed a statistical analysis to identify socioeconomic parameters that are enriched or depleted in different clusters (Figure S3.3). Intriguingly, the first (red) and third (blue) clusters exhibit opposite trends in several categories of demographic descriptors. Consider the population and political characteristics: whereas the first (red) cluster is enriched in counties with high population, urban status and a tendency to

vote Democratic, the third (blue) cluster is depleted for these descriptors (Figure S3.3). These two clusters also exhibit opposite trends in commuting, occupational, health and educational descriptors (Figure S3.3). These signatures are also evident in the distributions of the socioeconomic predictors: among the three clusters, the first (red) cluster has the latest distribution of commuting patterns, largest prevalence of college students, and lowest incidence of smoking and obesity, whereas counties in the third (blue) cluster exhibit contrasting trends (Figure 3.4D).

Weekday tweeting schedules are shifted later in the day during federal and school holidays

One of the most striking conclusions from the clustering analysis in Figure 3.4A,C is that nearly all counties experience a drop in Twitter social jet lag during the summer. One common reason for a change of schedule during summer months is the school holiday. We reasoned that if individuals and families tied to the school schedule set their weekday alarm clocks later during the summer than the school the year, this could lead to a large change in Twitter social jet lag.

To test this proposal, we examined weekday Twitter activity in select US counties with unified public school calendars (Figure 3.5A). When we marked the dates of important holidays alongside changes in the timing of Twitter activity, we observed that weekday tweeting schedules are consistently shifted 1-2 hours later in the day during summer, spring and winter school holidays (Figure 3.5B-D). Troughs of weekday Twitter activity schedules are also timed later when weekdays coincide with major public holidays, leading to “spikes” on Thanksgiving, Memorial Day, and Columbus Day (Figure 3.5B-D).

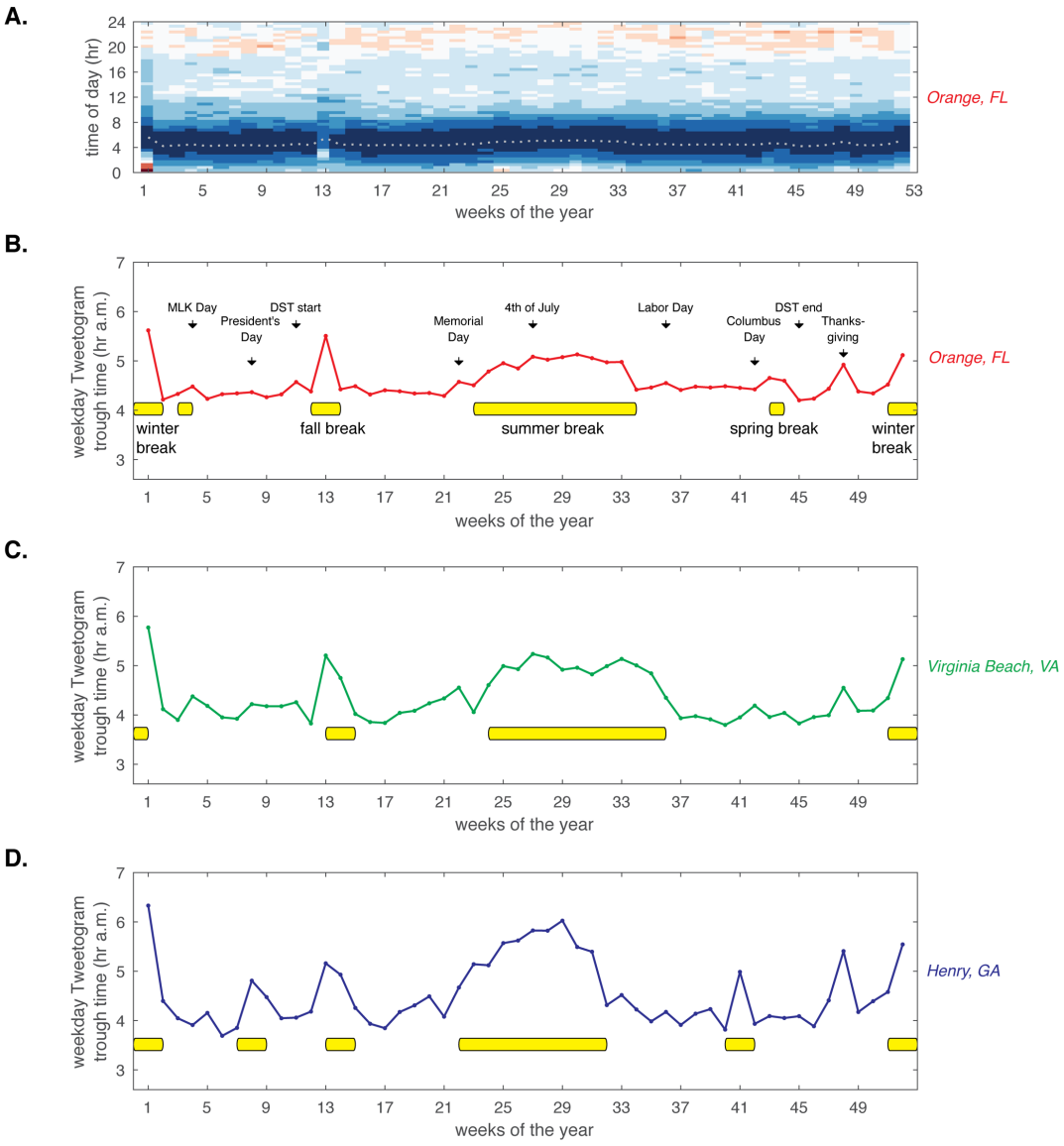

Figure 3.5. Seasonal changes in weekday Twitter activity patterns follow the K-12 school calendar and major holidays.

(A) Heat map representation of weekly tweetograms for Orange County, FL, showing averaged weekday Twitter activity profiles for each full week of 2013. Colors indicate probability of tweeting (blue = low probability, red = high). Dotted grey line marks the positions of tweetogram troughs. Week 1 is defined as the full week when January 1 occurs (Dec. 31, 2012 – Jan. 6, 2013).

(B-D) Seasonal variation in weekday tweetogram trough positions calculated for every full week of 2013 for three US counties from different clusters in Figure 3.4. Yellow bands beneath each curve mark the start and end dates of major school holidays (longer than one day off) observed by the public schools in the respective county in 2013. Arrows above the curve mark major US holidays in 2013, as well as the start and end of daylight savings time (DST).

Evidently, the holiday calendar plays an important role in setting the timing of weekday Twitter usage. Notably, counties belonging to the second (green) cluster, which generally experience a drop in social jet lag later in the summer compared to other clusters, are predominantly in the North and Northeast of the US (Figure 3.4B, Figure S3.3), where schools conventionally have holiday breaks from late June to early September, as opposed to many communities in the South which traditionally end the school year earlier [42]. Though the school calendar appears predictive of the timing of the summer shift in Twitter activity, the magnitude of this shift varies among counties. We discuss possible reasons in the Discussion in the context of the age distribution of Twitter users.

Seasonal variation in Twitter activity rhythms is primarily determined by social schedules

The pronounced effect of federal and school holidays on the Twitter social jet lag does not exclude the possibility that Twitter activity is also affected by the daily pattern of dawn and dusk, as has been suggested in the literature [43]. One way to address this question is to study how rhythms of tweeting change with the seasons. If patterns of tweeting are primarily influenced by the sun, then the timing of Twitter activity might remain aligned to dawn or dusk as their schedules change from season to season. On the other hand, if tweeting schedules follow local (i.e., socially defined) time, we would expect little seasonal variation in the timing of Twitter activity.

To discriminate between these two scenarios, we plotted the times of tweetogram troughs for weekdays and weekends, as well as the average times of dawn and dusk over each month throughout the 2013 calendar year (Figure S3.4, Figure 3.6). To quantify the preference of

Twitter rhythms to align to dawn, dusk or social cues, we computed how the time of minimum Twitter activity scales with day length in a linear model of clock-environment coupling (Figure 3.6). In this model, the slope of the scaling relationship describes whether Twitter activity patterns preferentially align to social time (e.g., 9 a.m.; m=0), sunrise ($m \approx -0.4$) or sunset ($m \approx 0.6$) (Figure 3.6A-C). By separately analyzing seasonal influences on weekend and weekday tweeting, we can quantify how the timing of sunrise and sunset affects the timing of Twitter activity both on work days and days with reduced social obligations.

The weekend distribution of m is centered around 0, which indicates that Twitter schedules on Saturdays and Sundays align to local (i.e., social) time more closely than to the solar schedules (Figure 3.6C). Tweeting rhythms on weekdays exhibit more seasonal variation and appear to be influenced by changes in sunset times, particularly at longer day lengths (Figure 3.6C, Figure S3.4). However, this apparent dusk-tracking behavior is likely confounded by the effects of student holidays, discussed in the previous section (Figure S3.4). When holiday months are removed from the analysis, the weekday distribution of m is instead centered near 0, much like the weekend distribution (Figure 3.6D-F).

Though there are some counties at the extremes of the distributions in Figure 3.6C where Twitter activity tracks sunrise or sunset quite closely throughout the year, our calculations suggest that for the majority of US counties the rhythms in Twitter use are more strongly affected by the social schedule. Yet even in these counties where social pressures appear to dominate, as in Suffolk County, NY, traces of dawn-tracking (in shorter winter months) and dusk-tracking (in the height of the summer) behavior may be present on weekends (Figure S3.4C).

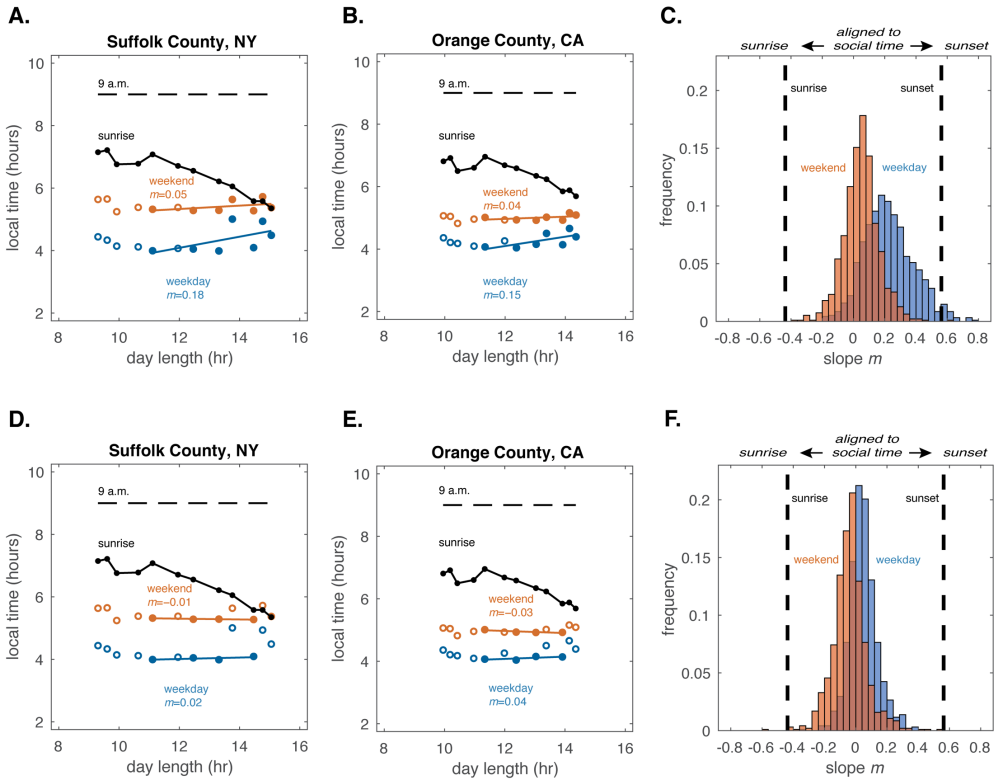

Figure 3.6. Seasonal changes in Twitter activity reflect social schedules.
(A-B) Monthly changes in the positions of weekend and weekday tweetogram troughs (orange and blue markers) in Suffolk County, NY, and Orange County, CA, plotted against day length. Slopes *m* of the linear fits (orange and blue lines) were determined by linear regression to data from months when daylight savings time (DST) was in effect (filled markers). Black dashed lines indicate average sunrise times calculated on a per month basis. Day length is defined as time between sunrise and sunset, when the sun is 0.833 degrees below the horizon.
(C) Distribution of day length vs. trough time slopes *m* for weekends (blue bars) and weekdays (orange bars) for counties in the dataset which had over 30 daily users in 2012-2013 on average (n=943). Slopes calculated as in (A-B) indicate whether the seasonal changes in the positions of tweetogram troughs tend to align more closely to social time cues (e.g., 9 a.m.) or solar time cues (e.g., sunrise or sunset). The dotted lines mark the slopes with which the local times at sunrise and sunset scale with day length; median slopes among all counties are shown.
(D-E) Data in (A-B) replotted, with linear fits shown to data from April, May, September and October, months of the year when public US schools were generally in session and DST was in effect.
(F) Distribution of day length vs. trough time slopes *m* for weekends (blue bars) and weekdays (orange bars) for all counties in the dataset calculated for data from April, May, September and October. Slopes calculated as in (D-E) indicate whether the seasonal changes in the positions of tweetogram troughs tend to align more closely to social time cues (e.g., 9 a.m.) or solar time cues (e.g., sunrise or sunset). The dotted lines mark the slopes with which the local times at sunrise and sunset scale with day length, as in (C).

DISCUSSION

In this study, we sought to obtain a geographically resolved, quantitative portrait of human activity rhythms. We asked whether Twitter activity patterns across the US are predominantly affected by social or solar factors, and whether differences between weekdays and weekends vary seasonally. To this end, we analyzed a large dataset of daily Twitter activity profiles averaged over many users. While these activity profiles have a characteristic shape, reaching maximal levels in the afternoon or late evening and lowest levels at night, a striking conclusion from our analysis is that there is broad diversity in the timing of Twitter activity across the United States that is correlated with geography. In this sense, different regions of the country are separated not only by space and culture, but also by their use of time. Indeed, these factors seem to be interdependent. Patterns of seasonal variability in Twitter activity rhythms, for example, organize US counties into clusters with distinct demographic, educational, socioeconomic and political characteristics (Figure 3.4).

The temporal axis of human behavior appears to influence human health [2], for example when patterns of activity on weekends are shifted later in the day compared to weekdays. We found that this phenomenon, known as social jet lag [22,33], is prevalent on Twitter. The magnitude of Twitter social jet lag generally increases from the Southwest to the Northeast of the United States. Particularly for those regions with larger overall Twitter social jet lag, there is a strong seasonal effect, with a marked decrease in social jet lag during the summer. Interestingly, this decrease derives primarily from seasonal changes in weekday schedules, which in turn appear to be strongly affected by holiday schedules, particularly in the school calendar. Data on

individual counties and statistical analyses of the full dataset both suggest that social factors exert a larger influence on Twitter activity patterns than do seasonal changes in day length.

Our results complement earlier efforts that used surveys to determine whether the timing of sleep wake-schedules follows sunrise, both seasonally and from East to West, in European populations [43–45]. Among German respondents, the mid-sleep point tends to align to seasonal changes in sunrise from late autumn to early spring, but not during the summer or when daylight savings time (DST) is in effect [43]. And in Estonia, sleep schedules display little variation year-round [45]. These observations are in line with the diversity of seasonal tracking behavior we observe across US counties, some of which may exhibit traces of dawn-tracking behavior in late autumn, but generally show little seasonal variability in the timing of Twitter activity during DST. It has been proposed that weakened responses of modern sleeping schedules to the rising and setting of the sun are consequences of spending little time exposed to natural light, particularly in more urbanized environments [4,44]. In this regard, one possible explanation for our findings is that the population of Twitter users consists largely of people who spend little time outdoors and structure their lives irrespective of when the sun rises and sets, but in accord with social obligations such as work and school.

The effects of the school calendar that we observe are much more pronounced in certain counties. One explanation could be that students comprise a large proportion of Twitter users in those counties and thus dominate the activity. However, according to the Pew Research Center, the prevalence of Twitter usage is comparable between teenagers, 18-29 year olds, and 30-49 year olds, with approximately 30% of US population from each age category using the social media platform [46,47]. Thus, we instead favor the possibility that school schedules influence the

activity schedules of a much larger portion of society (e.g., parents, caretakers, educators, and other school employees), and that the large differences we observe in the magnitude of seasonal Twitter social jet lag between counties reflect demographic differences in these categories.

Social jet lag has been previously found to associate with several disease indicators, including obesity and depression [18,22]. We also find that the incidence of obesity is associated with the magnitude of Twitter social jet lag. It would be interesting to extend this analysis to individual users to determine activity patterns that are most strongly associated with disease vs. healthy states in users living in similar environments. For instance, such findings could aid the development of school schedules appropriately timed relative to adolescent sleeping patterns as well as work schedules matched to individuals' circadian rhythms, helping to optimize performance in an increasingly "round-the-clock" work culture.

As portable health monitors and activity trackers become more widespread, so will real-world measurements linking the temporal structure of our daily lives with health and disease. Based on such epidemiological correlations, researchers will be able to design experiments probing the connection between circadian rhythms and illness, and incorporate circadian timing into diagnosis and treatment options [26]. Social jet lag is one of the first conditions to be studied in this way.

METHODS

Overview of methodology

Starting from a raw dataset containing the timestamps, locations, and user IDs of tweets sent between 2012 and 2013, we calculated county-level average Twitter activity profiles (i.e., tweetograms). Each tweetogram represents the probability distribution of tweeting throughout an average 24-hr day in a given county over a particular time period of interest (e.g., weekday activity profile in February). All tweetograms exhibit pronounced troughs (i.e., periods of low activity at night) and we studied how the timing of troughs differed county to county, and month to month. We defined Twitter social jet lag as the shift between tweetogram troughs on weekdays and weekends and performed statistical analyses to relate the magnitude of this shift to various demographic descriptors of US counties. We also studied how Twitter social jet lag changes monthly, compared the seasonal fluctuations in Twitter social jet lag among US counties using a clustering analysis, and compared the distributions of various demographic descriptors among the resulting clusters using the Kruskal-Wallis test. Finally, we studied how the timing of tweetogram troughs changes seasonally in a model where the timing of tweetogram troughs depends linearly on day length. The following sections describe our data collection, processing, and analysis steps in detail.

Generating Tweetograms from Raw Data

The basic unit of analysis in this study is a tweetogram, an anonymized measure of Twitter activity in a county over a 24-hr time period, averaged over all days of interest and for all users in each county. To calculate tweetograms from the master dataset containing the

timestamps, user IDs and geolocations of tweets, we assigned tweets to US counties, normalized daily tweet counts for each user, and binned tweet counts into 15-min intervals. Finally, binned activity profiles in each county were averaged across specific days of interest, with each day contributing equally to the average. Individual steps are described in detail below.

The master dataset contains all public tweets with publicly listed geolocation metadata that were sent from Jan. 1, 2011 to June 30, 2014 by users in the United States. We used the timestamps and geolocation metadata of the tweets in the analysis. Twitter IDs were used only to normalize activity levels among different users, as described below, and to remove counties with a median number of unique daily users below 10 over the timespan of the dataset. The dataset did not contain any text, data, or other metadata from the tweets. Detailed descriptions of criteria used to select data for specific figures in the main text and criteria used to reject outliers are provided in the tables at the end of this section.

On each calendar day, each user was assigned to a given US county based on the geolocation of the first tweet that user sent that day. Tweet counts were binned into 15-min intervals and each user's daily activity was then normalized to unit weight (Figure 3.1A). For example, if a user sent 5 tweets on January 1, 2013, then each tweet contributes 0.2 units to the 15-min bin when it was sent. This first normalization step gives equal weight to all users on any given day and helps ensure that the results are not biased by a small number of highly-active users.

Each county's daily activity was then normalized to unit weight. This second normalization step is necessary to avoid biases due to days with unusually high Twitter activity.

Symbolically, if a county has N Twitter users on a given day, and if $f_i(t)$ is the number of tweets from user i during time bin t, then the normalized activity is given by:

$$A(t) = \frac{1}{N}\sum_i \frac{f_i(t)}{\sum_\tau f_i(\tau)}$$

Twitter activity timeseries were then averaged across different days over the time periods of interest (e.g., across all days of 2012-2013, or separately by month of the year and by weekdays and weekends), i.e. averaging $A(t)$ above. The resulting curves are tweetograms. For downstream analysis and visualization purposes, tweetograms were smoothed with a 150-min Gaussian kernel.

The table below lists the data that were included in the tweetogram calculations in different figures.

Figure	Description of tweetogram	Criteria for aggregating days	Criteria for separating days	Weekdays and weekends separate?	Timespan
1	average day over 2012-2013	all days	--	no	2012-2013
2	average weekend and weekday over Feb.-Apr., Oct	all days from Feb.-Apr., Oct. 2012-2013	--	yes	2012-2013
3, 4, 6	average weekend and weekday for each calendar month	2012-2013	monthly	yes	2012-2013
5	average weekday for every week of 2013	all weekdays	weekly	weekdays only	2013

Table S3.1. Data included in tweetogram calculations.

In Figure 3.2, we specifically disregarded months when major holidays in the work and school calendar occur. Thus, we excluded May-September due to summer holidays, and November-January due to Thanksgiving, Christmas and winter holidays.

The following table lists which counties were excluded from analysis in different figures.

Figure	Description of tweetogram	Criteria for exclusion of outliers	Total number of counties analyzed
3.1, S3.1	average day over 2012-2013	all counties included	1521
3.2, S3.2	average weekend and weekday over Feb.-Apr., Oct	• 3.2C: If social jet lag for a given county is >3× standard deviations away from the mean value among all counties • 3.2D-E, S3.2: in addition to the criteria for C, if not all demographic descriptors available for this county	• 3.2C: 1513 • 3.2D-E, S3.2: 1429
3.3, 3.4A-C, 3.6	average weekend and weekday for each calendar month	• If the number of average daily users in this county is <30 (568 counties excluded) or • If standard deviation of the monthly social jet lag curve >1 hr (10 additional outliers)	943
3.4D, S3.3	average weekend and weekday for each calendar month	• In addition to the criteria for 4A-C, if not all demographic descriptors were available for this county	874

Table S3.2. Criteria for exclusion of outliers.

Characterization of Tweetogram Troughs

To calculate the width of a given tweetogram trough (Figure 3.1B), we calculated the horizontal distance between trough edges at the tweetogram value corresponding to 25% of the median height among all tweetograms in the dataset (see dotted line in Figure 3.1B,D); here, the height refers to the maximum value of the smoothed, interpolated tweetogram. We found this strategy was more robust than calculating the width of each tweetogram at its own quarter-height position, but the two approaches were in good agreement with each other. We found that computing tweetogram widths at this 25%-height level avoided artifacts arising from variability in tweetogram structures at the maximum and at the bottom of the trough.

Calculation of Twitter Social Jet Lag

In prior work, social jet lag has typically been defined as the difference between the midpoints of nighttime sleep on weekends and weekdays, based on surveys asking respondents when they go to sleep and wake up [10]. Because we do not have access to individual users' data, we defined Twitter social jet lag as the temporal shift between county-level weekday and weekend nighttime Twitter activity patterns.

Mathematically, we defined Twitter social jet lag as the time delay between weekend and weekday tweetograms that maximizes the cross-correlation between the troughs of the curves after they were smoothed and linearly interpolated in 1.5-min intervals. To calculate this value, we computed the Pearson correlation coefficients between the 2 a.m. – 10 a.m. portion of the weekend tweetogram and the corresponding interval on the weekday tweetogram, as the latter was temporally shifted in 1.5-min intervals up to a maximum delay (τ) of ±4 hours. The time delay leading to the maximum correlation coefficient was defined as Twitter social jet lag (*tSJL*). In an equation:

$$tSJL = \underset{-4<\tau<4}{\operatorname{argmax}}\, \rho(wkend(2\text{am}, 10\text{am}), wkday(2\text{am} - \tau, 10\text{am} - \tau)) \,,$$

where *wkend(t1,t2)* refers to the vector of weekend tweetogram values for $t1 < t < t2$, *wkday(t1,t2)* refers to the respective portion of the weekday tweetogram, and $\rho(x,y)$ is the Pearson correlation coefficient.

We compared this choice with a simpler metric, the difference in the positions of weekend and weekday tweetogram troughs. Trough positions were estimated by fitting parabolas within ±3 hours of the minima of the smoothed, interpolated tweetograms. We reasoned that this second metric based on trough tweetogram positions approximated the difference in mid-sleep

positions on weekends and weekdays, the traditional definition of social jet lag. We found that the two metrics were in good agreement with each other (Pearson ρ=0.91, p-value < 4e-15, for calculations in Figure 3.4), but we favor the cross-correlation metric because it is nonparametric and does not assume that the troughs are parabolic.

Agglomerative clustering analysis

To identify patterns of seasonal fluctuation in Twitter social jet lag that were common among US counties, we performed a clustering analysis. To focus on differences in seasonal variability between counties, as opposed to the mean level of Twitter social jet lag, we first subtracted the annual average from each county's monthly social jet lag values and used the residual seasonal fluctuations for clustering (Figure 3.4). Agglomerative clustering was performed using the built-in clusterdata() function in MATLAB 2017b (MathWorks, Inc.), using Euclidean distance to compare mean-subtracted monthly social jet lag curves and Ward's linkage to compare clusters with each other. The choice to cut the hierarchical cluster tree at the level that produced three clusters was made empirically. If counties were subdivided into fewer clusters, we found noticeable inhomogeneity in at least one cluster by visual inspection of clustering results (e.g., heat map in Figure 3.4A). Selecting four or more clusters led to clusters without social jet lag patterns that were obviously different by visual inspection. The gap statistic [48] calculated using the MATLAB evalclusters() function for 1-10 clusters confirmed our choice.

Calculations of day length tracking behavior

To understand whether the timing of Twitter activity onset follows the seasonal changes in the time of sunrise throughout the year or remains aligned to local time, we calculated the linear dependence of the positions of tweetogram troughs on day length. A slope of 0 indicates that the trough position remains aligned to local time and is unchanged throughout the year. A slope of approximately −0.4 suggests that the trough position changes seasonally in accord with changes in the timing of sunrise (e.g., getting earlier with longer days in the summer); by the same reasoning, a slope near 0.6 reflects dusk-tracking. Slopes in Figure 3.6 were calculated for each county by linear regression of monthly tweetogram trough times on day length. Tweetogram trough positions were estimated by fitting parabolas within ±3 hours of the minima of the smoothed, interpolated tweetograms. Day length was defined as time elapsed between sunrise and sunset, when the sun is 0.833 degrees below the horizon, averaged over all days for each calendar month. In Figure 3.6A-C, linear fits were performed only over months when daylight savings time was in effect (filled markers: April-October); in Figure 3.6D-F, fits were performed over months when school was in session and DST was in effect (filled markers: April, May, September, October). Monthly dawn times were defined as the local times at sunrise averaged over all days for each calendar month.

Demographic and other descriptors of US counties

To perform statistical analyses relating various population characteristics of US counties with the magnitude of Twitter social jet lag, its seasonal fluctuations, or properties of tweetogram troughs, we compiled a series of descriptors for each county.

Demographic, socioeconomic, commuting, health, and religion data were downloaded from the US Census Bureau and collections curated by Social Explorer, County Health Rankings and the Institute for Health Metrics and Evaluation (IHME) [49–56]. These databases aggregate information from multiple government and proprietary sources, such as US Census, Centers for Disease Control and Prevention, Centers for Medicare & Medicaid Services (CMS), and the Association of Religion Data Archives.

Specifically, data on county-level prevalence of sufficient sleep was obtained from the 2017 County Health Rankings dataset, which included sufficient sleep data from the 2014 Behavioral Risk Factor Surveillance Survey System run by the Centers of Disease Control and Prevention [36,49,57]. The CDC defines prevalence of sufficient sleep as the fraction of respondents reporting over 7 hours of sleep on average.

Astronomical variables were computed with the help of the Astral package in Python [58], which relies on solar calculations from NOAA [59]. Average precipitation and temperature readings were obtained from the North American Land Assimilation System (NLDAS) on CDC WONDER [60,61]. We included two further weather variables. The first weather variable was the number of "good-weather" days. Good-weather days were defined as those with at least 4 hours in a comfort zone based on standards developed in the building design literature [62,63]. This zone is defined as a four-point patch with vertices in temperature and humidity space. For temperature in Celsius (°C) and specific humidity in grams of vapor per kilogram of air, respectively, the four points are (18, 6.71), (27, 8.85), (27, 13.85), and (18,10). The second weather variable was the number of "bad-weather" days. Bad-weather days had at least 4 hours in an uncomfortable zone, defined as temperatures below –5 °C or above 35 °C. Good-weather

days and bad-weather days are not mutually exclusive; for each, the number of days in each county per year (averaged over 2003-2013) was included in the analyses.

Data on US election outcomes was downloaded from [64], which aggregated election results originally provided by The Guardian and TownHall.com [65,66].

Detailed definitions of data variables and data sources are provided in Table S3.4.

School calendars were downloaded from the websites of indicated school districts.

QUANTIFICATION AND STATISTICAL ANALYSIS

The number of data points used for statistical comparisons and criteria for exclusion of outliers are listed in the tables at the end of Methods section titled "Generating Tweetograms from Raw Data."

Linear Modeling and One-Way Correlation Analysis

We studied the relationship between Twitter social jet lag and roughly 130 characteristics of US counties (Table S3.4, Figure S3.2). In this analysis, we calculated average social jet lag only over the months of February-April and October to avoid the influence of school breaks and major holidays (as in Figure 3.2).

First, we performed an exploratory analysis, calculating the Pearson correlation coefficients between the magnitude of Twitter social jet lag and each of the covariates (Table S3.4, Figure S3.2). Dotted lines in Figure S3.2A mark the threshold for statistically significant non-zero Pearson correlation coefficients controlled at family-wise error rate (FWER) < 0.05 using the Bonferroni correction [67]. Though few variables individually explain more than 6% of

the variance in Twitter social jet lag, certain predictors appear more important than others (e.g., longitude correlates with extent of social jet lag more strongly than average precipitation). However, it is not possible to judge from the correlations with individual characteristics how much of the total variance in Twitter social jet lag can be explained by all of these predictors jointly because they are not independent.

To study the contributions of many predictors while taking into account the statistical relationships between them, we built a linear model that described Twitter social jet lag as a constant plus a weighted sum of predictors. The best-fit coefficient in front of a given predictor can be interpreted as the effect of the predictor on the response variable after accounting for the influences of all other predictors.

We focused on a subset of 21 predictors which were selected (i) if we hypothesized they may relate to social jet lag based on our findings (e.g., student population), (ii) if they represented basic demographic variables, or if (iii) they had been previously shown to correlate with social jet lag in a different population [10,22,68]. We excluded strongly correlated predictors (maximal pairwise Pearson $\rho \leq 0.7$ among 21 predictors). Based on these criteria, the following variables were selected (Table S3.3):

- basic demographic characteristics (population, the fraction of the population represented in our dataset daily on average, sex, age, race) or socioeconomics (employment, income, home ownership)
- commuting characteristics (average commute length and average morning commute start time)
- student population characteristics (fraction of population in high school and college)

- geographic coordinates (latitude, longitude)
- health predictors (smoking, obesity, diabetes, mental health, sleep)
- political leaning (Democratic voters in 2012 election)

We built the linear model using the fitlm() function in MATLAB. To evaluate the significance of the coefficients, we employed the Bonferroni p-value correction to control the family-wise error rate at 0.1. All eight statistically-significant coefficients are displayed in Figure 3.2E. The full model with 21 coefficients and a constant term had an $R^2_{adj} = 0.22$ (R^2=0.21, F statistic vs. constant model: 19.1, p-value < 1e-61); the reduced model, comprised of only the eight variables in Figure 3.2E plus a constant term, had an $R^2_{adj} = 0.20$ (R^2=0.20, F statistic vs. constant model: 45.6, p-value < 1e-64).

Cluster Enrichment Analysis

For the enrichment analysis in Figure 3.4, we used the nonparametric Kruskal-Wallis test to compare distributions of each socioeconomic predictor among the three clusters. We chose this test because many of the covariates had long-tail distributions. The Kruskal-Wallis test evaluates the hypothesis that the medians of the three distributions are identical.

For each predictor described in the previous section and each of the four clusters in Figure 3.4A, we performed the Kruskal-Wallis test comparing the distribution of this predictor for counties inside and outside the cluster. The corresponding p-values are plotted in Figure S3.3, where the dashed lines mark the Bonferroni-corrected p-value threshold controlling the family-wise error rate at 0.05.

SUPPLEMENTARY FIGURES AND TABLES

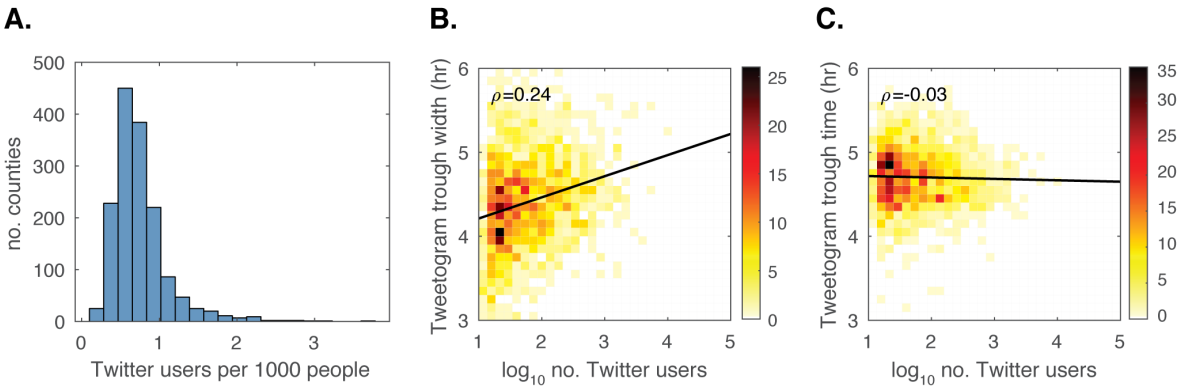

Figure S3.1. Twitter adoption rates for counties in our dataset.
(A) Distribution of Twitter adoption rates for counties in our dataset. For each county, the average number of unique daily users in our dataset was normalized by that county's population in the 2010 US Census.
(B) The widths of tweetogram troughs show a weak dependence on the size of Twitter user population.
(C) The positions of tweetogram troughs (in local time) are independent of the size of Twitter user population.
(B-C) Lines of best fit determined by linear regression. Pearson's correlation coefficients (ρ) listed in top left corners of the scatter plots: (B) ρ=0.24, p-value<3e-21; (C) ρ=-0.03, p-value=0.31.

A.

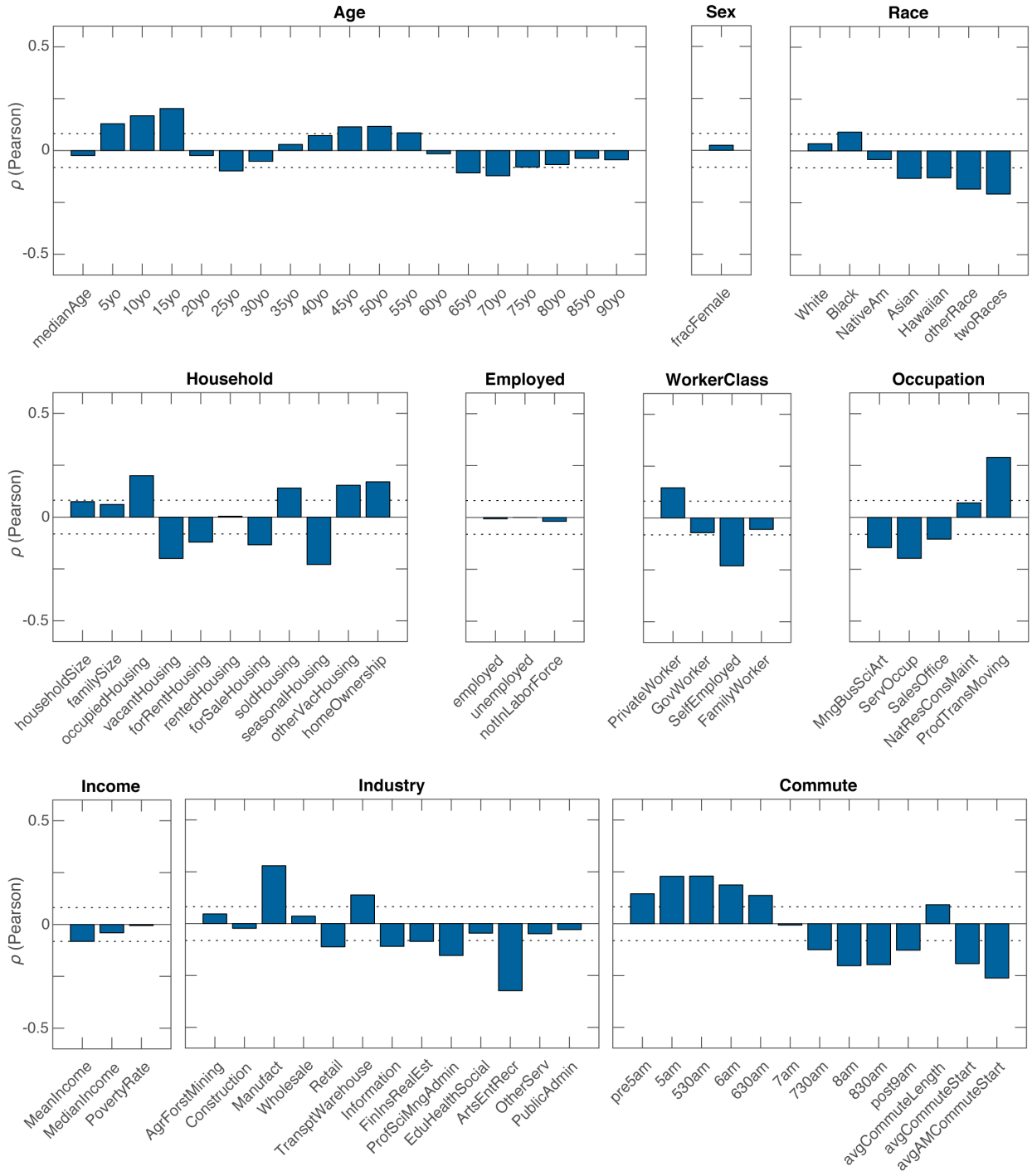

Figure S3.2A.

A (continued).

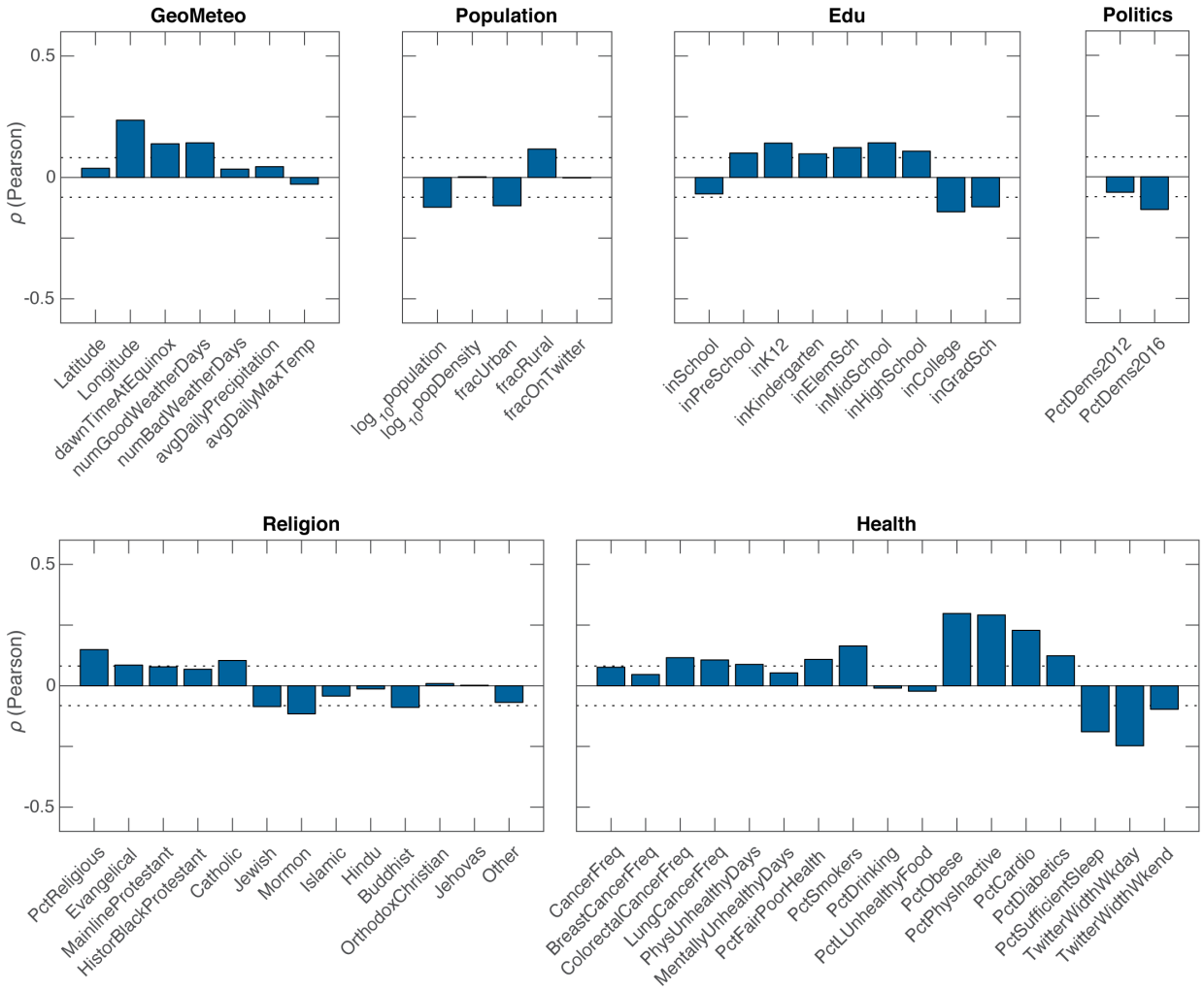

Figure S3.2A (continued).

B.

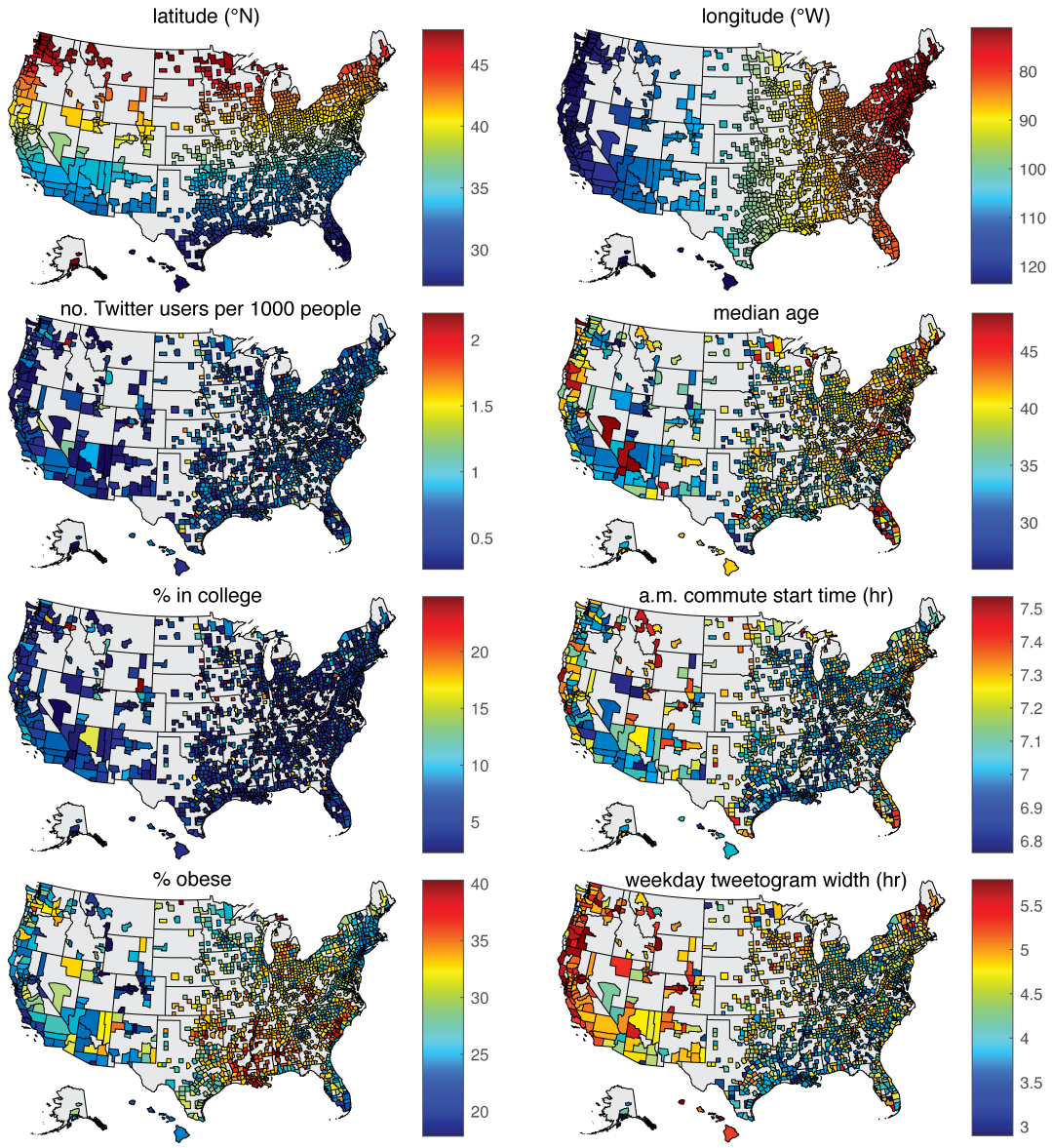

Figure S3.2. Correlations between descriptors of US counties and Twitter social jet lag.
(A) Pearson correlation coefficients between various socioeconomic, geographic and astronomical predictors and Twitter social jet lag. Dotted lines mark the threshold for statistically significant correlations controlled at family-wise error rate (FWER) < 0.05 using the Bonferroni correction. Twitter social jet lag was calculated as in Figure 3.2. See Table S3.4 for detailed descriptions of the socioeconomic predictors.
(B) Maps of US counties colored according to the magnitude of demographic predictors which are statistically associated with Twitter social jet lag (Figure 3.2E). Color limits are set to the 1st and 99th percentiles of the data.

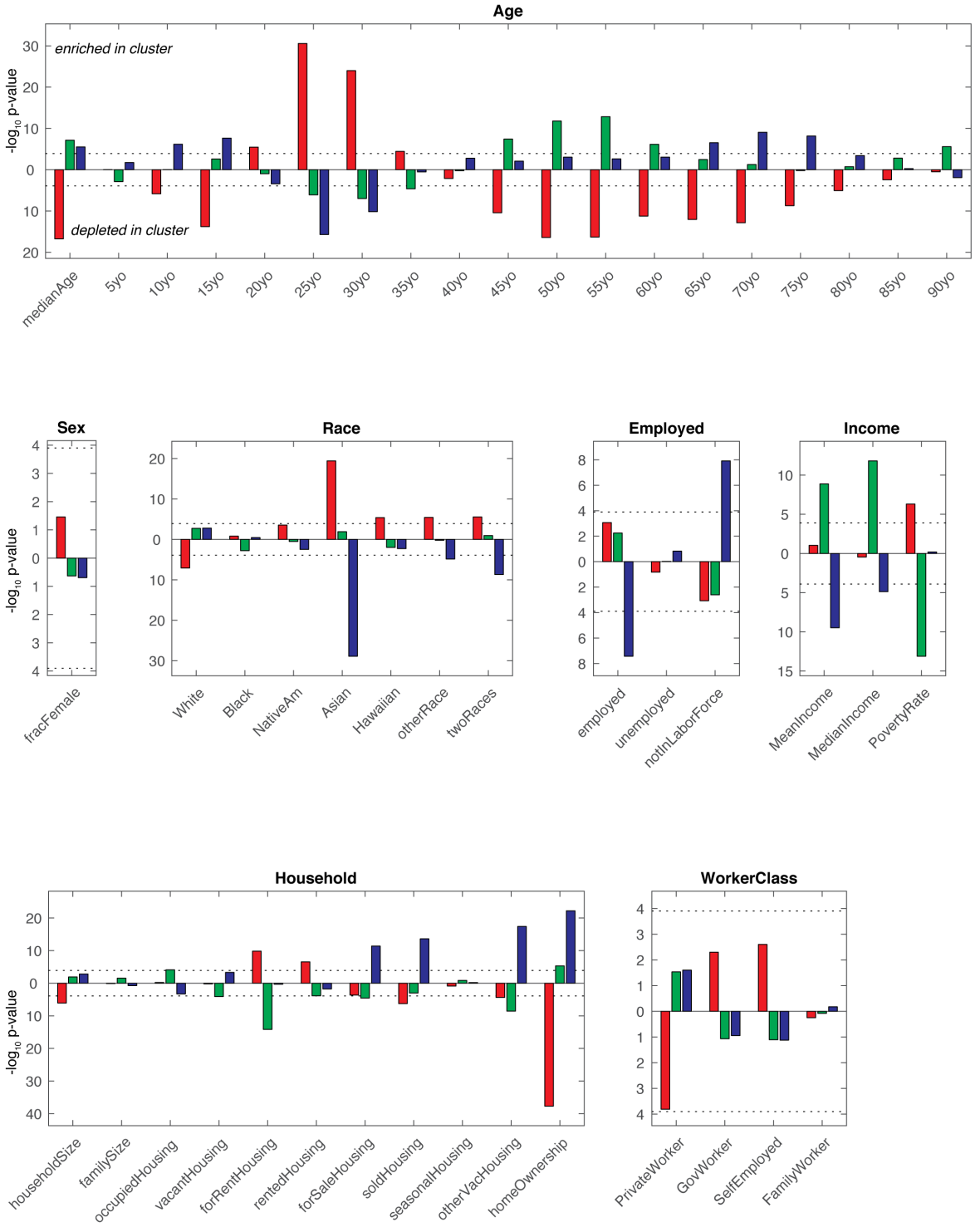
Age
enriched in cluster
depleted in cluster
-log10 p-value
medianAge
5yo
10yo
15yo
20yo
25yo
30yo
35yo
40yo
45yo
50yo
55yo
60yo
65yo
70yo
75yo
80yo
85yo
90yo
Sex
fracFemale
Race
White
Black
NativeAm
Asian
Hawaiian
otherRace
twoRaces
Employed
employed
unemployed
notInLaborForce
Income
MeanIncome
MedianIncome
PovertyRate
Household
householdSize
familySize
occupiedHousing
vacantHousing
forRentHousing
rentedHousing
forSaleHousing
soldHousing
seasonalHousing
otherVacHousing
homeOwnership
WorkerClass
PrivateWorker
GovWorker
SelfEmployed
FamilyWorker

Figure S3.3.

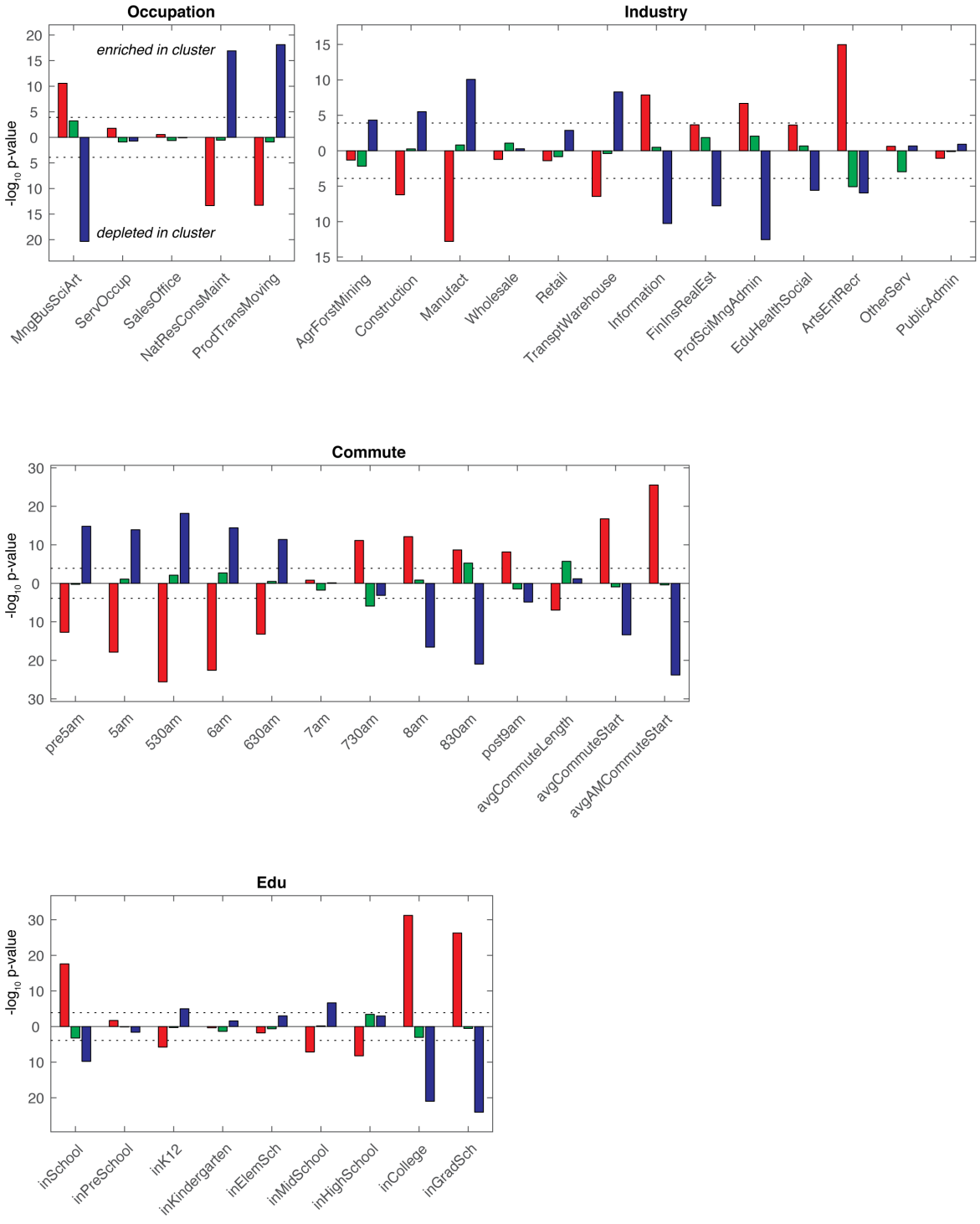

Figure S3.3 (continued).

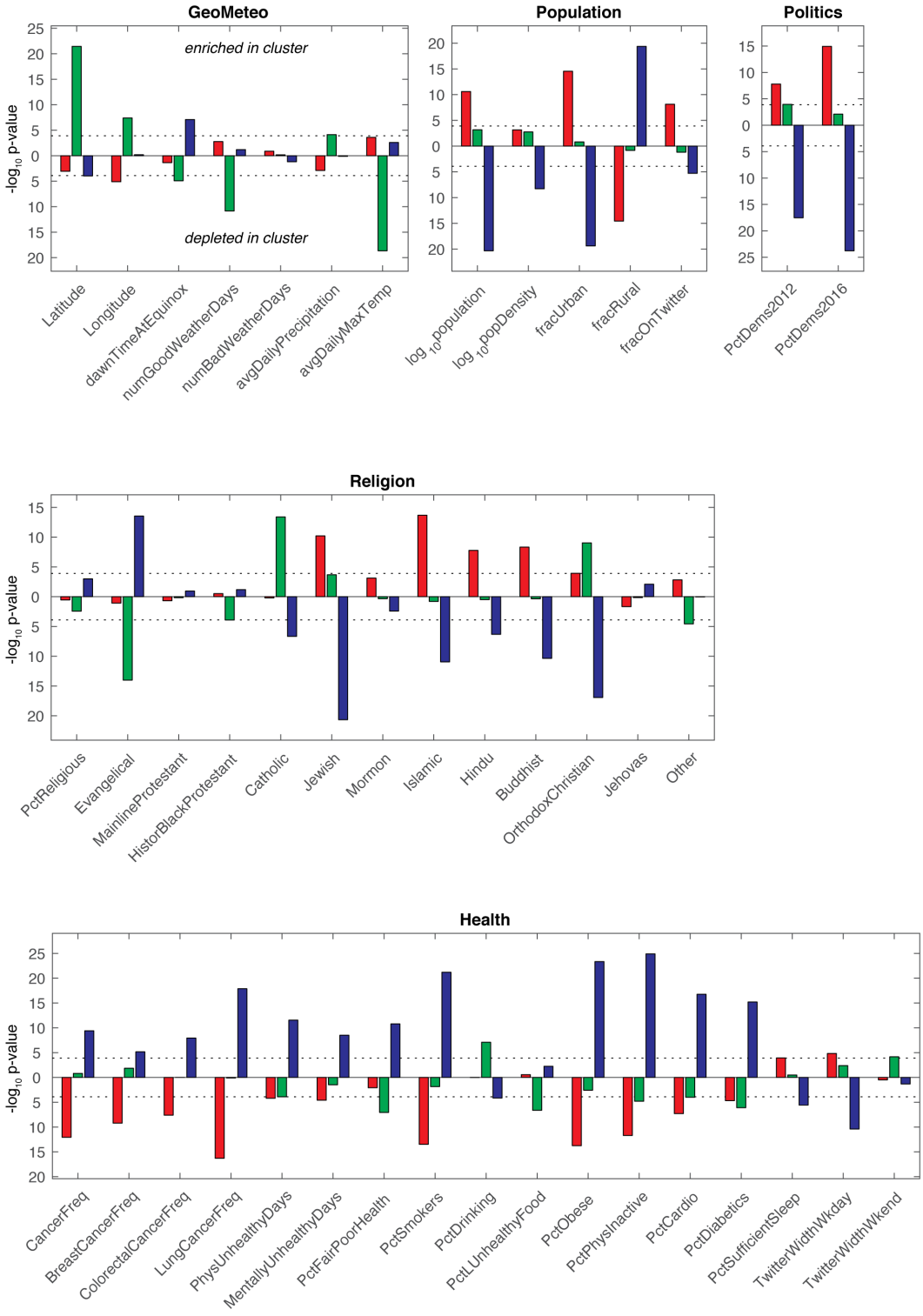

Figure S3.3 (continued).

Figure S3.3. Enrichment of demographic descriptors among clusters determined in Figure 3.4.

Enrichment of various socioeconomic, geographic and astronomical predictors in US counties clustered into four groups according to their seasonal changes in Twitter social jet lag Twitter. Colors correspond to cluster assignments in Figure 3.4. Each colored bar represents the $-\log_{10}$ p-value from the Kruskall-Wallis test comparing the distribution of a given socioeconomic predictor within counties in a particular cluster vs. all other counties in the dataset. A bar above the horizontal line indicates that the median value of the predictor is higher in counties within a given cluster in comparison to all other counties in the dataset (i.e., the cluster is enriched for this predictor). A bar below the horizontal line indicates that the cluster is depleted for a given predictor. If the medians of the distributions were equal, means were used to determine the direction of the bars. Dashed lines mark the Bonferroni-corrected threshold for controlling FWER at the 0.05 level.

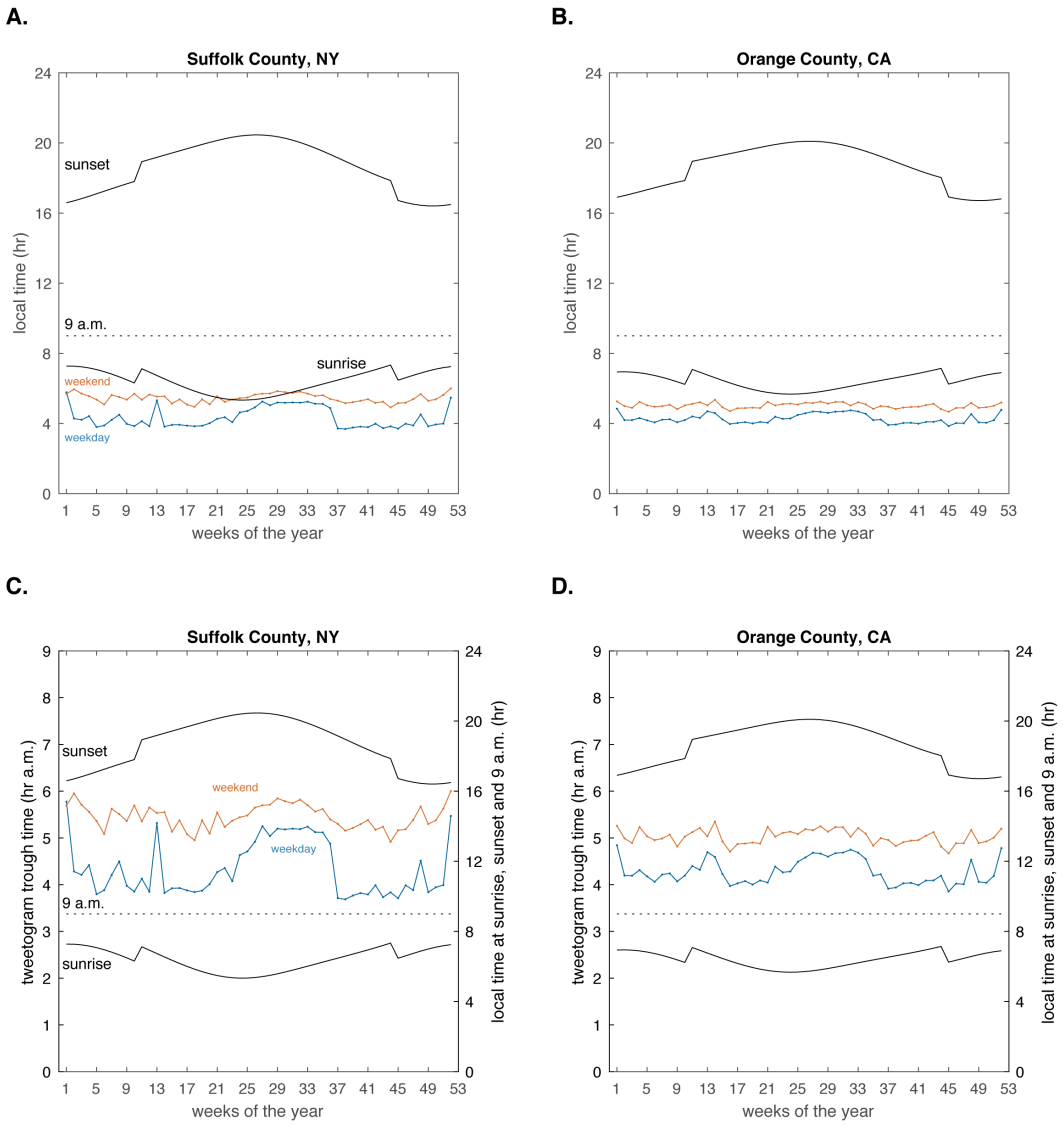

Figure S3.4. Weekly changes in tweetogram trough positions throughout 2013.
(A) Positions of weekend and weekday tweetogram troughs (orange and blue markers) in Suffolk County, NY, and Orange County, CA, plotted in local time (hr a.m.) for the 52 weeks of 2013. In the calendar convention employed here, weeks begin on Mondays and end on Sundays. Week 1 is defined as the full week when January 1 occurs (Dec. 31, 2012 – Jan. 6, 2013). Local times at 9 a.m., as well as at sunrise and sunset (when the sun is 0.833 degrees below the horizon), are indicated for reference.
(B) Data in (A) replotted using two vertical axes for clarity: tweetogram trough positions are plotted on the left vertical axes in local time, while the right vertical axes show the local times at 9 a.m., sunrise and sunset.

Covariate Code	Descriptive Name	Effect Size	StdErr	p-value
(Intercept)	(Intercept)	1.25E+00	7.78E-03	0.00E+00
Commute11	average commute length	-2.49E-03	1.15E-02	8.29E-01
Commute13	average morning commute start time	-3.88E-02	1.20E-02	1.22E-03
Edu7	% in high school	-1.59E-02	1.22E-02	1.94E-01
Edu8	% in college	-8.68E-02	1.60E-02	7.27E-08
Population1	$\log_{10}$population	-5.83E-03	1.11E-02	6.01E-01
Population5	% on twitter	4.44E-02	1.19E-02	2.01E-04
Sex1	% female	1.13E-02	1.00E-02	2.60E-01
Age1	median age	-9.58E-02	1.75E-02	5.01E-08
Race1	% white	2.94E-02	1.60E-02	6.52E-02
Household11	home ownership rate	3.83E-02	1.58E-02	1.54E-02
Employed1	employment rate	-1.06E-02	1.63E-02	5.14E-01
Income2	median income	2.81E-02	1.74E-02	1.07E-01
GeoMeteo1	latitude	4.65E-02	1.23E-02	1.59E-04
GeoMeteo2	longitude	5.24E-02	1.11E-02	2.76E-06
Health6	no. mentally unhealthy days per month	-7.51E-03	1.08E-02	4.85E-01
Health8	% smokers	3.86E-03	1.18E-02	7.43E-01
Health11	% obese	5.82E-02	1.37E-02	2.36E-05
Health15	% getting sufficient sleep	-1.60E-02	1.28E-02	2.11E-01
Health16	weekday tweetogram width	-4.20E-02	1.12E-02	1.87E-04
Health17	weekend tweetogram width	2.24E-02	9.91E-03	2.37E-02
Politics1	% Democratic voters	1.14E-02	1.29E-02	3.77E-01

Table S3.3. Covariates used in linear model.
Covariates used in linear model in Figure 2E, along with effect sizes (and their standard errors), as well as p-values from the linear regression model. Detailed coefficient descriptions are provided in Table S3.4.

Table S3.4. Descriptors of US counties used in this study.
Detailed descriptions of all US county descriptors used in this study. This table is provided online as a separate file.

REFERENCES

1. Roenneberg, T., Kuehnle, T., Juda, M., Kantermann, T., Allebrandt, K., Gordijn, M., and Merrow, M. (2007). Epidemiology of the human circadian clock. Sleep Medicine Reviews *11*, 429–438.

2. Roenneberg, T., and Merrow, M. (2016). The Circadian Clock and Human Health. Current Biology *26*, R432–R443.

3. Roenneberg, T., Keller, L.K., Fischer, D., Matera, J.L., Vetter, C., and Winnebeck, E.C. (2015). Human Activity and Rest In Situ. In Methods in Enzymology (Elsevier), pp. 257–283. Available at: http://linkinghub.elsevier.com/retrieve/pii/S0076687914000937 [Accessed April 4, 2018].

4. Wright, K.P., McHill, A.W., Birks, B.R., Griffin, B.R., Rusterholz, T., and Chinoy, E.D. (2013). Entrainment of the Human Circadian Clock to the Natural Light-Dark Cycle. Current Biology *23*, 1554–1558.

5. Stothard, E.R., McHill, A.W., Depner, C.M., Birks, B.R., Moehlman, T.M., Ritchie, H.K., Guzzetti, J.R., Chinoy, E.D., LeBourgeois, M.K., Axelsson, J., *et al.* (2017). Circadian Entrainment to the Natural Light-Dark Cycle across Seasons and the Weekend. Current Biology *27*, 508–513.

6. de la Iglesia, H.O., Fernández-Duque, E., Golombek, D.A., Lanza, N., Duffy, J.F., Czeisler, C.A., and Valeggia, C.R. (2015). Access to Electric Light Is Associated with Shorter Sleep Duration in a Traditionally Hunter-Gatherer Community. Journal of Biological Rhythms *30*, 342–350.

7. Moreno, C.R.C., Vasconcelos, S., Marqueze, E.C., Lowden, A., Middleton, B., Fischer, F.M., Louzada, F.M., and Skene, D.J. (2015). Sleep patterns in Amazon rubber tappers with and without electric light at home. Scientific Reports *5*. Available at: http://www.nature.com/articles/srep14074 [Accessed March 30, 2018].

8. Kreitzman, L. (2016). How the 24-hour society is stealing time from the night. Aeon. Available at: https://aeon.co/ideas/how-the-24-hour-society-is-stealing-time-from-the-night [Accessed May 1, 2018].

9. Zammit, G. (2006). The Effects of a 24-Hour Society. Sleep Review. Available at: http://www.sleepreviewmag.com/2006/01/the-effects-of-a-24-hour-society/ [Accessed May 1, 2018].

10. Wittmann, M., Dinich, J., Merrow, M., and Roenneberg, T. (2006). Social Jetlag: Misalignment of Biological and Social Time. Chronobiology International *23*, 497–509.

11. Roenneberg, T., Kantermann, T., Juda, M., Vetter, C., and Allebrandt, K.V. (2013). Light and the Human Circadian Clock. In Circadian Clocks, A. Kramer and M. Merrow, eds.

(Berlin, Heidelberg: Springer Berlin Heidelberg), pp. 311–331. Available at: http://link.springer.com/10.1007/978-3-642-25950-0_13 [Accessed April 23, 2018].

12. McMenamin, T.M. (2007). A time to work: recent trends in shift work and flexible schedules. Monthly Labor Review, 13.

13. Wöhrmann, A.M. (2016). Night- and shiftwork in Germany.

14. Juda, M., Vetter, C., and Roenneberg, T. (2013). Chronotype Modulates Sleep Duration, Sleep Quality, and Social Jet Lag in Shift-Workers. Journal of Biological Rhythms *28*, 141–151.

15. Castilhos Beauvalet, J., Luísa Quiles, C., Alves Braga de Oliveira, M., Vieira Ilgenfritz, C.A., Hidalgo, M.P., and Comiran Tonon, A. (2017). Social jetlag in health and behavioral research: a systematic review. ChronoPhysiology and Therapy *Volume 7*, 19–31.

16. Foster, R.G., Peirson, S.N., Wulff, K., Winnebeck, E., Vetter, C., and Roenneberg, T. (2013). Sleep and Circadian Rhythm Disruption in Social Jetlag and Mental Illness. In Progress in Molecular Biology and Translational Science (Elsevier), pp. 325–346. Available at: http://linkinghub.elsevier.com/retrieve/pii/B9780123969712000117 [Accessed April 9, 2018].

17. Haynie, D.L., Lewin, D., Luk, J.W., Lipsky, L.M., O'Brien, F., Iannotti, R.J., Liu, D., and Simons-Morton, B.G. (2018). Beyond Sleep Duration: Bidirectional Associations Among Chronotype, Social Jetlag, and Drinking Behaviors in a Longitudinal Sample of US High School Students. Sleep *41*. Available at: https://academic.oup.com/sleep/article/doi/10.1093/sleep/zsx202/4718366 [Accessed April 9, 2018].

18. Levandovski, R., Dantas, G., Fernandes, L.C., Caumo, W., Torres, I., Roenneberg, T., Hidalgo, M.P.L., and Allebrandt, K.V. (2011). Depression Scores Associate With Chronotype and Social Jetlag in a Rural Population. Chronobiology International *28*, 771–778.

19. de Souza, C.M., and Hidalgo, M.P.L. (2014). Midpoint of sleep on school days is associated with depression among adolescents. Chronobiol. Int. *31*, 199–205.

20. Parsons, M.J., Moffitt, T.E., Gregory, A.M., Goldman-Mellor, S., Nolan, P.M., Poulton, R., and Caspi, A. (2015). Social jetlag, obesity and metabolic disorder: investigation in a cohort study. International Journal of Obesity *39*, 842–848.

21. Koopman, A.D.M., Rauh, S.P., van 't Riet, E., Groeneveld, L., van der Heijden, A.A., Elders, P.J., Dekker, J.M., Nijpels, G., Beulens, J.W., and Rutters, F. (2017). The Association between Social Jetlag, the Metabolic Syndrome, and Type 2 Diabetes Mellitus in the General Population: The New Hoorn Study. Journal of Biological Rhythms *32*, 359–368.

22. Roenneberg, T., Allebrandt, K.V., Merrow, M., and Vetter, C. (2013). Social Jetlag and Obesity. Current Biology *23*, 737.

23. Díaz-Morales, J.F., and Escribano, C. (2015). Social jetlag, academic achievement and cognitive performance: Understanding gender/sex differences. Chronobiology International *32*, 822–831.

24. Haraszti, R.Á., Ella, K., Gyöngyösi, N., Roenneberg, T., and Káldi, K. (2014). Social jetlag negatively correlates with academic performance in undergraduates. Chronobiology International *31*, 603–612.

25. Smarr, B.L., and Schirmer, A.E. (2018). 3.4 million real-world learning management system logins reveal the majority of students experience social jet lag correlated with decreased performance. Scientific Reports *8*. Available at: http://www.nature.com/articles/s41598-018-23044-8 [Accessed April 4, 2018].

26. Roenneberg, T. (2013). The human sleep project: Chronobiology. Nature *498*, 427–428.

27. Nolan, T. (2014). Dance to the (circadian) rhythm. The Jawbone Blog. Available at: https://jawbone.com/blog/circadian-rhythm/ [Accessed April 4, 2018].

28. Walch, O.J., Cochran, A., and Forger, D.B. (2016). A global quantification of "normal" sleep schedules using smartphone data. Science Advances *2*, e1501705–e1501705.

29. Lampos, V., Lansdall-Welfare, T., Araya, R., and Cristianini, N. (2013). Analysing Mood Patterns in the United Kingdom through Twitter Content. Available at: https://arxiv.org/abs/1304.5507v1 [Accessed April 5, 2018].

30. Culotta, A., and Cutler, J. (2016). Mining Brand Perceptions from Twitter Social Networks. Marketing Science *35*, 343–362.

31. McCormick, T.H., Lee, H., Cesare, N., Shojaie, A., and Spiro, E.S. (2017). Using Twitter for Demographic and Social Science Research: Tools for Data Collection and Processing. Sociological Methods & Research *46*, 390–421.

32. Roenneberg, T. (2017). Twitter as a means to study temporal behaviour. Current Biology *27*, R830–R832.

33. Scheffler, T., and Kyba, C.C.M. (2016). Measuring Social Jetlag in Twitter Data. In Proceedings of the Tenth International AAAI Conference on Web and Social Media (Association for the Advancement of Artificial Intelligence), pp. 675–678.

34. Dzogang, F., Lightman, S., and Cristianini, N. (2017). Circadian mood variations in Twitter content. Brain and Neuroscience Advances *1*, 2398212817744501.

35. Golder, S.A., and Macy, M.W. (2011). Diurnal and Seasonal Mood Vary with Work, Sleep, and Daylength Across Diverse Cultures. Science *333*, 1878–1881.

36. Centers for Disease Control and Prevention (CDC) (2014). Behavioral Risk Factor Surveillance System Survey Data (Atlanta, Georgia: U.S. Department of Health and Human Services, Centers for Disease Control and Prevention).

37. Panda, S., Hogenesch, J.B., and Kay, S.A. (2002). Circadian rhythms from flies to human. Nature *417*, 329–335.

38. Hamrick, K.S., and McClelland, K. (2016). Americans' Eating Patterns and Time Spent on Food: The 2014 Eating & Health Module Data. Economic Information Bulletin, 51.

39. Liang, H., and Fu, K. (2015). Testing Propositions Derived from Twitter Studies: Generalization and Replication in Computational Social Science. PLOS ONE *10*, e0134270.

40. Bouchon, D. (1991). Biological clock in seasonal reproductive cycle in the ditch shrimp Palaemonetes varians Leach. I. Photoperiodie time measurement. J. Exp. Mar. Biol. Ecol. *146*, 12.

41. Prendergast, B.J., Nelson, R.J., and Zucker, I. (2002). Mammalian Seasonal Rhythms: Behavior and Neuroendocrine Substrates. 71.

42. Sashin, D. First day of school: Why August is the new September. CNN. Available at: https://www.cnn.com/2015/08/04/living/school-start-dates-august-parents-feat/index.html [Accessed May 5, 2018].

43. Kantermann, T., Juda, M., Merrow, M., and Roenneberg, T. (2007). The Human Circadian Clock's Seasonal Adjustment Is Disrupted by Daylight Saving Time. Current Biology *17*, 1996–2000.

44. Roenneberg, T., Kumar, C.J., and Merrow, M. (2007). The human circadian clock entrains to sun time. Current Biology *17*, R44–R45.

45. Allebrandt, K.V., Teder-Laving, M., Kantermann, T., Peters, A., Campbell, H., Rudan, I., Wilson, J.F., Metspalu, A., and Roenneberg, T. (2014). Chronotype and sleep duration: The influence of season of assessment. Chronobiology International *31*, 731–740.

46. Amanda Lenhart (2015). Mobile Access Shifts Social Media Use and Other Online Activities. Pew Research Center: Internet, Science & Tech. Available at: http://www.pewinternet.org/2015/04/09/mobile-access-shifts-social-media-use-and-other-online-activities/ [Accessed April 10, 2018].

47. Duggan, M. (2015). The Demographics of Social Media Users. Pew Research Center: Internet, Science & Tech. Available at: http://www.pewinternet.org/2015/08/19/the-demographics-of-social-media-users/ [Accessed April 10, 2018].

48. Tibshirani, R., Walther, G., and Hastie, T. (2001). Estimating the number of clusters in a data set via the gap statistic. Journal of the Royal Statistical Society: Series B (Statistical Methodology) *63*, 411–423.

49. Robert Wood Johnson Foundation, and University of Wisconsin Population Health Institute Use the Data. County Health Rankings & Roadmaps. Available at: http://www.countyhealthrankings.org/explore-health-rankings/use-data.

50. U.S. Census Bureau, 2011-2015 American Community Survey 5-Year Estimates Available at: https://www.census.gov/programs-surveys/acs/about.html.

51. U.S. Census Bureau, 2010 Census Available at: https://www.census.gov/2010census/data/.

52. Institute for Health Metrics and Evaluation (IHME) United States Cardiovascular Disease Mortality Rates by County 1980-2014. Available at: http://ghdx.healthdata.org/record/united-states-cardiovascular-disease-mortality-rates-county-1980-2014.

53. Cancer Data 2013 from the Centers for Disease Control and Prevention (CDC) & the Centers for Medicare & Medicaid Services (CMS) (2017). Available at: http://old.socialexplorer.com/pub/reportdata/HtmlResults.aspx?reportid=R11549815.

54. Health Data 2014 (SE), Health Data 2014, Social Explore; County Health Rankings & Roadmaps (2017). Available at: http://old.socialexplorer.com/pub/reportdata/HtmlResults.aspx?reportid=R11549794.

55. Health Data 2016 (SE), Health Data 2016, Social Explorer; County Health Rankings & Roadmaps (2017). Available at: http://www.socialexplorer.com/pub/reportdata/HtmlResults.aspx?reportid=R11549809.

56. Religions by Tradition (TR), Religion 2010 (InfoGroup), Data collected by InfoGroup, organized by the ARDA, tabulated and processed by Social Explorer (2017). Available at: http://www.socialexplorer.com/pub/reportdata/HtmlResults.aspx?reportid=R11549793.

57. CDC Sleep and Sleep Disorders Team (2017). Short Sleep Duration Among US Adults. Centers for Disease Control and Prevention: Sleep and Sleep Disorders. Available at: https://www.cdc.gov/sleep/data_statistics.html [Accessed April 8, 2018].

58. Kennedy, S. Astral v1.6.

59. Solar Calculation Details Earth System Research Laboratory Global Monitoring Division. Available at: https://www.esrl.noaa.gov/gmd/grad/solcalc/calcdetails.html.

60. North America Land Data Assimilation System (NLDAS) Daily Precipitation for years 1979-2011 on CDC WONDER Available at: http://wonder.cdc.gov/NASA-Precipitation.html [Accessed December 20, 2017].

61. North America Land Data Assimilation System (NLDAS) Daily Air Temperatures and Heat Index, years 1979-2011 on CDC WONDER Online Database, released 2013. Available at: http://wonder.cdc.gov/NASA-NLDAS.html [Accessed December 15, 2017].

62. Olesen, B.W., and Parsons, K.C. (2002). Introduction to thermal comfort standards and to the proposed new version of EN ISO 7730. Energy and Buildings *34*, 537–548.

63. Fanger, P.O. (1970). Thermal comfort. Analysis and applications in environmental engineering. Thermal comfort. Analysis and applications in environmental engineering. Available at: https://www.cabdirect.org/cabdirect/abstract/19722700268 [Accessed May 14, 2018].

64. McGovern, T. County-Level Presidential General Election Results for 2012 - 2016. Available at: https://github.com/tonmcg/County_Level_Election_Results_12-16 [Accessed December 15, 2017].

65. Rogers, S., and Cage, F. Full US 2012 election county-level results to download. The Guardian. Available at: https://www.theguardian.com/news/datablog/2012/nov/07/us-2012-election-county-results-download#data [Accessed December 15, 2017].

66. Election 2016 Results townhall.com. Available at: https://townhall.com/election/2016/president/ [Accessed December 15, 2017].

67. Sokal, R.R., and Rohlf, J.F. (1995). Biometry (Macmillan).

68. Roenneberg, T., Kuehnle, T., Pramstaller, P.P., Ricken, J., Havel, M., Guth, A., and Merrow, M. (2004). A marker for the end of adolescence. Current Biology *14*, R1038–R1039.

Appendix A: FITNESS OF CYANOBACTERIAL CLOCK MUTANTS IN CYCLING LIGHT-DARK ENVIRONMENTS

INTRODUCTION

Experiments by Johnson and colleagues indicate that a cyclic LD environment of a given period favors an *S. elongatus* mutant with a resonant circadian clock over mutants whose clocks have longer or shorter periods, suggesting that a mutant is most fit in a resonant LD environment [1,2]. But how the magnitude of this clock-conferred fitness varies across LD cycles of varied duration has not been tackled, in part because the necessary experiments are very laborious using traditional protocols. One of the goals of my thesis was to overcome these challenges by building on the LED array methodology described in Chapter 2 and systematically query the fitness of *S. elongatus* in LD environments with period 10-48 hours. For asexual microbes, the difference in growth rate of two populations grown in competition is a convenient and established measure of relative fitness [2].

Competition experiments offer several advantages over direct measurements of growth rates of cultures grown in isolation. Previous studies failed to identify appreciable differences in fitness when the strains were grown separately in batch culture, perhaps because unavoidable differences in growth conditions (e.g., light exposure, optical density, growth chamber parameters) masked the effects of circadian disruption. The advantage of competitions is that they are internally-controlled growth assays, in which both strains receive identical experimental treatment and face identical growth conditions. There is no evidence that the effects observed in competition are due to communication between the two strains (e.g., via secreted factors [3]).

My strategy to isolate the fitness effects conveyed by a 24-hour clock was to grow WT cells in competition with the clock-delete mutant Δ*kaiBC*, which has no free-running rhythms in gene expression but can respond directly to LD stimuli [4]. This chapter describes the methodology I developed to grow cyanobacterial strains in competition in a wide range of LD cycles in 96-well plates (using LED arrays) and assess relative fitness by monitoring changes in relative population abundance over time (using fluorescent microscopy).

My expectation was that the Δ*kaiBC* strain has an approximately flat fitness profile across these conditions, reflecting general changes in cell physiology in response to the frequency of light-dark transitions. Thus, the differences in growth rates of the WT and Δ*kaiBC* strains across light regimes would report on clock-specific fitness effects. The resulting fitness curve would address several basic questions: how precise is the adaptation to a 24-hr day? Are longer or shorter days more deleterious? What is the most debilitating LD rhythm?

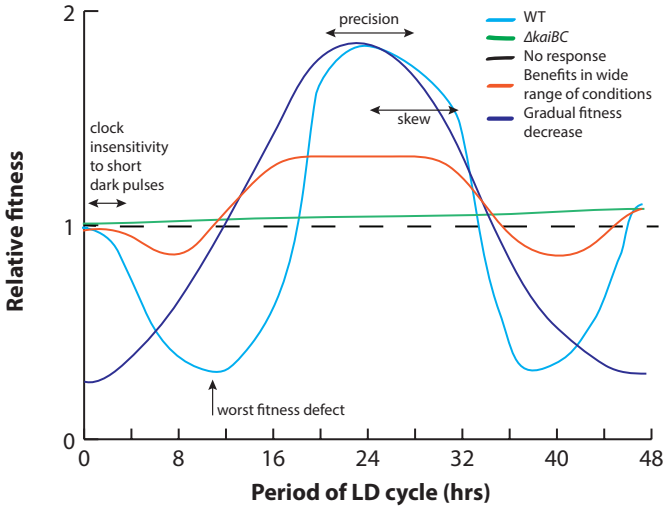

Figure A.1. Hypothetical fitness profiles of WT and ΔkaiBC as the period of the light-dark cycle is varied.
Light-dark cycles are assumed to be balanced between light and dark (i.e., 24-hr period refers to LD12:12). Fitness values are defined as growth rate in a given LD cycle divided by growth rate in conditions with rapidly fluctuating light-dark cycles (approximating constant light at half intensity, which is assumed to be the same for WT and Δ*kaiBC*).

Figure A.1 illustrates hypothetical outcomes I considered before embarking on these experiments. *S. elongatus* cells do not grow in the dark; when the lights are turned on after prolonged darkness, cyanobacteria spend several hours recovering before reaching a steady state rate of biomass incorporation in constant light. Thus, I expect the Δ*kaiBC* mutant (green curve) to be relatively insensitive to the environmental period. On the other hand, I expected the fitness of the WT strain to peak around 24-hours. Away from the peak, fitness may decrease monotonically in both directions (purple line), suggesting that the clock benefit is lost gradually as environmental period deviates from 24 hours. But my prediction was that the measured fitness curve would look like the solid red curve: in really short or really long LD cycles, the predictions of a 24-hr timekeeper are useless and the Δ*kaiBC* strain would be as fit as the WT strain. However, for an intermediate range of LD periods, the clock will respond to environmental LD rhythms by modulating the phase of gene expression relative to dawn and dusk. The nadirs of the fitness landscape indicate LD conditions where the clock's predictions of dawn and dusk are significantly out of phase with the actual timing of dawn and dusk. The width of the peak reflects the precision of circadian adaptation to 24-hr days, and the skew of the curve indicates whether the WT cell prefers shorter or longer days.

The rest of this Appendix describes my efforts to measure such a fitness curve for *S. elongatus*. Though the answers I got (Figure A.6G) argue against the hypothesis described above, my experiments revealed that relative fitness between WT and clock-null mutants depends on specific growth conditions and genetic background. This appendix focuses on description of methods developed for this study so they may be useful in future experiments in the Rust Lab. I also detail my efforts to replicate results published in the literature [2,5].

METHODS

Overview of methods

To understand how the circadian clock conveys fitness to cyanobacteria faced with varying LD environments, I needed to perform multiplexed competition experiments of *S. elongatus* mutants in dozens of different light regimes and in many mutant combinations simultaneously. To this end, I built growth chambers in a 96 well-plate format with tunable LED-based illumination of individual wells (see Figure A.3 and Chapter 2). To detect fitness differences, I developed protocols to maintain mixtures of mutant cultures in these devices for 30-40 generations (doubling time ≈24 hours), with regular passage of cells into fresh media at low optical density. I also developed protocols to assess of the composition of mutants in the mixture using fluorescent microscopy in 96-well format. To facilitate these studies, I engineered a series of mutants with diverse clock phenotypes carrying fluorescent markers and reporters of gene expression. Finally, in a follow-up to the work described in Chapter 2, I measured the growth curves of wild-type and clock-null mutants in 24-hr cycles of varied day length; for these experiments, cells were grown in flasks under white fluorescent lights. The following sections describe the methods in detail.

Cyanobacterial strains engineered for this study

Figure A.2A describes the cloning strategy used to generate various clock mutants for this study. Beginning with a WT *S. elongatus* strain, I inactivated the genomic *kaiBC* locus by interrupting it with a gentamicin-resistance cassette. To generate the desired clock phenotype, a

transgenic copy of *kaiBC,* carrying the appropriate point mutation, was inserted under its native P_{kaiBC} promoter in Neutral Site 1 in the genome. A construct carrying a fluorescent marker (EYPF or mTurquoise2) under an inducible promoter and a luminescence reporter of clock gene expression (P_{psbAI}*::luxAB* P_{psbAI}*::luxABCDE*) was targeted to Neutral Site 2 in the genome. Figure A.2B-C shows luminescence traces of select mutants generated using this approach, illustrating short-period, long-period and arrhythmic clock phenotypes in addition to a rescue of wild-type rhythms. Microscopy images in Figure A.2C-D illustrate the induction of the fluorescent proteins two selected strains.

To verify that the outcomes of the competition experiments were not artifacts of the multiple (potentially deleterious) genetic manipulations, I also made use of a simpler pair cyanobacterial strains carrying the minimum genetic tools necessary to do the experiments: a clock-null mutant in WT background (Δ*kaiBC* generated by disruption of gentamicin cassette, as described above) and WT cells carrying an inducible fluorescent marker (EYFP) in Neutral Site 1 (Figure A.2F-G).

Detailed descriptions of plasmids and strains can be found in Table A.1 and Table A.2. Plasmid maps have been deposited on Rust Lab Dropbox (Table A.4).

Methods for competitive growth experiments reported in prior literature

Here, I briefly summarize methods described in the literature in order to facilitate the comparison with the methods I developed. In the initial study by Ouyang et al. [2], which reported fitness advantages in clock mutants grown in environments with resonant light-dark cycles, the authors used wild type strains and period mutants carrying different antibiotic

resistance genes. The wild type strains AMC149 (spectinomycin resistant) and AMC343 (chloramphenicol resistant) both carry a luminescence reporter of clock gene expression (*PpsbAI::luxAB*) in a neutral site in the genome. Period mutants C22 and C27 were derived by chemical mutagenesis of AMC149 and are thus also resistant to spectinomycin. In competition assays, these strains were mixed at OD_{750} ≈0.001 and grown together in flasks with aeration under white fluorescent lights (≈100 μE) at 30 °C. The cultures were diluted every 8 days and the proportion of mutants in the mixture was determined by plating equal volumes on solid media supplemented with appropriate antibiotics. Ouyang et al. do not specify the dilution factor, but a follow-up report from the same group mentions that mixtures grown in competition were diluted 1:30 into fresh BG11 media every 8 days [2,5].

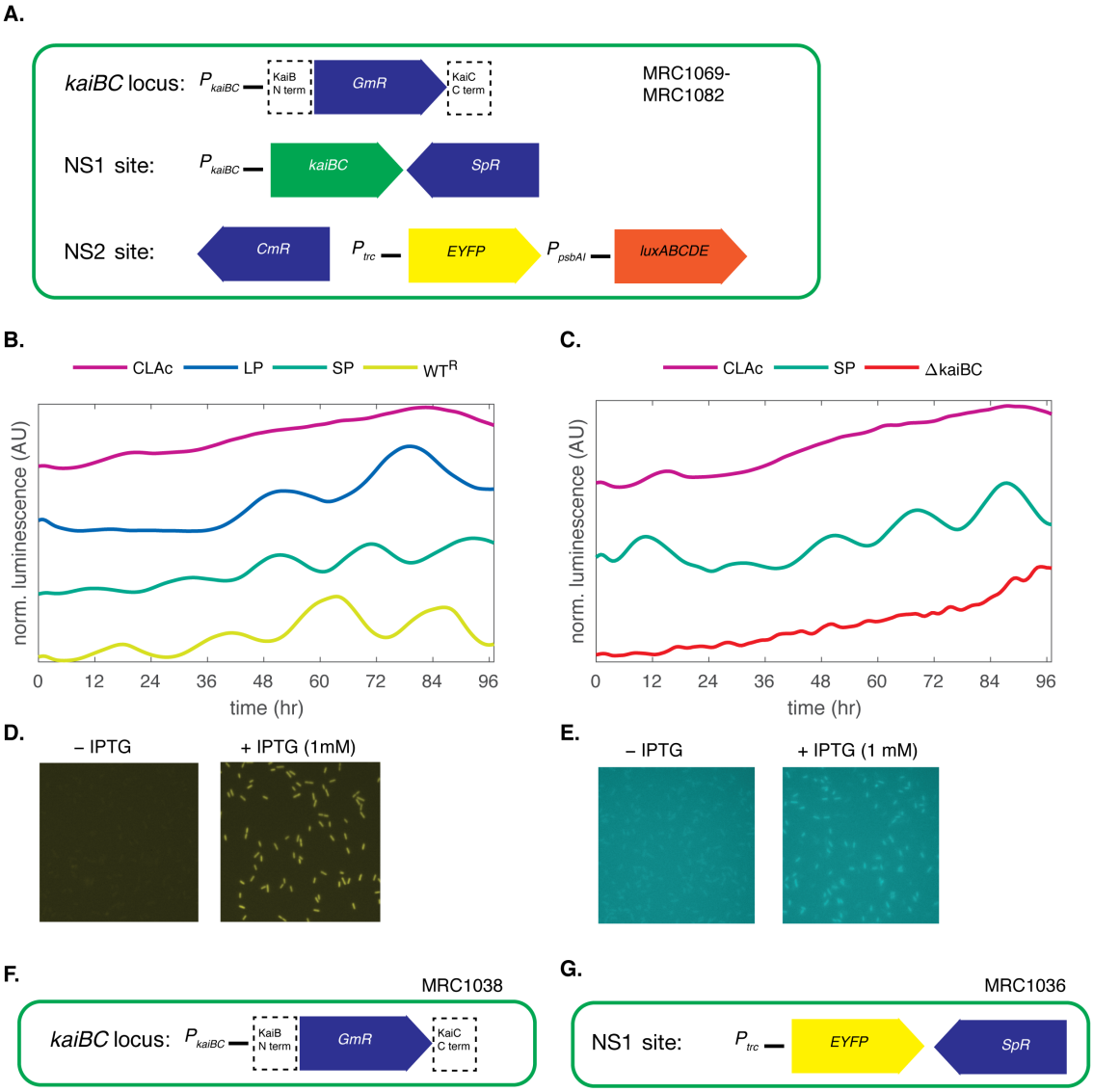

Figure A.2. Clock mutants engineered for this study.
(A) Cloning strategy to generate a cyanobacterial clock mutant carrying a fluorescent marker and luminescent reporter of clock gene expression. The genomic locus carrying the *kaiBC* operon was interrupted by a gentamicin-resistance cassette (*GmR*), and another copy of *kaiBC* (either WT or carrying the appropriate point mutation) driven by the native promoter (P_{kaiBC}) was targeted to neutral site 1 (NS1) in the genome using a streptomycin-resistance (*SpR*) cassette as a selectable marker. Additionally, a plasmid carrying an inducible copy of a fluorescent protein (EYFP or mTurquoise2), a luminescent clock gene expression reporter (*PpsbAI::luxAB PpsbAI::luxCDE*) and a chloramphenicol-resistance cassette (*CmR*) was targeted to neutral site 2 (NS2) in the genome under chloramphenicol selection. Strains MR1069-1082 were generated in this way (Table A.2).

(Figure A.2 continued) (B) Luminescence signals recorded in continuous light from four EYFP-tagged clock mutants (CLAc, an arrhythmic strain, MRC1074; LP, long-period mutant, MRC1072; SP, short-period mutant, MRC1071; WT^R, wild-type rescue, MRC1070). Cells were received one LD12:12, then released into constant light (LL). Data from first 96-hours in LL is shown. Luminescence trajectories were processed by subtracting the minimum values and normalizing by the mean ($y_{norm} = (y - min(y))/mean(y)$), then smoothed using a 5-hr Gaussian kernel. The curves are offset vertically for clarity. Luminescence measurements collected using the standard protocol (e.g., see Chapter 1 or [6]).
(C) Luminescence recordings from mTurquoise-tagged arrhythmic mutant (CLAc, MRC1081), short-period mutant (SP, MRC1078) and Δ*kaiBC* (MRC1076). Data was collected and processed as in **(B)**.
(D) Microscopy images of EYFP-tagged short-period mutant (MRC1071) grown in constant light for 16 hours with (+) or without (-) 1 mM IPTG. The two samples were imaged in side-by-side wells of a 96-well plate using the same settings. Magnification was 40x. Images are displayed with the same contrast settings.
(E) Microscopy images of mTurquoise-tagged arrhythmic mutant (CLAc, MRC1081) grown with (+) or without (-) 1 mM IPTG. Induction, imaging and processing settings were same as in **(C)**.
(F-G) Genotypes of Δ*kaiBC* (MRC1038) and WT-EYFP (MRC1036) used in this study.

Table A.1. Plasmids used in this study.
All plasmids are stored in the Rust Lab plasmid collection (MR). Relevant plasmid maps have been uploaded to Rust Lab Dropbox. The naming nomenclature of clock point mutants in this table follows the original publications [7,8].

MR plasmid library code	backbone	insert	description	gen-omic target site	anti-biotic in *E. coli*	anti-biotic in *S. elongatus*
MR0149	pAM2991	SYFP at EcoRI	Ptrc::SYFP	NS1	Spec	Spec
MR0150	pAM2991	mTurquoise2 at EcoRI	Ptrc::mTurquoise2	NS1	Spec	Spec
MR0151	pAM2991	EYFP at EcoRI	Ptrc::EYFP (made by Gopal Pattanayak)	NS1	Spec	Spec
MR0152	pAM2991	ECFP at EcoRI	Ptrc::ECFP (made by Gopal Pattanayak)	NS1	Spec	Spec
MR0153	pAM2195	LacI-Ptrc-SYFP	Ptrc::SYFP, PpsbaAI:: luxABCDE	NS2	Amp	Cm
MR0154	pAM2195	LacI-Ptrc-mTurquoise2	Ptrc::mTurquoise2, PpsbaAI:: luxABCDE	NS2	Amp	Cm

(Table A.1**, continued)**						
MR0155	pAM2195	LacI-Ptrc-EYFP at XhoI	Ptrc::EYFP, PpsbaAI:: luxABCDE	NS2	Amp	Cm
MR0156	pAM2195	LacI-Ptrc-ECFP at XhoI	Ptrc::ECFP, PpsbaAI:: luxABCDE	NS2	Amp	Cm
MR0157	pAM2314	PkaiBC-KaiBC at SpeI/SacII	PkaiBC::KaiC WT in pAM2314 (made by Gopal Pattanayak)	NS1	Spec	Spec
MR0158	pEL005	C22 via quikchange	C22, short-period mutant, Ala87 → Val	NS1	Spec	Spec
MR0159	pEL005	C27 via quikchange	C27a, long-period mutant, Thr409 → Ala	NS1	Spec	Spec
MR0160	pEL005	CLAb via quikchange	CLAb, arrhythmic mutant, Gly460 → Glu	NS1	Spec	Spec
MR0161	pEL005	CLAc via quikchange	CLAc, arrhythmic mutant, Thr495 → Ala	NS1	Spec	Spec
MR0162	pAM2314	pr1	pr1, phase-resetting mutant, Ala422 → Val (opposite orientation from MR0158-161)	NS1	Spec	Spec
MR0091	pBlue Script II (SK+)	GmR cassette flanked by PkaiBC/kaiBC fragments	Δ*kaiBC* knock-out plasmid (made by Gopal Pattanayak)	kaiBC	Amp	Gm

Table A.2. *S. elongatus* strains used in this study.
All strains listed are available in the Rust Lab strain collection (MRC). MRC also contains clock point mutants engineered in analogous fashion to MRC1069-MRC1075, but in a background containing a reporter of circadian gene expression suitable for single-cell studies (*PkaiBC::EYFP-ssrA*). The naming nomenclature of clock point mutants in this table follows the original publications [7,8].

MRC code	description	genomic modification		NS1 insert		NS2 insert	
		targeting plasmid	anti-biotic marker	targeting plasmid	anti-biotic marker	targeting plasmid	anti-biotic marker
MRC 1069	ΔkaiBC, Ptrc::EYFP, PpsbAI::luxABCDE	MR0091	gmR	none	none	MR0155	cmR
MRC 1070	kaiBC (WT) rescue in MRC1069 background	MR0091	gmR	MR0157	spR	MR0155	cmR
MRC 1071	short period mutant (C22) in MRC1069 background	MR0091	gmR	MR0158	spR	MR0155	cmR
MRC 1072	long period mutant (C27) in MRC1069 background	MR0091	gmR	M0159	spR	MR0155	cmR
MRC 1074	arrhythmic mutant (CLAc) in MRC1069 background	MR0091	gmR	MR0161	spR	MR0155	cmR
MRC 1075	phase-resetting mutant (pr1) in MRC1069 background	MR0091	gmR	MR0162	spR	MR0155	cmR
MRC 1076	ΔkaiBC, Ptrc::mTurquoise2, PpsbAI::luxABCDE	MR0091	gmR	none	none	MR0154	cmR
MRC 1077	kaiBC (WT) rescue in MRC1076 background	MR0091	gmR	MR0157	spR	MR0154	cmR
MRC 1078	short period mutant (C22) in MRC1076 background	MR0091	gmR	MR0158	spR	MR0154	cmR
MRC 1079	long period mutant (C27) in MRC1076 background	MR0091	gmR	M0159	spR	MR0154	cmR
MRC 1081	arrhythmic mutant (CLAc) in MRC1076 background	MR0091	gmR	MR0161	spR	MR0154	cmR
MRC 1082	phase-resetting mutant (pr1) in MRC1076 background	MR0091	gmR	MR0162	spR	MR0154	cmR
MRC 1083	AMC1300 (WT *S. elongatus* with PkaiBC::luxAB reporter)			PkaiBC::luxAB	spR	PpsbAI::luxCDE	kanR

(Table A.2 continued)							
MRC 1084	ΔkaiBC in AMC1300 background	MR0091	gmR	PkaiBC:: luxAB	spR	PpsbAI:: luxCDE	kanR
MRC 1035	WT *S. elongatus* 7942						
MRC 1036	WT/Ptrc::EYFP			MR0151	spR		
MRC 1037	WT/Ptrc::ECFP			MR0152	spR		
MRC 1038	ΔkaiBC in WT background	MR0091	gmR				

Experimental workflow for competition experiments in 96-well format developed for this study

Figure A.3 depicts the typical workflow for a competition experiment, which can be broken down into two parts: first (green ovals) propagating a mixture of cells in 96-well plates under LED arrays for 30-40 generations, and second (yellow ovals) periodically sampling the mixtures and assessing the composition of mutant strains using fluorescent microscopy in 96-well format. These steps and important considerations are described in detail below.

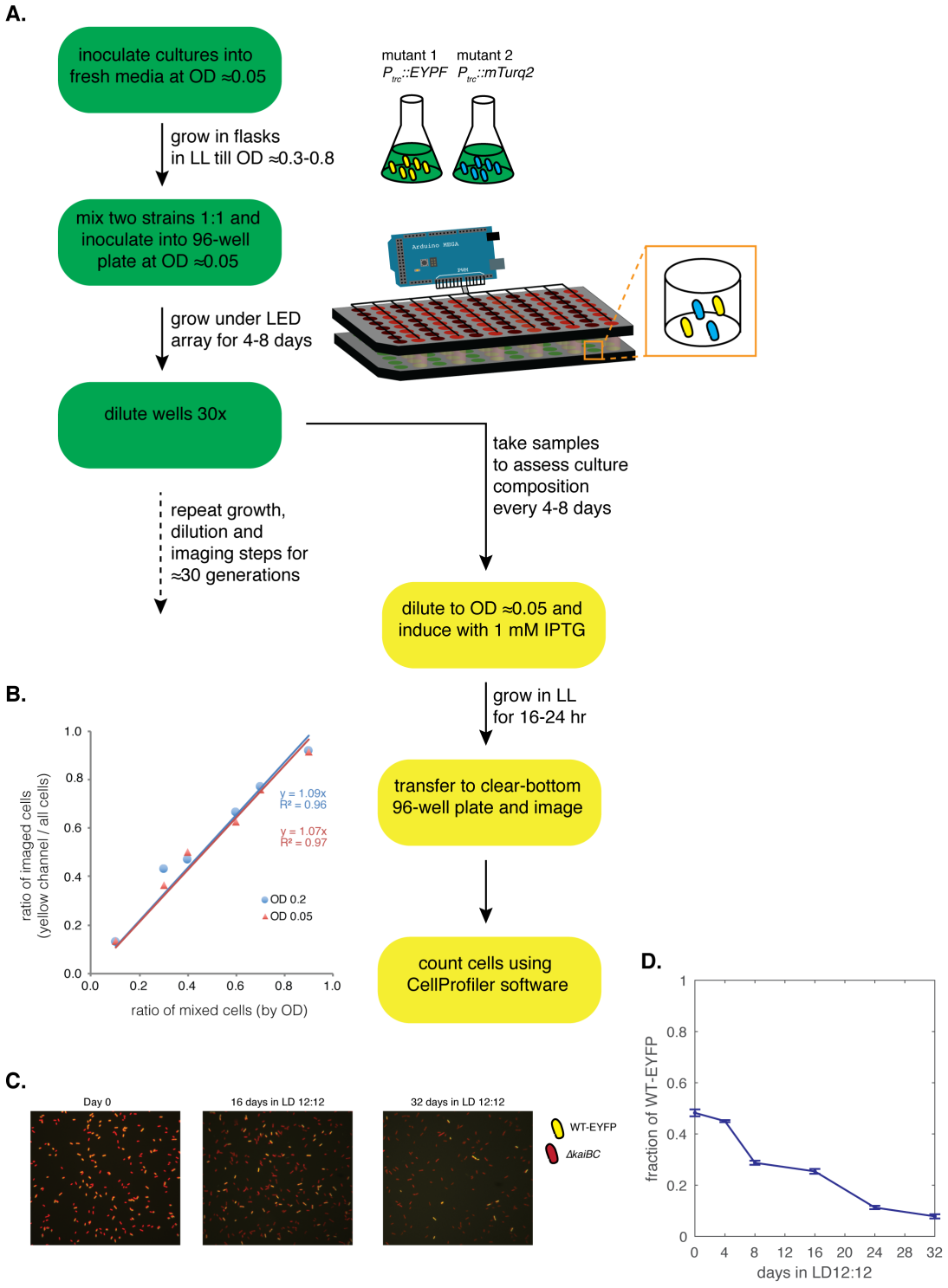

Figure A.3. Experimental workflow for studying fitness of cyanobacterial clock mutants via competitive growthassays in 96-well format.
(A) Experimental workflow (see Methods).

(Figure A.3, continued) (B) Multi-well fluorescent imaging and automated image processing can be used to reliably calculate the proportion EYFP-tagged cyanobacterial cells in a mixture. In this experiment, EYFP-tagged short-period mutant (MRC1071) and mTurquoise-tagged CLAc mutant (MRC1081) were mixed at OD_{750} 0.2 or 0.05 in various ratios, and the mixtures were grown for ≈19 hr with shaking (≈200 rpm) in a transparent 96-well plate in the presence of 1 mM IPTG on under while fluorescent lights (≈75-100 μE) in the Percival growth chamber. Mixtures were then transferred to a clear-bottom 96-well plate (Greiner FLUOTRAC High-binding, cat. no. 655097) and imaged using a 40x dry objective (0.7 NA). The fraction of YFP^+ cells was measured using a customized image analysis pipeline in CellProfiler. Each condition was imaged in triplicate (error bars representing standard deviations are smaller than marker sizes). Linear regressions were carried out in Excel (Microsoft) enforcing a y-intercept of 0.
(C) Example images from day 0, day 16 and day 32 of an experiment where WT-EYFP (MRC1036) was competed against Δ*kaiBC* (MRC1038) in LD 12:12. EYFP and Cy3 channels were overlaid.
(D) Fraction of WT-EYFP cells remaining in the mixture over time in the competition experiment in **(C)**. See Figure A.6**(B)** for other conditions from the same experiment.

General considerations.

- All experiments used unbuffered BG11M growth medium (no HEPES).
- Antibiotics were used only to select for positive clones during strain engineering, but not for competition experiments.
- To prevent contamination over the course of experiments, all culturing steps were performed using sterile technique. E.g., open flasks and 96-well plates were only used in a sterile hood. Before the beginning of each experiment, all cultures were streaked on LB-agar without antibiotics to check for bacterial contamination. During the course of the competition experiments, random wells were similarly tested for contamination.
- Because each experiment is very long (3-5 weeks) and laborious, it is important to design it in a way that reduces the likelihood of failure during many handling steps over this time period. (Of course, this is true for any experiment, but it's more painful to destroy your efforts two weeks into an experiment than two hours into one.) It is important to

plan each competition assay meticulously, write out detailed plate layouts, design schedules and protocols of sampling/dilution steps ahead of time, and to create spreadsheets to facilitate note-taking during OD measurements and other steps. It is highly advisable to use multichannel pipets to reduce pipetting errors.

- Throughout these experiments, it is necessary to periodically remove plates from under the LED arrays (e.g., to dilute cultures or to add water to offset evaporated volumes). Because different columns of the LED arrays are typically on different light-dark schedules (often with non-24 hr period), it is impossible (or impractical) to perform these steps while all of the wells are lit. My solution has been simply to perform the handling steps as quickly as possible (<30 min) and at the same time of day throughout the experiment.

I. Propagating mixtures of cyanobacterial strains in 96-well plates under LED arrays.

i. Preparation of actively growing cultures. Before the beginning of each experiment, strains were typically maintained on the benchtop in flasks or test tubes at room temperature in BG11M medium. Though cyanobacteria can be maintained in such conditions for several weeks or months, these cultures quickly reach very high density and are no longer actively growing. To get consistent results, it is important to passage these cells in fresh medium for several doublings to return the cells to an actively dividing state. To do so, cells were typically inoculated into 50-100 mL of fresh BG11M into acid-washed 250 mL flasks at low optical density ($OD_{750\ nm}$ = 0.01 – 0.05, henceforth OD). Cultures grown in continuous light in the Percival growth chamber under standard

conditions (30 °C, 70-100 μE, shaking at 200 rpm). If starting cultures were taken directly from freezer stocks (stored at −80 °C in BG11 with 5% DMSO), cells were first inoculated into 5-10 mL of fresh BG11M and allowed to grow up in test tubes for several generations, and only then transferred into 50-100 mL in flasks, as described above.

ii. *Inoculation of mixtures of mutant strains into 96-well plates*. Actively growing cultures were diluted to low density (OD 0.001 - 0.05) in BG11M and appropriate combinations were mixed in equal volumes in 50 mL conical tubes. These master mixtures were transferred into black 96-well plates (Costar 3916), 200 μL/well, using a multichannel pipet. Experiments were designed such that wells in the same column always contained replicate mixtures. Only the middle four rows were used to culture cells (e.g., C1-F1 in column 1), and the other rows were filled with water. Rows A, B, G and H were avoided for culturing purposes because they experience rapid evaporation (150-180 μL in 4-5 days). Plates were sealed with transparent film (Uniseal, GE cat. no. 7704-0001) and holes were punctured above each well to provide aeration with a 26G½ needle (BD, cat. no. 305111). To facilitate this process, a 96-well hole-punching apparatus was designed by gluing needles into hollow 96-well plates.

iii. *Culturing mixtures of mutants in 96-well plates in custom light-dark environments.* Plates containing liquid cultures were grown under LED arrays (described in Chapter 1) programmed to the desired light-dark schedule (≈100-200 μE during the light). Plates were placed on a shaking platform (≈100 rpm) in a dark 30 °C incubator using custom 3D-printed 96-well holders.

iv. *Periodically replenishing evaporated volume.* Under these conditions, wells in rows C-F of a 96-well plate typically lose about 40-50% of volume in four days. Thus, every 2-4 days, replicate wells from each column were pooled and supplemented with Milli-Q H_2O or BG11 to offset the evaporated volume.

- Though water is the correct medium to replenish evaporated volumes while maintaining osmolarity, the addition of BG11M does not seem to affect the qualitative outcome of the experiments (compare Figure A.6A-B vs. C-F). The frequency with which evaporated volumes are replenished also does not seem to play a major role. Refer to Table A.3. Variations in experimental protocols used in competition assays.Table A.3 for specifics for individual experiments presented in this Appendix.

v. *Periodic dilution.* Every 8 days, replicate wells from each column were pooled and diluted 30-fold into fresh BG11M in a new black 96-well plate. Empty rows were filled with water, plates were sealed with transparent film and returned to the shaker, as described in step *iii*. Samples from pooled mixtures were used for the microscopy analysis in step *II.i.*

Experiment	Starting $OD_{750\ nm}$	Evaporated volume adjustment		Dilution	
		frequency	liquid used	frequency	dilution ratio
Figure A.4	0.05	every 2 days	Milli-Q H_2O	every 8 days	1:30
Figure A.5	0.001	every 4 days	BG11M	every 8 days	1:30
Figure A.6 A,C,D,F	0.05	every 4 days	BG11M	every 8 days	1:30
Figure A.6 B,E	0.05	every 4 days	Milli-Q H_2O	every 8 days	1:30

Table A.3. Variations in experimental protocols used in competition assays.

II. Quantifying the composition of populations grown in competition using fluorescent microscopy.

i. *Sampling and induction of fluorescent protein expression.* Cultures grown in competition were sampled only on days when the plates also had to be handled for a different purpose, e.g., in order to replenish evaporated volume or to dilute dense cultures (steps *I.ii*, *I.iv* or *I.v* above). Samples of pooled mixtures were transferred in triplicate to transparent 96-well plates filled with 200 µL BG11M supplemented with 1 mM IPTG at a final OD ≈ 0.05. As described in *I.ii*, plates were sealed with transparent film and aeration holes were punctured. These plates were then transferred to the Percival incubator and grown under standard conditions (30 °C, 70-100 µE, shaking at 200 rpm) for 16-20 hr.

- The exact OD used for induction is not critical, as I have verified that the mixture composition can be detected reliably by the downstream imaging/processing pipeline across a range of ODs (0.05-0.2) (Figure A.3B). Because the doubling time of the mixtures is relatively insensitive to the period of the LD cycle, it is sufficient to estimate the OD of each pair of mutants in just one LD condition and use this value in the dilution calculations. As a rule of thumb, it is sufficient to add 1.5-2 µL of each pool per 200 µL of BG11-IPTG.
- Plates and lighting conditions used for induction can be flexible. Both white lights and red LEDs can be used, as well as transparent or black plates.

ii. *Preparing samples for imaging.* At the end of induction period, mixtures from the induction plate were transferred into a clear-bottom imaging plate (Greiner, cat. no. 655097) filled with PBS (typically 5-10 µL in 100 µL PBS per well). The plate was spun at 4000x g for 10 min at 4 °C on a table top centrifuge with swinging-bucket attachments.

- The spinning step is important in getting cells to stick to the bottom of the plate and prevent them from moving during subsequent imaging. A piece of aluminum foil was placed beneath the plate to prevent dirt and oily stains from sullying the wells.

iii. *Imaging using 96-well microscopy.* Plates were imaged on an Olympus IX81 microscope using a 40x dry objective with 0.75 numerical aperture. The microscope was equipped with an automatic stage (Prior ProScanII) and camera with a large field of view (Hamamatsu Orca Flash 4.0 camerai, 6.5 μm pixel size, 2048 x 2048 pixels). These devices were controlled using SlideBook 6.0 software, which could be used to program the coordinates of the centers of all wells on the 96-well plate (relative to the "home" position). In this way, SlideBook controls were used to move the plate between desired wells. Focus was adjusted manually between wells. Each well was imaged once using Cy3 (for chlorophyll), YFP (for EYFP, exc. 500 nm / 20 nm bandpass), emm. 535/30 nm) and CFP (for mTurquoise) filters.

- It is preferable to take pictures near the centers of the wells to achieve even illumination.
- At the same induction conditions, mTurquoise gives much weaker signal relative to EYFP. In practice, it is preferable to rely on the EYFP signal to detect one mutant, and to use chlorophyll signal to detect all cells, rendering CFP channel images unnecessary.

iv. *Image processing using CellProfiler.* CellProfiler is a free software for image analaysis that contains a number of image processing tools which can be combined into pipelines. I created a pipeline to calculate the ratio of EYFP-expressing cells in an image.

Figure A.3B demonstrates that the methodology described in steps *II.i-II.iv* can be used to measure the fraction of EYFP-expressing mutants in a mixture. Taken together, steps in sections *I* and *II* above were used to perform a series of competition experiments described in this chapter. As an example, Figure A.3C shows example images from three timepoints during a competition experiment between an WT-EYFP and Δ*kaiBC* (Figure A.2F-G) in LD12:12. Figure A.3D shows the quantification of such images taken throughout the experiment. The ratio of WT cells in the population decreased from roughly 50% to just over 10% over the course of 32 days, suggesting that the Δ*kaiBC* mutant is more fit than WT cells under these conditions.

Measuring growth curves of cyanobacteria in light-dark cycles with different day lengths

In experiments described in Figure A.7Figure A.9 and Figure A.8, WT and Δ*kaiBC* mutants were grown in acid-washed flasks in standard growth conditions (30 °C, 70-100 μE, shaking at 200 rpm) in a Percival incubator. To mimic nighttime in days of different length, flasks were tightly covered with several layers of aluminum foil at appropriate times of day. Before the beginning of each growth curve, cells were "acclimated" to a given light-dark schedule for 5-9 days (see captions for details), during which period the cultures were diluted to OD 0.05 immediately after lights-on every day. After the last day of the acclimation period, cells

were diluted to OD 0.05 immediately after lights-on (day 0), and culture OD was monitored every 24 hours for the remainder of the experiment.

Detailed protocols and raw data

Raw data for experiments described in this Appendix can be found on Rust Lab Dropbox in the same folder as the copy of this thesis. File locations are specified in Table A.4.

For all competition experiments, code used to create figure panels is generated by Matlab scripts called "process96wp_***_thesis.m," which are located in subfolders within the respective parent directories. The *** represents a code name specific to each experiment (typically a color). These scripts also indicate which files contain image quantifications, descriptions of timepoints, etc.

Detailed protocols followed throughout the course of each experiment can be found in the spreadsheet files located at the top of each directory (typical filename: "yyyy-mm-dd_competitions96wp-***.xlsx").

Figure panel in Appendix A	Folder on Rust Lab Dropbox Containing Data and/or Code
Figure A.1B-C	fig1/fig1_BD_luminescence
Figure A.2B	fig2/fig2B_stdCurve
Figure A.2C-D	fig2/fig2C-D_WT/orange-Apr-24-plate
Figure A.3A,C	fig3-4-5/fig3_AC_LD11-11_LD15-15
Figure A.3B,E	fig3-4-5/fig3_BE_LD11-11_LD15-15
Figure A.3F	fig3-4-5/fig3_F_WT_ClaC
Figure A.4A-C	fig3-4-5/fig4_ABC_LP_SP_WT_longPer_EYFP
Figure A.4D-F	fig3-4-5/fig4_DEF_LP_SP_WT_longPer_mTurq
Figure A.5A,D	fig3-4-5/fig5_AD_pink
Figure A.5B,E	fig3-4-5/fig5_BE_orange
Figure A.5C,F	fig3-4-5/fig5_CF_red
Figure A.5G	fig3-4-5/fig5_fitnessCurve
Figure A.6-7	fig6-8/fig6-7_growthCurves/allTogetherByGenotype.xlsx contains all grow curve measurements; experiments are distinguished by date and genotype, which are indicated on the figures and legends
Figure A.8	fig6-8/fig8_lumi
Table A.1	Competitions_Plasmid_Maps

Table A.4. Locations of raw data depositories for experiments described in this Appendix.

RESULTS AND DISCUSSION

This section briefly summarizes the results of several sets of competition experiments and growth assays. Figure A.4 and Figure A.5 describe my efforts to reproduce the findings reported by Carl Johnson and colleagues, namely that period mutants whose clocks match the period of the light-dark environment enjoy a fitness advantage over mutants with longer or shorter clock periods [2], and that the arrhythmic CLAc mutant is outcompeted by WT in LD 12:12 [5]. Figure A.6 describes 96-well format experiments measuring the relative fitness of WT and clock-null mutants across a range of LD cycles, the question which motivated this study.

Finally, Figure A.7, Figure A.9, and Figure A.8 describe experiments measuring the growth curves of pure WT and clock-null mutants in flasks in conditions with varied day length (and 24-hr period). This line of work serves as the link between my study of how the cyanobacterial clock adapts to different day lengths (Chapter 1) and the fitness questions that motivated the work in the rest of this Appendix.

Attempts to replicate literature reports of the fitness of clock mutants grown in competition

First, I used the 96-well LED array protocols to grow WT (expressing mTurquoise2) in competition with the short-period mutant (expressing EYFP) in LD11:11 and LD15:15. Figure A.4C, adapted from Ouyang et al. [2], indicates that in their report a 1:1 mixture of these mutants grown in LD15:15 is dominated by WT after 27 days; on the other hand, in LD11:11, the mixture becomes dominated by the short-period mutant. As Figure A.4A shows, in my experiments WT had a fitness advantage over the short-period mutant in both light conditions,

reaching 70-80% of the mixture over 32 days. To rule out the possibility that the fluorescent marker influences the outcome of the competition, I repeated the experiment with swapped fluorescent markers and saw a similar result (Figure A.4B). As a negative control, I monitored the composition of a mixture of WT-mTurquoise and WT-EYFP in both LD11:11 and LD15:15 and verified that the proportion did not change significantly over time in either light-dark regime. Thus, in my experiments the fitness advantage of WT over the short-period mutant is independent of the period of the light-dark cycle.

Next, I studied the relative fitness between the arrhythmic CLAc mutant and WT. Based on observations by Woelfle et al., shown in Figure A.4G, I expected WT to outcompete the arrhythmic strain in LD cycles with near 24-hr period; however, I also expected that the fitness advantage would decrease further from LD12:12 because the predictions of a 24-hr circadian clock would be less useful in, e.g., a 30-hr day. Indeed, I found that WT is more fit than CLAc in LD12:12 (Figure A.4F). However, it appears that WT generally fares better than CLAc in longer days than in shorter days, even the period of the days is much longer than 24 hr. For example, WT is more fit relative to CLAc in LD15:15 than in LD11:11 (Figure A.4D-E).

To gain a more complete understanding of whether the resonance of clock period and the LD cycle confers a fitness advantage in my experimental setup, I grew the short-period mutant and the long-period mutant in competition with each other or the WT strain in a range of LD cycles encompassing the natural periods of all three strains (LD8:8 to LD15:15) (Figure A.5). I found reproducible differences in fitness between the strains, but they were only weakly dependent on the period of the LD cycle. A more prominent conclusion is that the mutant with the longer period fares better across LD conditions.

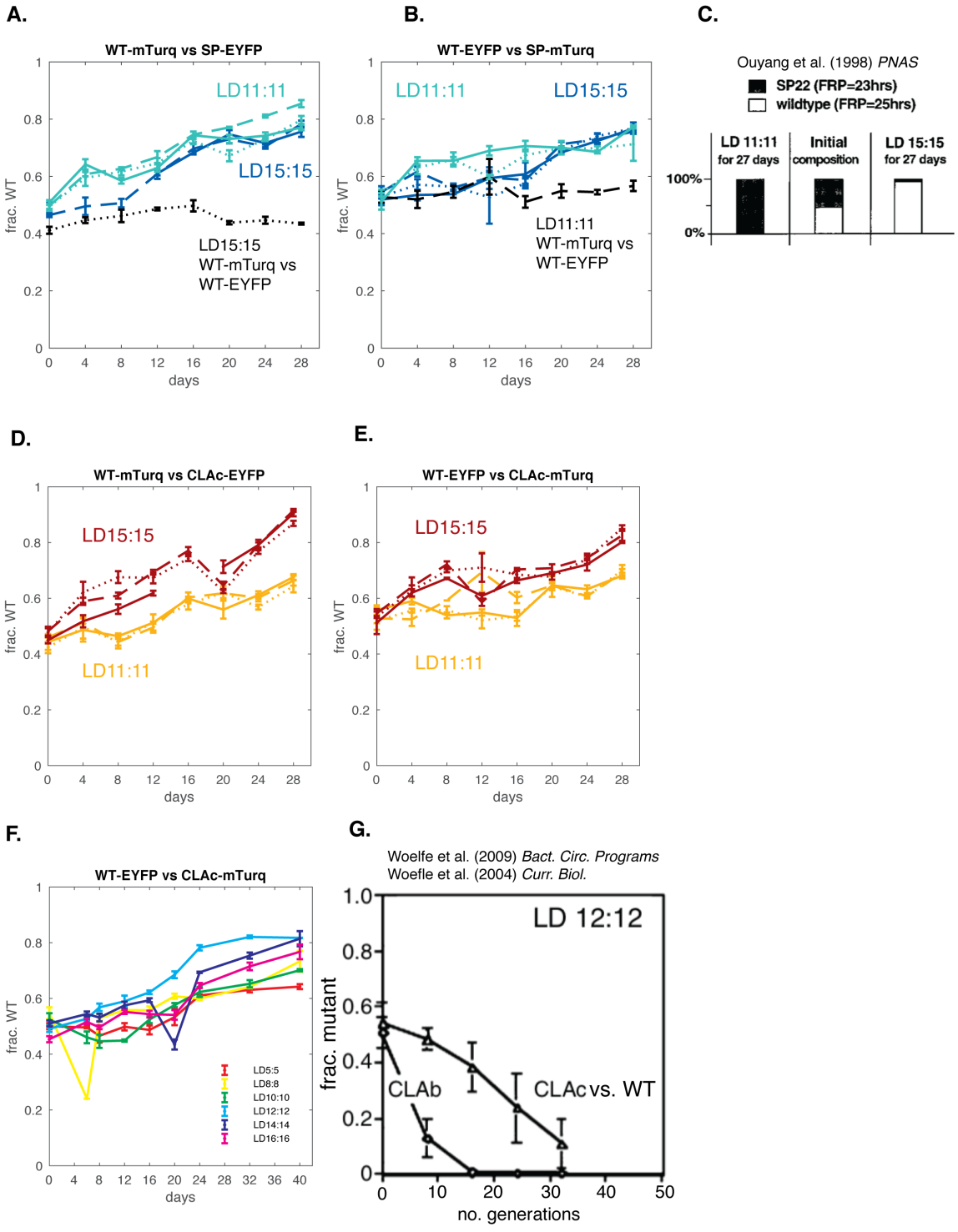

Figure A.4. Competition experiments in this study failed to replicate results from prior publications.

(Figure A.4 continued) (A) Competition experiment between mTurquoise-tagged WT^R (MRC1077) and EYFP-tagged short-period mutant (MRC1071) in LD11:11 and LD15:15. Black curves represent a control condition where mTurquoise-tagged WT^R (MRC1077) was competed against EYFP-tagged WT^R (MRC1070) in LD15:15 (fraction of mTurquoise-tagged strain is shown). Lines of the same color represent biological replicates, which were propagated in neighboring columns on the 96-well plate for the duration of the experiment. Three samples from each condition were imaged at each time point. Error bars represent mean ± standard deviation of the fraction of WT cells calculated from the three replicates.
(B) Competition experiment analogous to (A), but with swapped fluorescent markers. I.e., EYFP-tagged WT^R (MRC1070) was competed against mTurquoise-tagged short-period mutant (MRC1078) in LD11:11 or LD15:15. Black curves represent a control condition where mTurquoise-tagged WT^R (MRC1077) was competed against EYFP-tagged WT^R (MRC1070) in LD11:11 (fraction of EYFP-tagged strain is shown).
(C) Competition experiment between WT and short-period mutant in LD11:11 and LD15:15 reported by Ouyang et al. in [2], from where this panel adapted.
(D-E) Competition experiments in LD11:11 and LD15:15 between WT^R and the CLAc mutant. In (D), WT^R cells carried EYFP (MRC1070) and the CLAc mutant carried mTurquoise (MRC1081). In (E), the reporters were swapped: WT^R cells carried the mTurquoise marker (MRC1077) and the CLAc mutant carried the EYFP marker (MRC1075).
(F) Competition experiment between WT^R-EYFP (MRC1070) and CLAc-mTurquoise (MRC1081) in light-dark cycles with period from 10 to 32 hr (LD5:5-LD16:16).
(G) Competition experiment between WT and the CLAc mutant in LD12:12 reported by Woelfle et al. (2004) [6]. Panel adapted from [9].

For example, the long-period mutant outcompetes the short-period mutant in LD15:15 as well as in LD10:10 (Figure A.5A,D), and the WT strain does not lose out to the short-period mutant in any condition tested (Figure A.5C,F). In certain cases, period mutants appear to suffer the largest relative fitness *dis*advantage in conditions when the LD period most closely matches their natural period. For example, the short-period mutant is worst off relative to both the long-period mutant and the WT between LD8:8 and LD10:10 (Figure A.5A,C). These results were not due to differences in fluorescent markers between the strains, as experiments with swapped fluorescent markers led to similar competitive outcomes (compare Figure A.5A-C to Figure A.5D-F).

In sum, the methods I developed give reproducible measurements of relative fitness, but they are in disagreement with earlier reports by Ouyang et al. (Figure A.5D-F) [2]. Though I

mimicked aspects of their experimental conditions, there are important differences between our approaches. Most notably, growth conditions in large aerated flasks under white fluorescent lights in their study are very different from growth conditions in my protocols, which use a different spectrum of light and where cells are much more poorly aerated. The genotypes of the strains I engineered are also different from those used by Ouyang et al. Clock-conferred competitive advantage may be sensitive to these differences.

Measurement of relative fitness of WT *S. elongatus* relative to Δ*kaiBC* in LD cycles of different period

Next, I set out to measure the fitness profile of WT *S. elongatus* as a function of the period of the light-dark cycle, addressing the initial questions that motivated this study (Figure A.1). According to my initial hypothesis, the fitness of Δ*kaiBC* would be relatively constant across different LD periods, so that outcomes of competitive growth assays between WT and Δ*kaiBC* would reveal how the fitness of WT changes with the period of the light-dark environment. To this end, I grew WT and Δ*kaiBC* in six LD cycles spanning LD5:5 to LD16:16 (Figure A.6). This experiment was repeated three times in two genetic backgrounds. I found that Δ*kaiBC* consistently outcompeted WT.

Intriguingly, WT appears to be most *dis*advantaged relative to the clock-less mutant in LD12:12; this disadvantage disappears gradually as the period of the LD cycle decreases, and the two strains are nearly equally fit in LD5:5. Likewise, the difference in fitness is reduced in LD14:14 or LD16:16 compared to LD12:12. The fitness curve I measured in this way (Figure A.6G) exhibits nearly the opposite behavior from my initial prediction (Figure A.1).

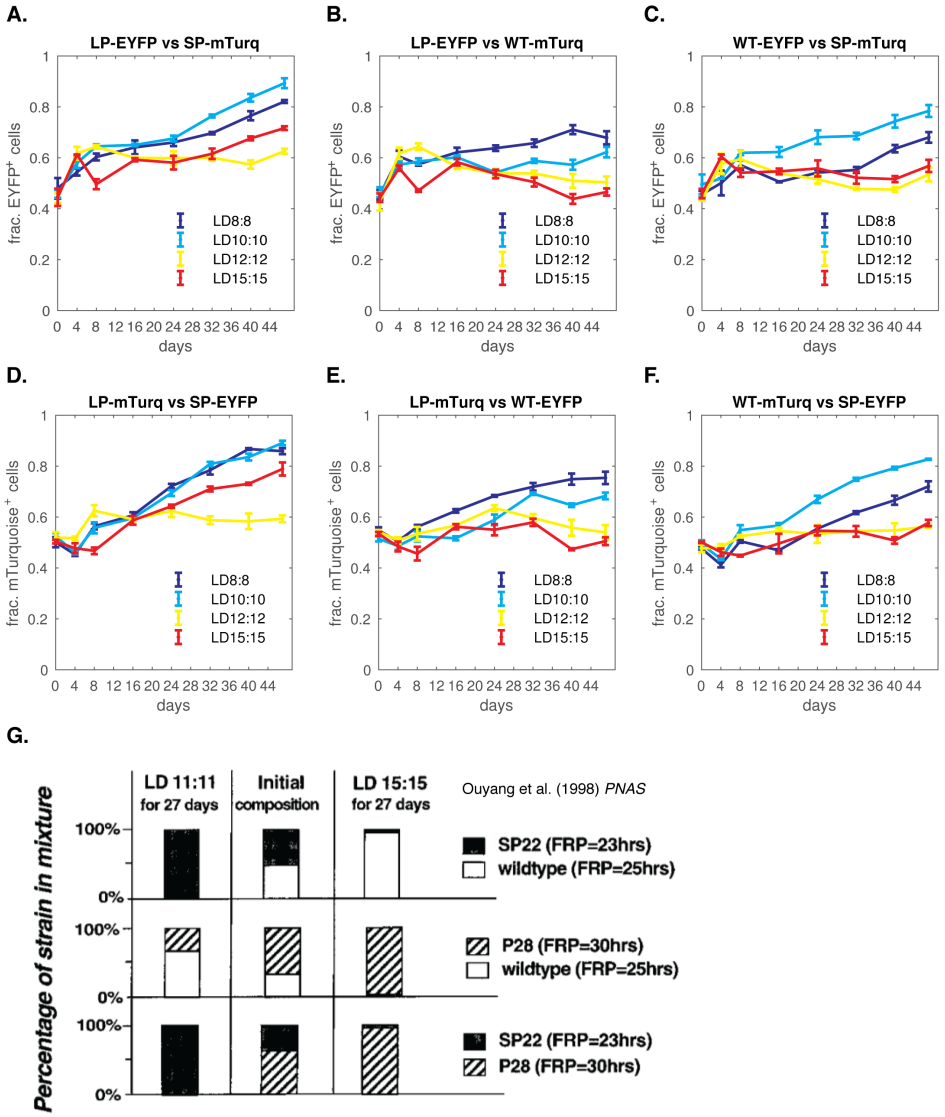

Figure A.5. Fitness of period mutants in this study is not maximized when clock period matches LD cycle period.

(A-C) Competition experiments in LD8:8, LD10:10 and LD15:15, between (A) the long-period mutant and short-period mutant (MRC1072 vs. MRC1078), (B) the long-period mutant and wild-type rescue mutant (MRC1072 vs. MRC1077), and (C) the wild-type rescue mutant and short-period mutant (MRC1070 vs. MRC1078). The mutant with the longer period carries the EYFP marker, and the mutant with the shorter period carries the mTurquoise marker.

(D-F) Competition experiments performed by analogy with (A-C), but with switched reporter colors. The mutant with the longer period carries the mTurquoise marker, and the mutant with the shorter period carries the EYFP marker. Strains used: (D) MRC1079 vs. MRC1071, (E) MRC1079 vs. MRC1070, (F) MRC1077 vs. MRC1071.

(Figure A.5 continued) (G) Outcomes of competition experiments between pairs of clock period mutants reporter by Ouyang et al. (1998), from where this panel is adapted [2]. SP22 refers to the short-period mutant, P28 to the long-period mutant, FRP stands for "free-running period."

In the remainder of this appendix, I present my measurements of relative growth rate of WT and clock-null mutants grown in flasks under fluorescent lights. In this different set of conditions, WT does enjoy a fitness advantage in LD12:12, even though this behavior depends on the genetic background of the strains.

WT (AMC1300) enjoys a growth advantage relative to Δ*kaiBC*/AMC1300 in 24-hr light-dark cycles when cultures are grown in flasks under white fluorescent lights

One of the major conclusions of my work in Chapter 2 is that the circadian clock of cyanobacteria adapts to changing day length, tracking the middle of the day across conditions from LD8:16 to LD16:8. In the Discussion section in Chapter 2, I argued that this ability allows the cells to fairly balance the resources between the morning and evening programs of gene expression. I hypothesized that this ability would confer a fitness advantage. To test this hypothesis, I grew WT and Δ*kaiBC* strains (both in AMC1300 background, see Table A.2) in 24-hr cycles with 8-16 hours of daylight or under constant illumination). Four days after the cultures were seeded at the same initial density, WT cultures were much denser than clock mutants in all light-dark conditions, but not in LL (Figure A.7).

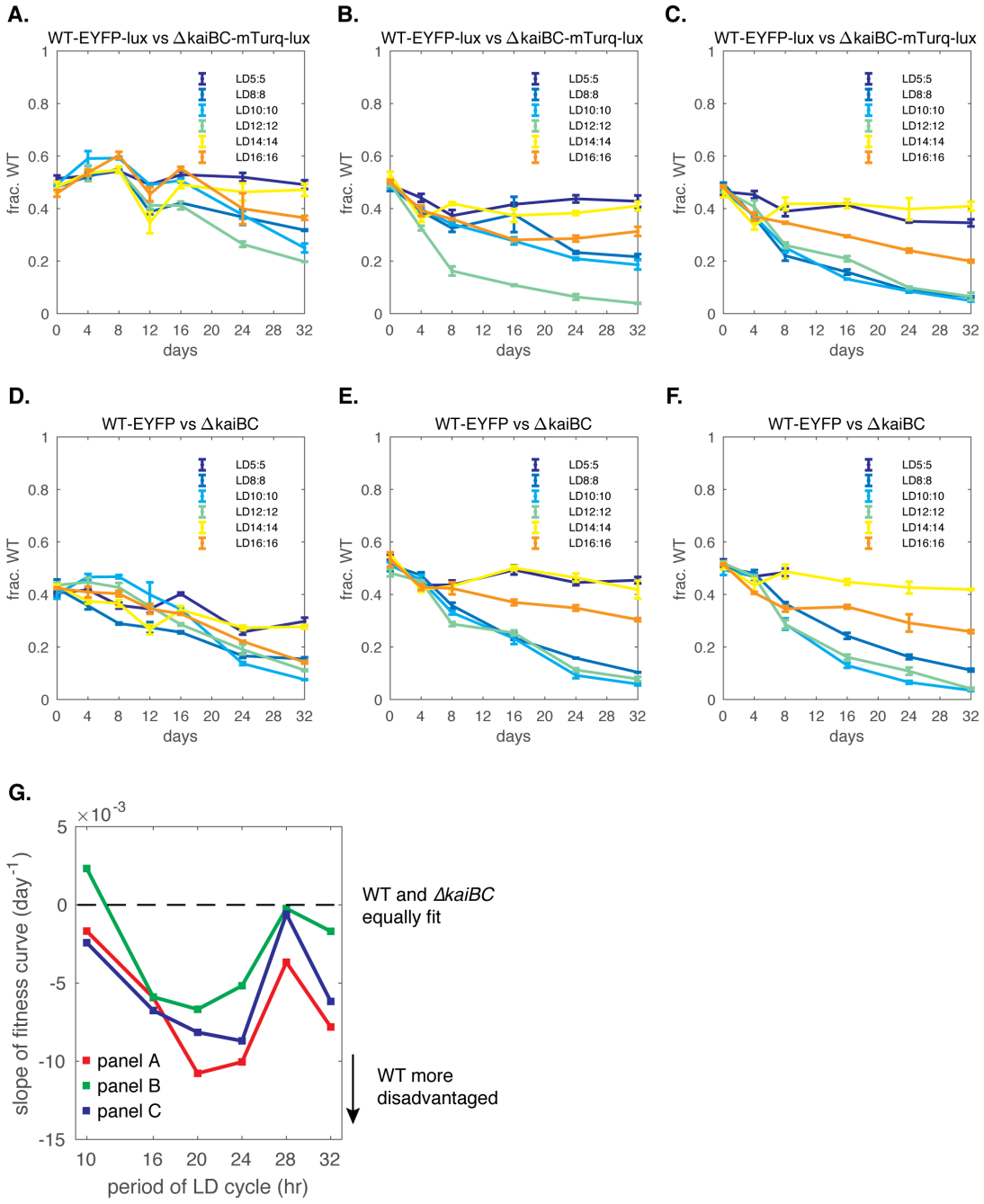

Figure A.6. Clock-null mutants enjoy a fitness advantage over WT cells in LD8:8, LD10:10 and LD12:12 in 96-well LED array experiments.
(A-C) Biological replicates of competition experiments between WT^{R}-EYFP (MRC1070) and Δ*kaiBC*-mTurquoise (MRC1076) in varied LD cycles (LD5:5 to LD16:16). In addition to the fluorescent markers, these strains carry a reporter of circadian gene expression P_{psbAI}::*luxABCDE* (cloning strategy described in Figure A.2A).

(Figure A.6 continued) (D-F) Biological replicates of competition experiments between WT-EYFP (MRC1036) and Δ*kaiBC* (MRC1076) in varied LD cycles (LD5:5 to LD16:16). In contrast to (A-C), these mutants do not carry P_{psbAI}*::luxABCDE*; additionally, the Δ*kaiBC* strain (MRC1036) does not carry a fluorescent marker (cloning strategy described in Figure A.2F-G). **(G)** Linear slopes of fitness curves in (A-C) from 8-32 days of each experiment. Slope of 0 indicates that the proportion of the two stains remains unchanged throughout the course of the experiment. Negative slope indicates that the proportion of the WT strain decreases over time.

Though in these conditions WT does enjoy a reproductive advantage over Δ*kaiBC* in LD12:12, the fitness effects were most pronounced in longest or shortest day lengths, suggesting that the clock's ability to track day length is most beneficial under physiologically relevant extremes. Intriguingly, in these growth conditions the circadian rhythm of *S. elongatus* aligns to dusk (Figure A.8). Thus, both the relative fitness between these strains and the seasonal entrainment of the clock are affected by growth under red LED arrays in 96-well plates vs. in a traditional setup. Two major differences between the two conditions are that cultures are much better aerated when shaken in large volumes in flasks and that white fluorescent bulbs emit a much broader spectrum of light as compared to red LEDs. These observations suggest that redox stress or illumination at shorter wavelengths may be important factors affecting fitness of cyanobacteria.

The fitness advantage of WT relative to Δ*kaiBC* grown in flasks under white fluorescent lights depends on the genetic background of the strains

Using the same methodology, I measured the growth rates of WT and Δ*kaiBC* in three replicate experiments using two genetic backgrounds. All of the measurements are plotted in Figure A.9. I reproducibly measured that wild-type *S. elongatus* in AMC1300 background (WT/1300) grows faster than the clock mutant in the same background (Δ*kaiBC*/1300) in

LD10:10, LD12:12 and LD14:10, but not in LL Figure A.9A). However, I could not observe similar effects in true wild-type *S. elongatus* 7942 and the clock mutant made in that background (Figure A.9B). Subtle differences became apparent after day 6 in these experiments, but the trends are opposite to what I observed in AMC1300 background. For example, WT fares worse in LL relative to Δ*kaiBC*, but there are no differences in growth in LD10:14 or LD14:10.

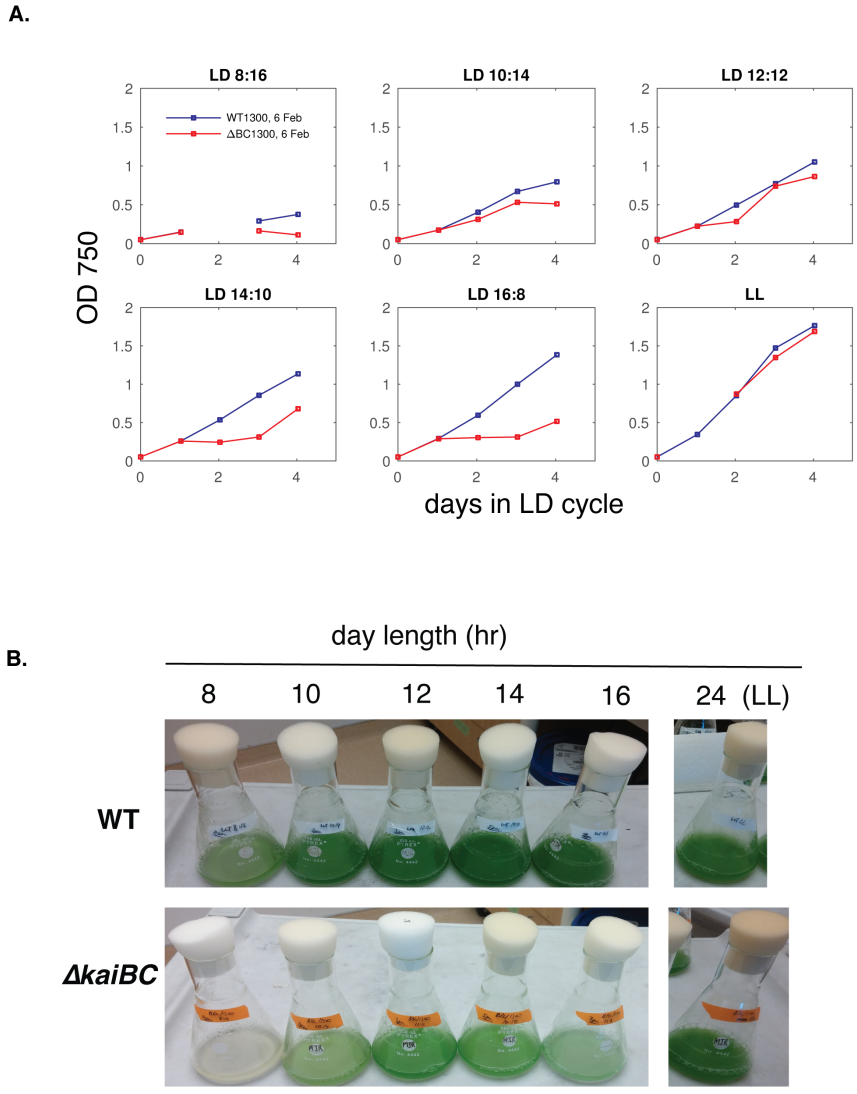

Figure A.7. Δ*kaiBC* mutant is disadvantaged relative to WT in 24-hr LD cycles with varying day lengths when grown in flasks.

(Figure A.7 continued) (A) Growth curves of WT *S. elongatus* and the *kaiBC-null* mutant, both in AMC1300 background (WT/1300 is MRC1083; ΔBC/1300 is MRC1084), in LD cycles of different day length. Cells were grown in flasks with shaking (≈200 rpm) in a Percival growth chamber at constant 30 °C. White fluorescent lights (≈70-100 μE) were set on a timer to generate a LD16:8 cycle. To create conditions with shorter day lengths, flasks were covered with several layers of aluminum foil at appropriate times of day. Prior to day 0, cells were "acclimated" to a given light-dark cycle for 9 days, during which period the cells were diluted to OD 0.05 every day just after lights-on.
(B) Photos of flasks subjected to different light-dark cycles at the last day of experiment.

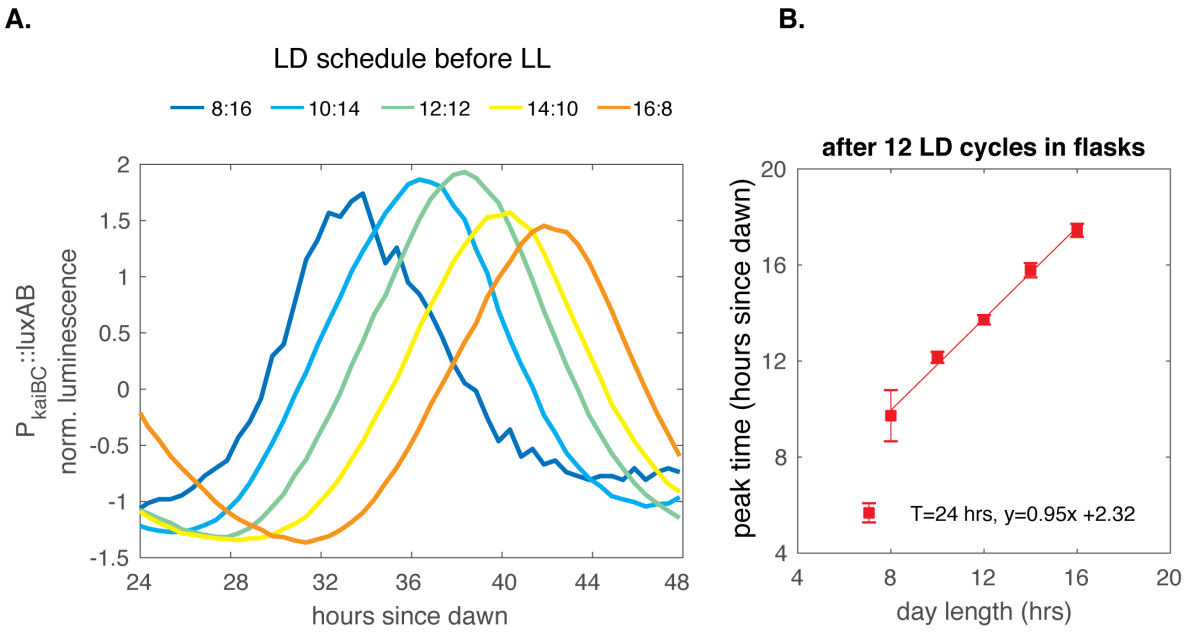

Figure A.8. The circadian clock of *S. elongatus* tracks dusk in 24-hr cycles of varying day length when grown in flasks under bright fluorescent lights.
(A) Luminescence recordings from WT/1300 cells grown in LL after they had been exposed to 12 LD cycles of various day length (cells taken from the Mar. 13 trial in Figure A.9).
(B) Peak time of curves in (A) estimated by sinusoidal fitting.

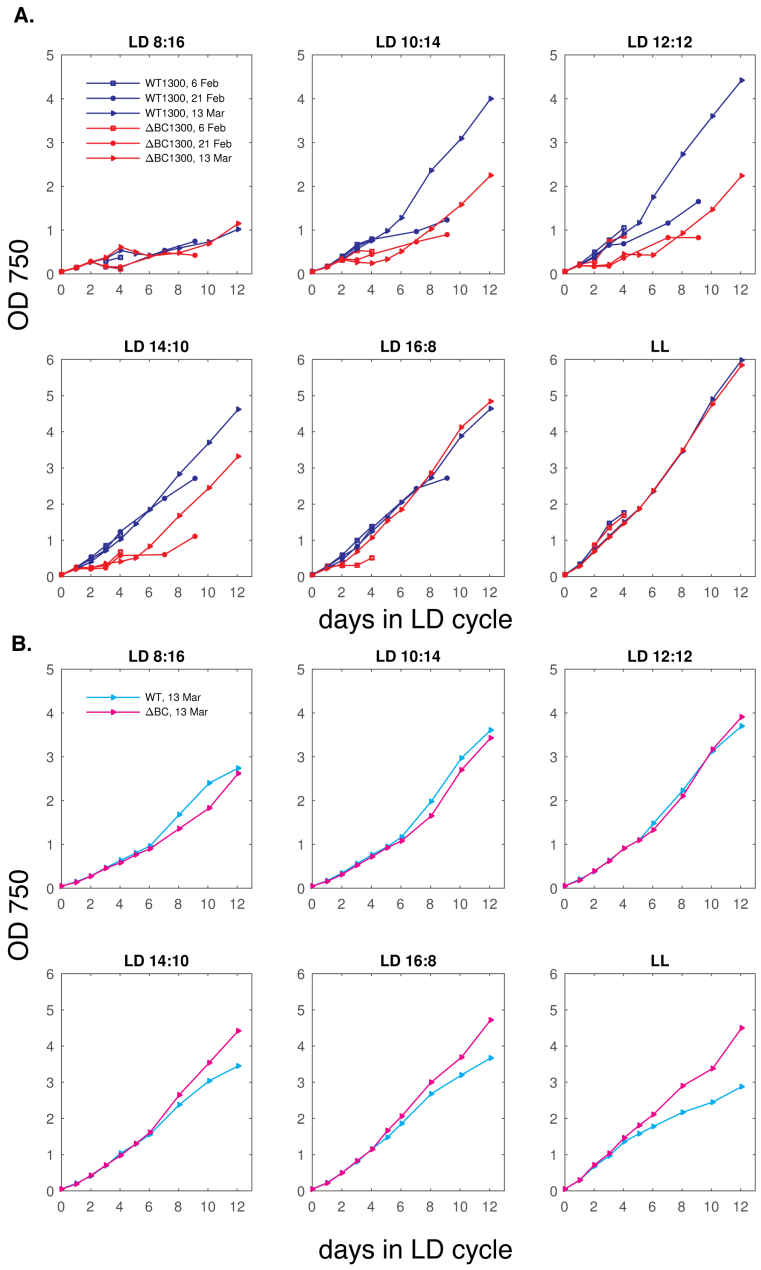

Figure A.9. The fitness advantage of WT relative to Δ*kaiBC* in 24-hr LD cycles with variable day length depends on the genetic background.
(A) Biological replicates of experiment in Figure A.7. Trial from Feb. 6 is replotted from Figure A.7; for the trial on Feb. 21, cells were acclimated to a given day length condition for 5 days prior to the beginning of the growth curve; for the trial on Mar. 13, cells were acclimated for 7 days.
(B) Growth curves as in (A) (Mar. 13 trial), performed using strains without luminescent reporters, WT *S. elongatus 7942* (MRC1035) and Δ*kaiBC* mutant (MRC1038) in WT background.

Concluding remarks

By definition, organismal fitness depends on the environment in which it is assessed. My results suggest that the fitness of cyanobacteria depends not only on the frequency of the light-dark cycle, but also on other features of growth conditions and strain genetics. Both genetic background and growth conditions appear to play a role. It is noteworthy that the strains designed for the 96-well competition experiments were derived from the WT *S. elongatus* 7942 strain and the clock-null mutant made in that background, i.e., the same strains that showed only minor differences in growth rate as a function of day length in Figure A.9B. Both WT and WT/1300 have been propagated in the lab for decades, in the absence of selection pressures in the natural environment. It is possible that at some point during its laboratory history, the WT strain picked up a spontaneous mutation which was adaptive in the laboratory setting, but makes the cells have a weakened response to changes in day length.

REFERENCES

1. Yerushalmi, S., and Green, R.M. (2009). Evidence for the adaptive significance of circadian rhythms. Ecology Letters *12*, 970–981.

2. Ouyang, Y., Andersson, C.R., Kondo, T., Golden, S.S., and Johnson, C.H. (1998). Resonating circadian clocks enhance fitness in cyanobacteria. Proceedings of the National Academy of Sciences *95*, 8660–8664.

3. Ma, P., Woelfle, M. a, and Johnson, C.H. (2013). An Evolutionary Fitness Enhancement Conferred by the Circadian System in Cyanobacteria. Chaos, solitons, and fractals *50*, 65–74.

4. Ito, H., Mutsuda, M., Murayama, Y., Tomita, J., Hosokawa, N., Terauchi, K., Sugita, C., Sugita, M., Kondo, T., and Iwasaki, H. (2009). Cyanobacterial daily life with Kai-based circadian and diurnal genome-wide transcriptional control in Synechococcus elongatus. Proceedings of the National Academy of Sciences of the United States of America *106*, 14168–73.

5. Woelfle, M.A., Ouyang, Y., Phanvijhitsiri, K., and Johnson, C.H. The Adaptive Value of Circadian Clocks: An Experimental Assessment in Cyanobacteria. Current Biology, 6.

6. Leypunskiy, E., Lin, J., Yoo, H., Lee, U., Dinner, A.R., and Rust, M.J. (2017). The cyanobacterial circadian clock follows midday in vivo and in vitro. eLife *6*. Available at: https://elifesciences.org/articles/23539 [Accessed March 30, 2018].

7. Ishiura, M. (1998). Expression of a Gene Cluster kaiABC as a Circadian Feedback Process in Cyanobacteria. Science *281*, 1519–1523.

8. Kiyohara, Y.B., Katayama, M., and Kondo, T. (2005). A Novel Mutation in kaiC Affects Resetting of the Cyanobacterial Circadian Clock. Journal of Bacteriology *187*, 2559–2564.

9. Woelfle, M.A., and Johnson, C.H. (2009). The Adaptive Value of the Circadian Clock System in Cyanobacteria. In Bacterial Circadian Programs, J. L. Ditty, S. R. Mackey, and C. H. Johnson, eds. (Berlin, Heidelberg: Springer Berlin Heidelberg), pp. 205–221. Available at: http://link.springer.com/10.1007/978-3-540-88431-6_12 [Accessed March 30, 2018].